Experimental Investigation of Cycling Characteristics of Anatase TiO_2 Nanotubes as Negative Electrode of Lithium-ion Batteries

This thesis is submitted to the Department of Mechanical Engineering of Chittagong University of Engineering & Technology as a partial fulfillment of requirement for the degree of

MASTER OF SCIENCE IN MECHANICAL ENGINEERING

Submitted by

Simul Das

ID: 17MME017P

Session: 2017-2018

Supervised By

Dr. Md. Arafat Rahman

Professor

Department of Mechanical Engineering

Chittagong University of Engineering & Technology (CUET)

Approval

This thesis titled "**Experimental Investigation of Cycling Characteristics of Anatase TiO_2 Nanotubes as Negative Electrode of Lithium-ion Batteries**" submitted by Simul Das, Student ID: 17MME017P, Session: 2017-2018 has been accepted as ……in partial fulfillment of the requirement for the degree of Masters of Science (M.Sc.) in Mechanical Engineering dated on ……...

Board of Examiners

01	**Prof. Dr. Md. Arafat Rahman,** Dept. of ME, CUET	**Chairman**
02	**Prof. Dr. Sheikh Muhammad Humayun Kabir,** Dept. of ME, CUET	**Member (Co-Supervisor)**
03	**Prof. Dr. Mohammad Mizanur Rahman,** Dept. of ME, CUET	**Member**
04	**Dr. Md. Abu Mowazzem Hossain,** Associate Professor, Dept. of ME, CUET	**Member**
05	**Prof. Dr. Mohammad Asaduzzaman Chowdhury,** Dept. of ME, DUET.	**Member (External)**
06	**Head**, Dept. of ME, CUET	**Member (Ex-officio)**

Declaration

Thus, I authenticate that all of this thesis's work is original, except for cited quotations and summaries. No degree has accepted this thesis, and it is currently being presented for only this degree.

Name: Simul Das

ID: 17MME017P

Date:

Copyright Declaration

I hereby declare that I am the sole author of the thesis titled "**Experimental Investigation of Cycling Characteristics of Anatase TiO_2 Nanotubes as Negative Electrode of Lithium-ion Batteries**". Along with this, submitted a softcopy is true copy of my final hardcopy thesis including any required final revisions, as accepted by the board of examination.

I hereby release my copyright to **Chittagong University of Engineering and Technology (CUET)** for uploading the electronic version of the same to the **'Digital Repository (Institutional Repository)'** of **CUET** after one year from the day of submission. Apart from this, the existing or to be approved **Open Education Resources (OER)** policies and procedures of **Chittagong University of Engineering and Technology (CUET)** shall be applicable to this research work.

I also acknowledge my sincere delivering of copyright to Chittagong University of engineering and Technology (CUET) to reproduce this thesis by reprography or by other means, in total or by part at the necessity of individuals for the purpose of scholarly research.

……

Signature of the Author

Acknowledgement

With the goal to finish my thesis and reach the end of the five-year M.Sc. journey, I had to remain physically and psychologically stable, thus I would like to express my gratitude to Almighty GOD for His auspicious kindness in maintaining me in that state. Additionally, I must express my sincere gratitude to the Chairman of the board Dr. Md. Arafat Rahman, Professor, Department of Mechanical Engineering, CUET, who served as my esteemed supervisor and provided constant guidance & support throughout the completion of my thesis. It is important to note my unwavering love for him, my experiences, the academic & teamwork skills I gained, the direction, inspiration, and encouragement I received. All of these things motivated me to work as hard as I could on this thesis.

I am grateful to my co-supervisor Prof. Dr. Sheikh Muhammad Humayun Kabir, Department of Mechanical Engineering at CUET for his professional administrative assistance with my thesis. Additionally, I'd like to express my gratitude to the internal board member, Prof. Dr. Mohammad Mizanur Rahman, Head, Department of Mechanical Engineering at CUET and Dr. Md. Abu Mowazzem Hossain, Associate Professor in the same Department, for agreeing to serve on the committee for my thesis oral examination. My deepest gratitude goes out to Prof. Dr. Mohammad Asaduzzaman Chowdhury, Department of Mechanical Engineering, DUET, Bangladesh, for participating in my oral examination committee as an external examiner. It is also necessary to thank the other members of the Department of Mechanical Engineering at CUET for their encouragement and assistance.

I am writing to express my gratitude to Dr. Md. Saiful Islam, Assistant Professor, Department of Glass and Ceramic Engineering at BUET, for his kind support and

encouragement while I worked to finish this thesis. The Coin "Cell Battery Crimper Machine," a vital tool for this thesis, was provided by Syed Md. Ikram, Chief Technical Officer, Department of Mechanical Engineering, CUET. I also want to thank him for his technical help. I am grateful for the kind help with my thesis.

Lastly, I would like to thank my parents, Sasanka Mohan Das and Silpi Das, for establishing in me a strong work ethic and for encouraging me to achieve my objectives. I also want to express my sincere gratitude to my lovely wife **Prapti Das** for all her love, understanding, and unwavering support. Last but not least, I have to express my gratitude to my daughter **Pranavi Das Stuti** for being my inspiration and the driving force behind everything I do.

Dedication

I dedicate this thesis report to my father, Sasanka Mohan Das; my mother, Silpi Das; my wife, **Prapti Das**; my daughter **Pranavi Das Stuti** and my mentor, Dr. Md. Arafat Rahman, who has been my constant source of inspiration and motivation throughout my academic journey. Your unwavering belief in me and your endless encouragement has been the driving force behind my success, and I am forever grateful for your love and support.

Abstract

Lithium-ion batteries (LIBs) have emerged as a ground-breaking technology that has revolutionized modern portable devices and facilitated the electrification of numerous industries, such as transportation and grid energy storage, as a result of the pursuit of sustainable and efficient energy storage solutions. Due to their superior qualities, such as their high energy density, prolonged cycle life, and lightweight nature, which facilitates greater portability, lithium-ion batteries have been embraced as a replacement for conventional energy storage systems. A consistent effort has been made to investigate developments in the field of lithium-ion batteries in response to the growing need for energy storage systems that exhibit improved performance metrics, including increased energy density, faster charging capabilities, enhanced safety, and longer lifespan. The current issues with current LIB technology must be resolved in order to use lithium-ion batteries (LIBs) as a viable energy storage solution with increased capacity. This requires the creation of new electrolyte formulations, cell structures, and production methods. Nanotubes Anatase TiO_2 (NT-TiO_2) have been brought forth via electrochemical anodization of 99.9% pure titanium foils in a fluorine containing and four different percentages (10%, 20%, 30% & 50%) of Ethylene Glycol (EG) electrolyte. After that calcination process is done at 550^0C for 2h. Different types of structure is observed in SEM images for four different electrolyte type samples. Among them in 10% of EG electrolyte type, the nanotubes NT-TiO_2 is observed and by using this as anode the battery is assembled and tested the electrochemical analysis. In the first cycle, the charge-discharge capacities are 550 $mAhg^{-1}$ and 400 $mAhg^{-1}$, respectively, with columbic efficiency 75.75%. At 40th cycle, charge-discharge capacities are found to be 375 $mAhg^{-1}$ and 325 $mAhg^{-1}$, respectively, and at this cycle, the columbic efficiency is 80%. The superior electrochemical performances of this type of battery were

originated from its high specific surface area and highly nanotubes structure. These advanced features of the nanotubes provide higher contact between electrode and electrolytes, shorten the diffusion pathways for conductive ions and electrons and ensure fast kinetics.

সার-সংক্ষেপ

লিথিয়াম-আয়ন ব্যাটারি একটি গ্রাউন্ড ব্রেকিং প্রযুক্তি হিসাবে আবির্ভূত হয়েছে যা আধুনিক পোর্টেবল ডিভাইসগুলিতে বিপ্লব ঘটিয়েছে এবং টেকসই এবং দক্ষ শক্তি সঞ্চয়ের সমাধানের অন্বেষণের ফলে পরিবহন এবং গ্রিড শক্তি সঞ্চয়ের মতো অসংখ্য শিল্পের বিদ্যুতায়নকে সহজতর করেছে। তাদের উচ্চতর গুণাবলীর কারণে, যেমন তাদের উচ্চ শক্তির ঘনত্ব, দীর্ঘায়িত চক্র জীবন এবং হালকা প্রকৃতি, যা অধিক বহনযোগ্যতাকে সহজতর করে, লিথিয়াম-আয়ন ব্যাটারিগুলিকে প্রচলিত শক্তি সঞ্চয় ব্যবস্থার প্রতিস্থাপন হিসাবে গ্রহণ করা হয়েছে। শক্তি সঞ্চয় ব্যবস্থার ক্রমবর্ধমান প্রয়োজনের প্রতিক্রিয়া হিসাবে লিথিয়াম-আয়ন ব্যাটারির ক্ষেত্রে উন্নয়নগুলি তদন্ত করার জন্য একটি ধারাবাহিক প্রচেষ্টা করা হয়েছে যা উন্নত কর্মক্ষমতা মেট্রিক্স প্রদর্শন করে, যার মধ্যে শক্তির ঘনত্ব, দ্রুত চার্জ করার ক্ষমতা, উন্নত নিরাপত্তা এবং দীর্ঘ জীবনকাল রয়েছে। লিথিয়াম-আয়ন ব্যাটারি বর্ধিত ক্ষমতা সহ একটি কার্যকর শক্তি সঞ্চয়ের সমাধান হিসাবে ব্যবহার করার জন্য বর্তমান LIB প্রযুক্তির বর্তমান সমস্যাগুলি অবশ্যই সমাধান করা উচিত। এর জন্য নতুন ইলেক্ট্রোলাইট ফর্মুলেশন, কোষের গঠন এবং উৎপাদন পদ্ধতি তৈরি করা প্রয়োজন। Nanotubes Anatase TiO2(NT-TiO2) একটি ফ্লোরিন ধারণকারী ৯৯.৯৯% বিশুদ্ধ টাইটানিয়াম ফয়েল এবং ইথিলিন গ্লাইকল (EG) ইলেক্ট্রোলাইটের চারটি ভিন্ন শতাংশ (১০%, ২০%, ৩০% এবং ৫০%) ইলেক্ট্রোকেমিক্যাল অ্যানোডাইজেশনের মাধ্যমে আনা হয়েছে। এর পরে ক্যালসিনেশন প্রক্রিয়াটি ২ ঘন্টার জন্য ৫৫০০সে তাপমাত্রায় করা হয়। চারটি ভিন্ন ইলেক্ট্রোলাইট ধরণের নমুনার জন্য SEM চিত্রগুলিতে বিভিন্ন ধরণের গঠন পরিলক্ষিত হয়। তাদের মধ্যে ১০% EG ইলেক্ট্রোলাইট টাইপের মধ্যে, ন্যানোটিউব NT-TiO2 পরিলক্ষিত হয় এবং এটিকে অ্যানোড হিসাবে ব্যবহার করে ব্যাটারি একত্রিত করা হয় এবং ইলেক্ট্রোকেমিক্যাল বিশ্লেষণ পরীক্ষা করা হয়। প্রথম চক্রে, চার্জ-ডিসচার্জ ক্ষমতা যথাক্রমে ৫৫০ mAhg-1 এবং ৪০০ mAhg-1, কলম্বিক দক্ষতা ৭৫.৭৫% সহ। 40 তম চক্রে, চার্জ-ডিসচার্জ ক্ষমতা যথাক্রমে ৩৭৫ mAhg-1 এবং ৩২৫ mAhg-1 পাওয়া যায় এবং এই চক্রে, কলম্বিক দক্ষতা ৮০%। এই ধরনের ব্যাটারির উচ্চতর ইলেক্ট্রোকেমিক্যাল পারফরম্যান্স এর উচ্চ নির্দিষ্ট পৃষ্ঠ এলাকা এবং অত্যন্ত ন্যানোটিউব গঠন থেকে উদ্ভূত হয়েছিল। ন্যানোটিউবগুলির এই উন্নত বৈশিষ্ট্যগুলি ইলেক্ট্রোড এবং

ইলেক্ট্রোলাইটের মধ্যে উচ্চতর যোগাযোগ প্রদান করে, পরিবাহী আয়ন এবং ইলেকট্রনের জন্য প্রসারিত পথগুলিকে ছোট করে এবং দ্রুত গতিবিদ্যা নিশ্চিত করে।

Table of Contents

List of Figures

List of Tables

Chapter 01

Introduction

1.1 Background

Nowadays, the generation of electricity is approximately 5900 terawatts per hour (TWH) and will be increased by over 7000 terawatts per hour (TWH) in the year 2030 [1]. Currently, approximately 68% of the energy utilized for power generation is derived from fossil fuel sources, including natural gas (21%), coal (42%), and oil (5%). The remaining are from renewable energy technology like nuclear (14%), hydro (15%) and others 3% [2].

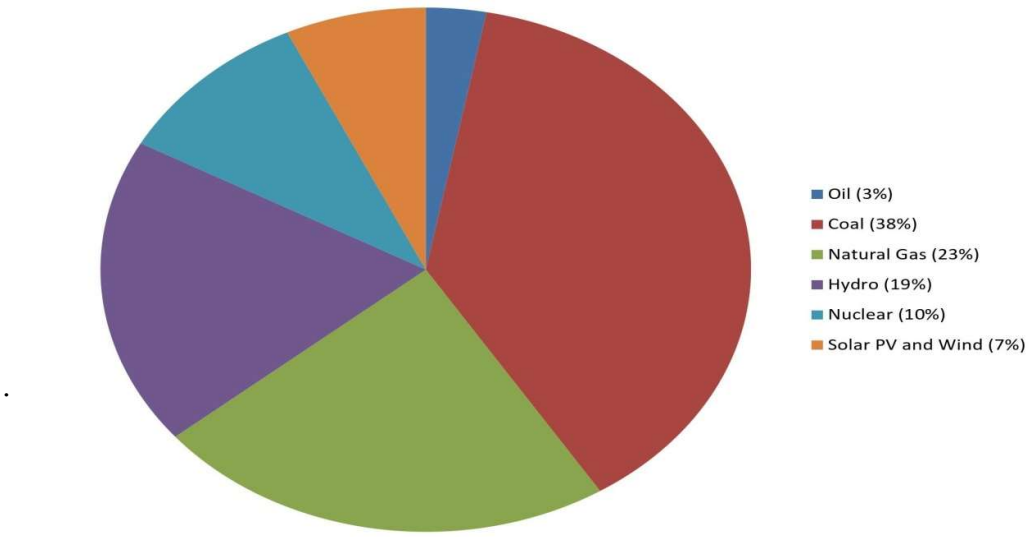

.

Figure 1. 1 World electricity generation by source in 2018 [3].

Compared to overall energy consumption, the demand for electricity is rising more quickly. According to conservative estimates, oil supplies will start to deplete among the fossil fuels in the next 30 years [4]. Due to vast coal reserves, current consumption levels may be sustained longer than with oil and gas for its dominance as a source of energy generation worldwide [5]. But an average 1000 g of CO_2 is emitted in the air for generating one unit of electricity by using coal. CO_2, a greenhouse gas commonly recognized as the

main cause of global warming [6, 7]. Coal-fired power plants in the United States emit around 1.5 billion metric tons of carbon dioxide (CO2) on a yearly basis. Furthermore, there is a growing trend of escalating pollution levels from developing countries. Moreover, there was a decline in the demand for nuclear energy because of nuclear tragedies (Three Mile Island in 1979, Chernobyl in 1986 and Fukushima in 2011) [8, 9].

Concerns about energy security and the environment related to the usage of fossil fuels have combined with increasing interest in generating electricity from renewable sources. The most prevalent and potentially accessible sources of energy are solar and wind [6, 10, 11]. A year's worth of global energy needs can be satisfied by the solar radiation energy that the Earth gets in just one hour. The world's need for electrical energy may be greatly increased by capturing even a small portion of the wind's potential energy. Solar and wind power aren't stable and consistent energy sources, though. Because additional power facilities (often those powered by fossil fuels) must be used to compensate for the unpredictability, this unpredictable character presents severe difficulties for the electric grid operators. Low-cost electrical energy storage (EES) is going to be required to control the spontaneous generation of renewable energy. The cost associated with implementing Energy Storage Systems (EES) has been identified as a notable issue [12]. However, it is widely recognised as an essential enabler for the smart grid or future grid. There is an expectation that a significant proportion of renewable energy sources will be integrated into the provision of fuel, specifically electricity, for hybrid and electric cars [13]. In order to maintain the frequency of the AC (alternating current) system within restricted environments, balancing services are employed to ensure equilibrium between power generation and demand. EES possesses the necessary capabilities to provide this service through the process of absorbing electrical energy during the

charging cycle, which occurs when there is an excess of electrical generation in comparison to the demand. Conversely, during the discharging cycle, EES injects electricity into the power grid promptly when there is an inadequate amount of electrical generation. In addition to supplying the grid with dependability services, EES may boost the economic effectiveness of the energy infrastructure by increasing its usage. About 50% of the total power transmission system (T&D) is typically used [14]. The utilization of infrastructure frequently requires enhancement, even though it is constructed to accommodate peak load situations, with an additional margin of reserve capacity and predictions for capacity growth incorporated into the peak load estimation. From the perspective of economic efficiency, this could be better. The system must be loaded more equitably to maximize the grid assets' overall efficiency. EES may help this process by diverting electricity from peak to off-peak times. Figure.1.2 presented depict the utilization of load levelling techniques to store electrical energy during periods of low-cost generation, such as off-peak hours, and subsequently release it during peak hours when its value is higher. As a result, great interest has been paid to inventing more efficient technology to store energy. Different ESSs are investigated widely as; i) Electrochemical systems (Batteries, Fuel cells, Super capacitors), ii) Magnetic systems (Super conducting energy storage), iii) Hydro systems (water pumps), iv) Pneumatic systems (Air compressors), v) Mechanical system (Flywheels) vi) Thermal system (Molten salts, Water and oil heaters) [15-17].

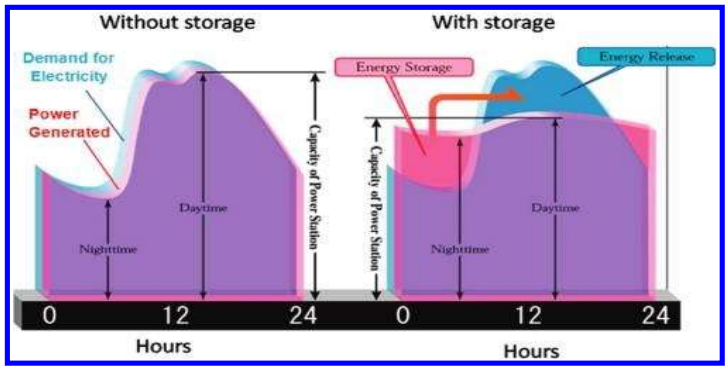

Figure 1. 2 Schematic of balancing generation and demand via load leveling, a typical case of load shifting (Courtesy of NGK, Inc.) (Adapted from [2]).

Some factors, including energy storage effectiveness, energy cost, accessible energy sources, energy needs, applications, and infrastructures, must be considered when choosing a suitable technology. The electrochemical energy storage system is often regarded as a highly practical way for storing energy, as it allows for the conversion and storage of electrical energy in the form of chemical compounds. Electrons are the common carrier for both chemical and electric energy, which inhibits the minimization of losses [18]. The subject of most electrochemical ESS is batteries. Two terms defining the ESS state are shown bilaterally in Fig.1.3, which compares several ESSs. The first is known as specific power or power density, which describes how much power a system can produce per unit of weight. The second is specific energy, which refers to how much energy a system can store inside. A system characterized by a greater energy density has the potential to sustain energy provision for an extended duration, irrespective of its specific energy value. At the same time, substantially more power may be drawn from the system in reverse proportion to the power density. The ESSs with high specific energy may be the best choice if the goal is to store energy for longer. As a group member with a reasonably high energy density, the battery might be interested in such energy needs [19-21].

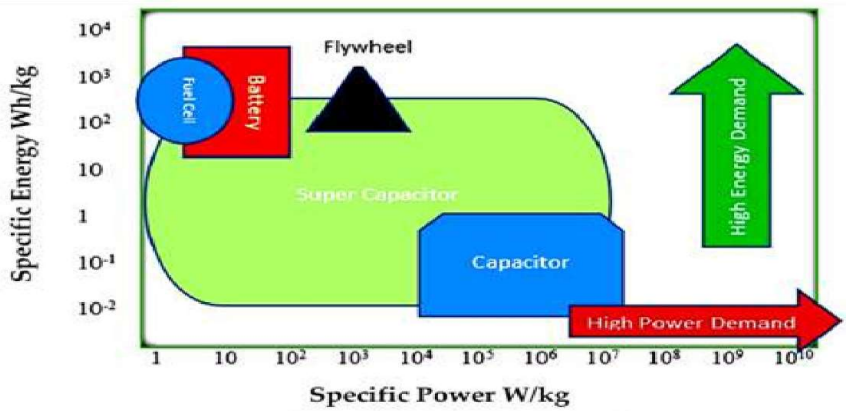

Figure 1. 3 Specific power vs. specific energy for different Energy Storage systems.

1.2 Battery

Electrical energy is stored using battery energy storage systems (ESS) for later use. They are essential in many applications, such as integrating renewable energy, grid stability, load balancing, and backup power. Because they can store and release electrical energy effectively, batteries are the primary technology employed in ESS. The following list of causes and sources are the main reasons to utilize batteries as a popular ESS includes:

Energy density: Batteries can store much energy in a small, light package because of their high energy density. This is essential for applications with limited space or when portable energy storage is required [22].

Efficiency: Batteries have proven attractive for ESS due to their high energy density. Battery round-trip efficiency is high, allowing for efficient energy storage and discharge with little losses. The round-trip efficiency of modern battery chemistries like lithium-ion has surpassed 90% [23].

Rapid response: Batteries can react quickly to changes in the demand for or supply of power. They can swiftly charge and discharge electricity, making them appropriate for applications like grid frequency management that need

speedy responses. This responsiveness helps integrate sporadic renewable energy sources and increases grid stability [24].

Scalability: To satisfy various applications' distinct power and energy needs, battery ESS may be scaled up or down. To enhance capacity or voltage, more battery modules may be linked in parallel or series. Because of their adaptability, batteries may be used with various system sizes and designs [25].

Lifespan and cycle life: Emerging battery technologies, exemplified by lithium-ion batteries, exhibit extended operational lifetimes and demonstrate resilience in enduring several charge-discharge cycles. Long-term energy storage applications may benefit from the battery's economic viability by adequately managing and operating it [26].

In the following scenarios, more in-depth insights will be investigated, focusing on battery energy storage systems [27].

1.2.1 Battery Principle

A battery is a type of electrochemical arrangement that facilitates the conversion of chemical energy present in its active constituents into electrical energy by means of a redox (reduction-oxidation) reaction. Within the framework of a rechargeable system, the battery undergoes a reversal of its operational process in order to initiate the recharging procedure. The process described involves the movement of electrons from one substance to another across an electric circuit. In non-electrochemical redox reactions, such as the processes of rusting or burning, electron transfer takes place through direct means, wherein heat serves as the sole kind of energy involved. The battery performs an electrochemical process whereby chemical energy is transformed into electrical energy. In contrast to combustion or heat engines, batteries are not subject to the restrictions of the Carnot cycle as dictated by the second law

of thermodynamics. The electrochemical unit commonly referred to as a "battery" is more accurately described as a "cell." A battery is composed of one or more interconnected cells arranged in either a series or parallel arrangement, or a combination of both, depending on the desired output voltage and capacity. [28].

The cellular structure comprises three primary constituents, namely the anode, cathode, and electrolyte. During the electrochemical reaction, the anode, also known as the negative electrode, releases electrons to the external circuit and undergoes oxidation. Simultaneously, the cathode, also known as the positive electrode, undergoes reduction as it receives electrons from the external circuit during the electrochemical reaction. The electrolyte serves as the conduit for the movement of charge, in the form of ions, throughout the cell, facilitating the transfer between the anode and cathode. The electrolyte is commonly a liquid medium, such as water or other solvents, which contains dissolved salts, acids, or alkalis in order to facilitate the flow of ions. Certain types of batteries utilize solid electrolytes, which exhibit ionic conductivity when the cell is running at its designated temperature.

When connecting the two electrodes of a battery within an electrical circuit, the electrolyte initiates a process of active decomposition. Over time, the chemical constituents transform into alternative compounds, such as ions or an excess of electrons generated by the electrode components. The conducting ions participate in a chemical reaction that involves the electrolyte. Simultaneously, the transfer of electrons occurs between the terminals via the external circuit. The procedure above persists until the electrolyte undergoes complete conversion. At a certain point, the movement of ions within the electrolyte and electrons through the outer circuit stops, resulting in the total discharge of the battery. The discharge and charge process is illustrated consecutively in Fig.1.4 (a, b).

During the process of discharge, the cell establishes a connection with an external load, resulting in the flow of electrons from the anode. This flow causes oxidation at the anode, while the electrons traverse the external load and reach the cathode. At the cathode, the electrons are accepted, leading to reduction of the cathode material. The completion of the electric circuit within the electrolyte occurs by the movement of anions (negatively charged ions) and cations (positively charged ions) towards the anode and cathode, respectively.

Oxidation: $Y \longrightarrow Y^{+}+e^{-}$ Eq: 1.1

Reduction: $Z + e^{-} \longrightarrow Z^{-}$ Eq: 1.2

Overall Cell Reaction (discharge): $Y+Z \longrightarrow Y^{+}+Z^{-}$ Eq: 1.3

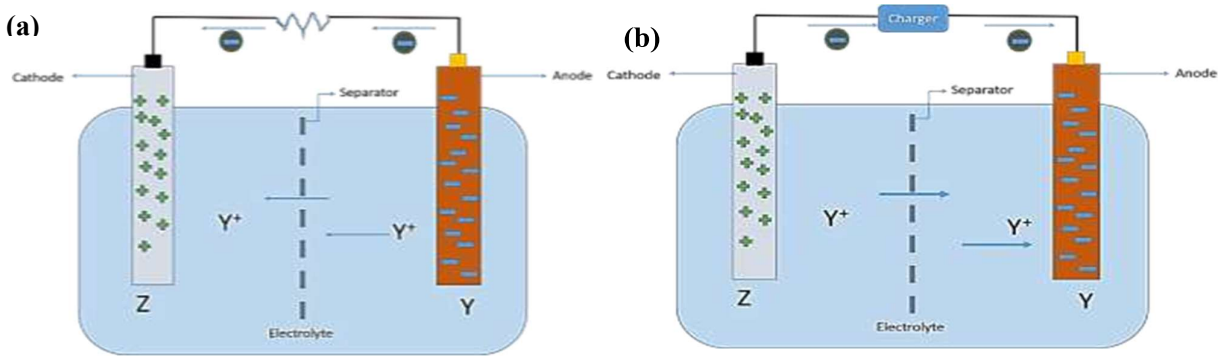

Figure 1. 4 Battery with (a) discharging, (b) charging.

Conversely, in the process of recharging a rechargeable or storage cell, the direction of current flow is reversed, leading to oxidation at the positive electrode and reduction at the negative electrode. According to the definition, the anode is the electrode where oxidation takes place, while the cathode is the electrode where reduction occurs. Consequently, the positive electrode is designated as the anode, while the negative electrode is referred to as the cathode.

Reduction:	$Y^{+}+e^{-} \longrightarrow Y$	Eq: 1.4
Oxidation:	$Z^{-} \longrightarrow Z + e^{-}$	Eq: 1.5
Overall Cell Reaction (charge):	$Y^{+}+Z^{-} \longrightarrow Y+Z$	Eq: 1.6

1.2.2 Battery Types

Battery classification is based on the capacity for recharging, resulting in two distinct categories: main batteries and secondary batteries. Primary batteries are not capable of being efficiently recharged using electrical means and can only be discharged once. The primary cell, which lacks a free or liquid electrolyte, contains the electrolyte within an absorbent or separator material. These cells are commonly referred to as "dry cells". The primary battery serves as a pragmatic and economical solution for supplying portable electronic and electric devices, lighting systems, photographic equipment, toys, memory backup systems, and a range of other applications with a convenient and easily accessible source of packaged power. This feature enables autonomy from the electrical grid and improves the usability of these devices. Primary batteries provide numerous advantages, such as prolonged storage capability, a high level of energy density when discharged at low to moderate rates, minimum maintenance demands, and user-friendly operation. Primary batteries of large capacity are commonly employed in military applications, signaling, standby power, and other similar situations. The majority of primary batteries are composed of single-cell cylindrical and flat button configurations, as well as multi-cell batteries that integrate these individual cells. Secondary batteries possess various distinctive characteristics, such as their ability to undergo recharging, their high-power density, their higher discharge rate, their consistent discharge curves, and their excellent performance even in low-temperature environments. In contrast to primary batteries, secondary batteries generally exhibit lower

energy densities. The capacity to retain their charge is relatively lesser in comparison to primary batteries. Nevertheless, the diminished performance of the secondary battery resulting from inactivity can be restored through the process of recharging.

There are different types of primary batteries, including Zinc Carbon cells, Zinc Alkaline Manganese Dioxide cells, Zinc Mercuric Oxide cells, Cadmium Mercuric Oxide cells, Silver Oxide cells, Zinc Air cells, Magnesium cells, Aluminum cells, Lithium cells, Solid Electrolyte cells. The prevalent type of primary cell is the battery composed of zinc and acidic manganese dioxide. Despite their extended shelf life, they offer limited energy [29]. Alkaline zinc-based primary cells are known to provide extended shelf life and significant power output [30]. The Lithium primary cell, primarily used for military purposes due to safety concerns, exhibits a long shelf life of ten years [31]. The extensive utilization of silver oxide primary batteries is hampered by the expensive nature of silver, despite their remarkable energy density [32]. Zinc-air cells have emerged as the prevailing industry standard for hearing aid batteries. The extended operation of the device is attributed to its utilization of solely anode material and the surrounding air's oxygen as a cathode, as stated in reference [33].

The focus on primary cell batteries is transitioning towards secondary cell batteries due to certain limitations associated with primary cells, such as their single-use nature and low energy efficiency of approximately 2% over their lifespan. Numerous types of secondary batteries have been discovered. Rechargeable alkaline batteries are a type of secondary battery that is cost-effective and has a prolonged shelf life, albeit with a relatively lower cycle life. These devices are primarily utilized for power needs of a moderate scale and purportedly do not present any concerns regarding the disposal of toxic byproducts [34].

Nickel-Cadmium (Ni-Cd) rechargeable batteries are known for their durability and reliability. These devices are capable of functioning across a broad spectrum of temperatures and demonstrate extended durability, as well as higher specific power density. The extensive utilization of cadmium is impeded by several drawbacks, including its high discharge rate of 30% per month, toxicity, carcinogenic properties, non-recyclability, and memory effect. Due to their low internal resistance and ability to deliver high surge current, wireless devices such as wireless telephones, emergency lighting, aircraft starting batteries and electric vehicles have increasingly favored these batteries [35].

The focus on primary cell batteries is transitioning towards secondary cell batteries due to certain limitations associated with primary cells, such as their single-use nature and low energy efficiency of approximately 2% over their lifespan. Numerous types of secondary batteries have been discovered. Rechargeable alkaline batteries are a type of secondary battery that is cost-effective and has a prolonged shelf life, albeit with a relatively lower cycle life. These devices are predominantly employed for the purpose of charging Nickel-Metal Hydride (Ni-MH) batteries, which can be considered as modified versions of Ni-Cd batteries. Ni-MH batteries exhibit a 30% higher capacity than their Ni-Cd counterparts, possess a prolonged cycle life, and demonstrate commendable high-rate capability. In addition, it is noteworthy that these materials do not pose a challenge regarding toxic waste disposal, as they do not contain cadmium. However, it should be noted that the presence of cobalt and nickel oxide, though in small quantities, can have carcinogenic properties. Additionally, these batteries exhibit memory effect and a notable self-discharge rate of 40% per month [36, 37].

Lead-acid batteries, which were initially discovered by French physicist Gastone Pante in 1859, have gained significant popularity as rechargeable

battery. Although rechargeable batteries of this type demonstrate a lower energy density compared to other types, they can deliver high surge current, thereby resulting in a high power to weight ratio of the cell. Lead-acid batteries are cost-effective, making them a desirable choice for autonomous vehicles. These are primarily favored for providing a high surge current to their starter motor. Various lead-acid batteries are commercially accessible, each designed to adapt to specific applications. These include deep-cycle batteries, VRLA batteries, AGM batteries, and gel batteries. Due to their significant mass, portable consumer applications do not utilize them. Additionally, lead (Pb) exhibits elevated toxicity levels and is associated with carcinogenic properties. It is noteworthy that a significant proportion of lead-acid batteries, approximately 90%, can be effectively recycled to manufacture new lead-acid batteries, as evidenced by sources [38, 39].

Aluminum-based batteries that are rechargeable possess low flammability and are cost-effective. Additionally, their high capacity is attributed to their three-electron-redox characteristics. The expected safety advantages of utilizing aluminum in this battery type are attributed to its inertness and ease of handling in a natural environment. Additionally, aluminum exhibits a greater volumetric capacity than other metals such as lithium, potassium, and others. The substance in question shows a notable density of $2.7 gcm^{-3}$ at 25 °C and can undergo a three-electron exchange. This observation implies that, in terms of volume as a metric, the energy density of aluminum-based batteries is somewhat greater than that of batteries utilizing alternative metals. As a result, it is expected that aluminum-based batteries will demonstrate decreased physical size. Aluminum-ion batteries exhibit a greater number of charge-discharge cycles as compared to competing battery technologies. Therefore, it has been suggested that Al-ion batteries have the potential to take the place of Li-ion batteries [40-42].

At present, rechargeable Calcium batteries exhibit lower energy densities and capacity degradation in comparison to Li-metal batteries. Nevertheless, concerted efforts are being made to tackle these issues. The migration rate of calcium ions is seen to be quite low during their traversal over the solid electrolyte interface (SEI). Dendritic development occurs within calcium metal under conditions of strong electric current. The nature of calcium deposits plays a crucial role in the extended performance of batteries, and efforts are being undertaken to produce consistent and high-quality deposits. In order to get energy densities that are on par with the existing Li-ion and Li-metal batteries, the utilization of a pristine calcium (Ca) metal anode is required for calcium batteries. The higher hardness of calcium in comparison to lithium needs the inclusion of calcium foils in battery manufacturing methods, such as pouches and cylinder cells, in order to ensure proper integration [43, 44].

The drawbacks associated with the aforementioned rechargeable batteries have dampened the enthusiasm for the advancement of rechargeable battery technology. A novel rechargeable battery technology is currently under development, effectively addressing all the drawbacks of the prior rechargeable battery technologies. The most recent version of the Lithium-ion battery (LIB) functions by utilizing the migration of lithium ions (Li+) to produce energy. The LIBs are lightweight, have a rapid charging capability, and exhibit a longer lifespan compared to other conventional batteries. In addition, lithium-ion batteries (LIBs) exhibit superior stability and can undergo hundreds of recharge cycles. In comparison to alternative rechargeable batteries, these batteries show a superior energy density, increased specific capacity, and reduced self-discharge rate. Thus, this exhibits excellent power efficiency and capacity retention compared to the aforementioned types. This thesis will provide a comprehensive

understanding of LIBs, which will be further elaborated in subsequent sections.

1.3 Lithium-ion Batteries (LIBs):

1.3.1 Prospects of LIBs

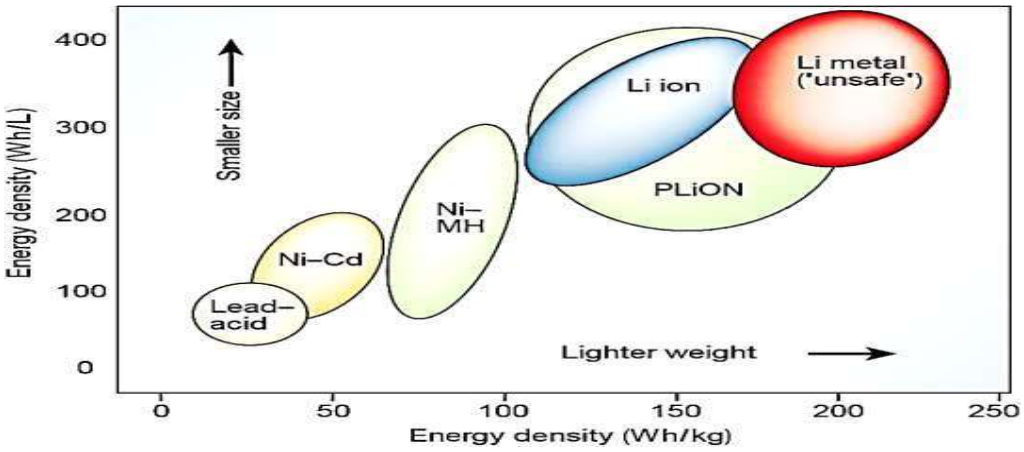

Figure 1. 5 Specific energy density ($WhKg^{-1}$) vs. volumetric energy density (WhL^{-1}) of different batteries (Adapted from [45]).

LIBs have contributed major improvements in the contemporary era of portable electronic gadgets, including laptops, smartphones, and digital cameras. In addition, the lightweight nature of this specific battery has made it the predominant choice for pure electric vehicles (PEV), plug-in hybrid vehicles (PHEV), and hybrid vehicles (HEV). The reason for the lightweight characteristic of Lithium-ion batteries (LIBs) can be traced to their high energy density per unit weight and volume, as depicted in Figure 1.5. The battery has an extended duration of storage and employs energy technology that is environmentally sustainable. Additionally, its manufacturing process is characterized by increased ease and efficiency. The sources mentioned above have reported that these items' production cost is low and exhibit no memory effect [46-49]. Thus, these characteristics enhance the appeal of this battery.

The discovery of lithium, also known as "lithion/lithina," dates back to 1817 when Arfwedson [50] and Berzelius [51] analyzed petalite ore ($LiAlSi_4O10$). However, it was not until 1821 that the element was successfully isolated through the electrolysis of lithium oxide by Brande and Davy [52]. Lewis delved into the electrochemical properties of the aforementioned substance a century after its discovery [53]. Given lithium's favorable physical characteristics, including its low density ($0.534gcm^{-3}$), high specific capacity ($3860mAhg^{-1}$), and low redox potential (-3.04V vs. SHE), it was promptly recognized that lithium had the potential to function effectively as a battery.

The commencement of the comprehensive investigation into the complete capabilities of Li-ion technology was instigated in 1912 by G.N Lewis, who served as the dean of the chemistry department at the University of California Berkeley [53]. The introduction of commercially accessible non-rechargeable lithium-ion batteries was pioneered in the early 1970s, after the proposal of M.S. Whittingham at Exxon [54]. The batteries were manufactured utilizing titanium disulfide (TiS_2) as the cathode and lithium metal as the anode. While the positive cathode had acceptable performance, the lithium metal anode exhibited uneven dendrite growth during the cycling process, as illustrated in Figure 1.6.

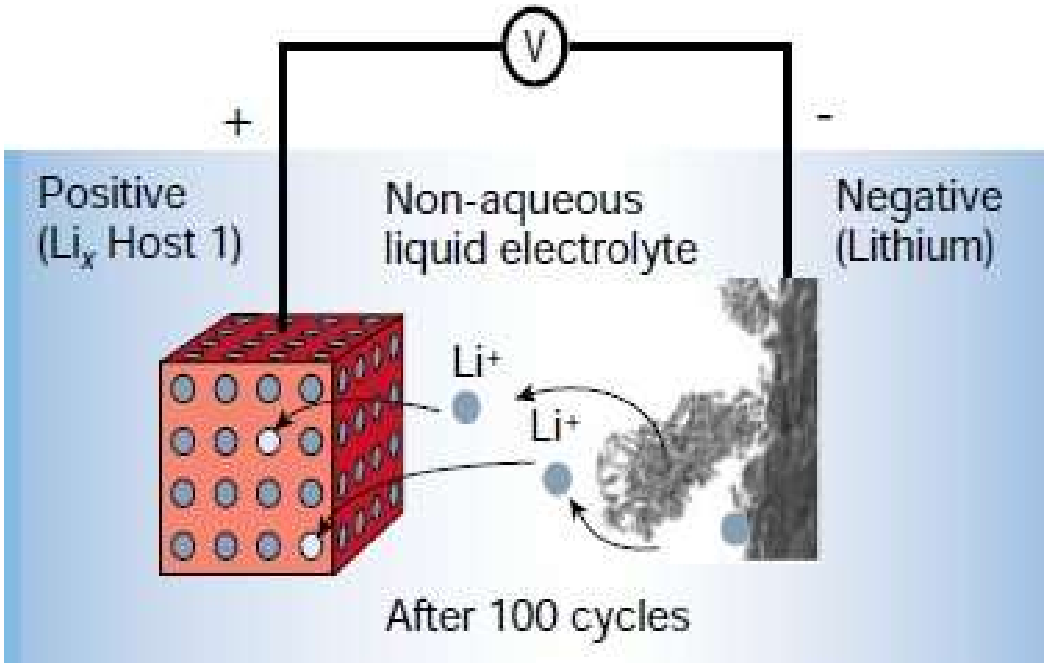

Figure 1. 6 Dendrite formation on lithium anode (Adapted from [55]).

The identification of the intercalation materials, which employ lithium as an insert material for rechargeable battery packs, signifies a significant advancement in the evolution of lithium batteries. In the year 1986, Rachid Yazami and his colleagues conducted an experiment to illustrate the electrochemical properties of lithium the intercalation in graphite, as depicted in Figure 1.7. This finding was documented in reference [56].

In the 1970s, John Goodenough, a chemist, and his research team from Oxford University, consisting of Phil Wiseman, Koichi Mizushima, and Phil Jones, initially introduced the concept of the Lithium-ion battery. The research was published during the 1980s. In the year 1991, Sony Corporation initiated the commercial release of lithium-ion batteries, employing graphite as the anode material. This choice was decided based on the material's widespread availability and its theoretical specific capacity of 372mAhg^{-1} [57]. While lithium-ion batteries possess sufficient characteristics to be considered a viable energy storage solution, enhancing their energy efficiency is imperative

for responding to the increasing energy requirements of the contemporary world. There has been a discernible rise in the utilisation of lithium-ion batteries (LIBs) across many domains, including robotics, continuous energy supply (UES), various power tools, and static power storage systems. Furthermore, it is important to highlight that automobiles intended for long-distance travel require a minimum specific energy density of lithium-ion batteries ($150 Whkg^{-1}$), which is five to ten times higher than the previously indicated number [58, 59]. According to Figure 1.8, there has been an increase in the reliance on and usage of Lithium-ion batteries (LIBs) over time. It is imperative to introduce modifications to the current conventional materials utilized in batteries to achieve significantly improved energy efficiency. Delaying such action is not a viable option.

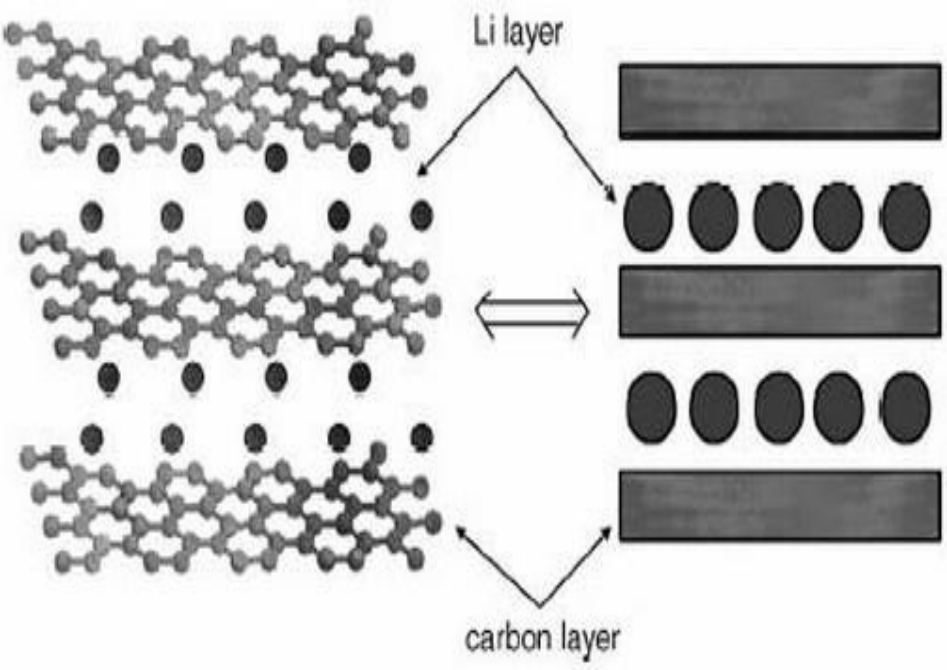

Figure 1. 7 Structure of graphite intercalated with lithium (Adapted from [60]).

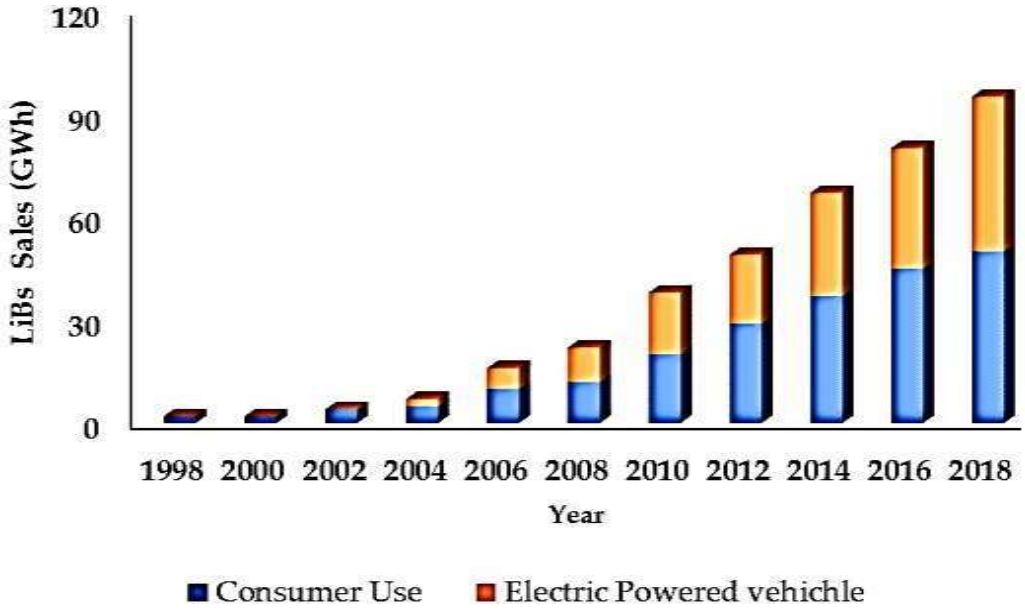

Figure 1. 8 Scenario of increasing demand of LIBs.

1.3.2 Electrochemistry of LIBs

An electrical battery is a composite of one or several electrochemical cells that enable the transformation of accumulated chemical energies into electricity.

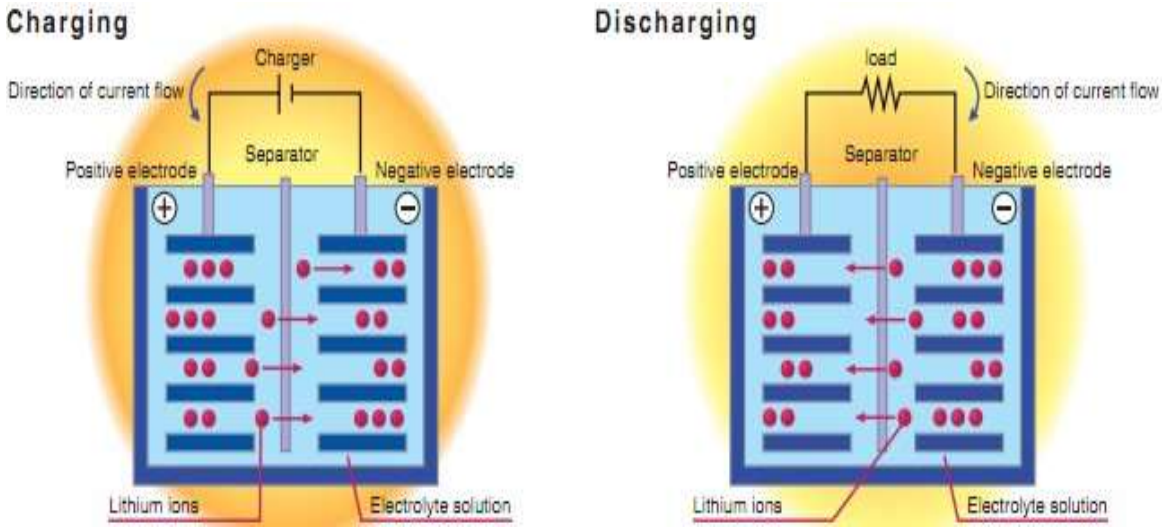

Figure 1. 9 Diagram of Li-ion cell during charging and discharging (Adapted from [61]).

There are two main classifications of batteries, known as primary and secondary. Primary batteries are distinguished by their lack of rechargeability, which is attributed to the irreversible chemical process occurring within the battery. As a result, once a primary battery has been utilized, it must be discarded instead of being subjected to the process of recharging. Secondary batteries exhibit the capacity to undergo recharging and subsequent usage on multiple occasions. A lithium-ion battery is commonly referred to as a rechargeable battery that utilizes chemical processes involving the intercalation of lithium ions between the cathode (positive electrode) and the anode (negative electrode) to store energy. During the process of charging and discharging cycles, the migration of lithium ions between the cathode and anode takes place, resulting in their commonly referred to nomenclature as "Rocking-chair" batteries [62]. The lithium-ion battery consists of four fundamental components: the anode, cathode, separator, and electrolyte, which can be comprised of various materials. The cathode operates as a positively charged electrode that undergoes reduction through the acceptance of electrons, whereas the anode performs as a negatively charged electrode that provides electrons and experiences oxidation throughout the discharge cycles. The electrodes maintain electrical connectivity via the electrolyte, while the separator serves the dual purpose of preventing electrode intermixing and allowing ion passage.

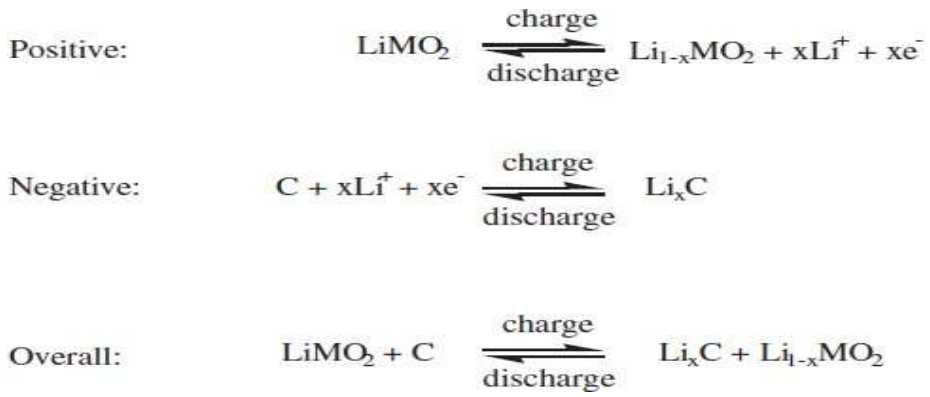

Figure 1. 10 Electrode and cell reactions in a Lithium Ion battery (Adapted from [63]).

To obtain a succinct comprehension of this procedure, let us analyze the instance of a traditional $LiCoO_2$ battery, where $LiCoO_2$ serves as the cathode. During the process of charging, there is a migration of lithium ions from the cathode to the anode. Simultaneously, the presence of an external field assists in the extraction of electrons from the cathode and subsequently transports them to the anode. During the process of discharge, the anode liberates ions to the solution of electrolyte and provides electrons for the external circuit. Subsequently, these ions undergo intercalation within the cathode, while electrons generated by the external circuit are employed to uphold charge balance. The processes of intercalation and de-intercalation refer to the insertion and extraction, respectively, of Li+ ions from electrodes [64, 65]. The following redox reaction is depicted below.

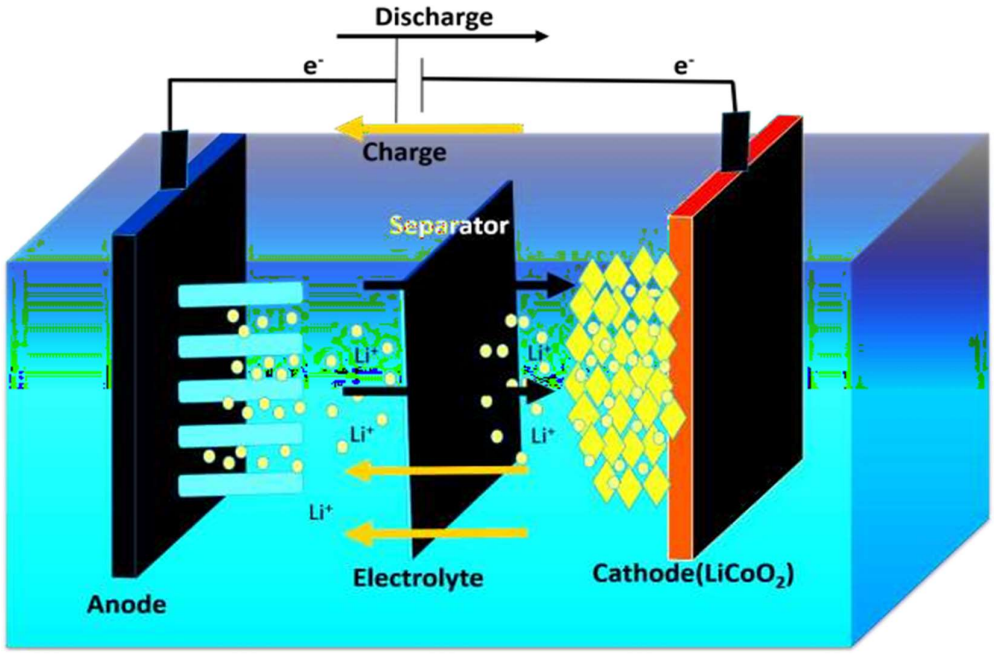

Figure 1. 11 Skeleton of LiBs showing Li+ intercalation/de-intercalation mechanism.

1.3.3 Advantages of LIBs

The property which makes LIBs advanced from others is energy density. It exhibits energy density of 100Whg^{-1}–265Whkg^{-1}. So, it can store energy for a long time supporting the portable application-based fields. Here some of the main advantages of LIBs are given below:

High Energy Density: Lithium-ion batteries exhibit a notably higher energy density than alternative rechargeable battery technologies. This characteristic enables them to achieve a higher energy density in terms of mass and volume, rendering them highly suitable for applications that prioritize limitations in space and weight [66]. They can supply up to 3.6 Volts, which is almost three times greater than their nickel counterparts.

Long Cycle Life: Lithium-ion batteries exhibit a prolonged cycle life, as they can endure numerous charge and discharge cycles without experiencing

substantial deterioration in their capacity. The extended lifespan of these entities renders them well-suited for enduring purposes, such as using electric vehicles and grid energy storage systems [67].

Low Self-Discharge Rate: Lithium-ion batteries exhibit a comparatively reduced self-discharge rate compared to alternative rechargeable battery technologies such as nickel-based chemistries. LIBs have a lengthy shelf life because of their modest self- discharge rate of 1.5-2 percent each month. Lithium-ion batteries can retain their charge for prolonged durations, rendering them advantageous for applications involving sporadic usage, such as emergency backup systems [68].

Rapid Charging: Lithium-ion batteries can undergo rapid charging at a significantly accelerated pace compared to alternative battery technologies. The field of lithium-ion battery chemistry and engineering has witnessed notable progress, leading to the development of enhanced rapid charging capabilities. This advancement has reduced periods of inactivity and enhanced user convenience [55].

No Memory Effect: Lithium-ion batteries have the advantageous characteristic of not being subject to the memory effect. This phenomenon leads to reduced battery capacity as a result of incomplete discharging or charging. This sets them apart from certain other rechargeable battery types. This functionality enables users to recharge the battery at their convenience without causing any detrimental impact on its overall performance.

Lightweight and Compact: Lithium-ion batteries are renowned for being lightweight and compact. The attribute above confers significant benefits in the context of portable electronic devices, including smartphones, laptops, and tablets [66].

Environmentally Friendly: Lithium-ion batteries are commonly regarded as more ecologically sustainable than specific alternative battery chemistries, such as lead-acid batteries. The diminished dependence on hazardous substances and the potential for recyclability of these materials contribute to decreased environmental consequences [69].

1.3.4 Challenges of LIBs

The commercial implementation of lithium-ion batteries has been accomplished with success for a duration of nearly two decades. The present condition of battery chemistry suggests that the technology can be considered somewhat developed. Lithium-ion batteries have become the dominant preference for portable electronic gadgets, including cell phones and laptop computers. Electric vehicles are progressively acquiring a more prominent role. Lithium-ion batteries are increasingly considered a feasible choice for integration into sustainable energy systems due to their capacity to efficiently store renewable energy generated by sustainable sources. The growing demand for energy storage compels the development of present lithium-ion battery technologies and the emergence of next-generation lithium-ion batteries, with a particular focus on cost reduction. The task of developing alternative battery chemistry as a substitute for the existing lithium-ion battery technology continues to be a significant and difficult obstacle.

In order to increase the energy density of lithium-ion batteries, it is beneficial to identify electrode pairs that exhibit both high-specific capacities and high operating cell voltages. As previously said, there is a diverse array of prospective options for anodes that possess the capacity to greatly boost specific capabilities. Significantly, there has been a notable focus on anodes utilizing silicon (Si) and tin (Sn) materials, mostly due to their attractive characteristics. The production of Si nanomaterials on a large scale

while maintaining low cost remains a significant challenge. Tin-based anodes exhibit suboptimal cycling performance as a result of pulverization. Hence, it is plausible that Si-Sn-based composites could serve as potential future anodes [70].

In contrast with the candidates for the anode, the fundamental constraint on the number of cells is mostly ascribed to the limited capacity of the candidates for the cathode. The existing cathode material, namely $LiCoO_2$, is characterized by its significant expense and considerable toxicity. The $LiFePO_4$ battery, which has experienced an increase in its level of acceptance, demonstrates a comparatively limited capacity. The cathodes, which have been created by Argonne National Laboratory and are based on the Ni-Co-Mn composition, can be readily manufactured and have generated substantial attention, particularly within the industrial sector. However, it should be noted that the specific capacity remains at a moderate level, and it is important to acknowledge that both cobalt (Co) and nickel (Ni) are widely known for their elevated expenses and poisonous properties. From an environmental standpoint, future cathode materials should avoid incorporating toxic elements such as Co or Ni.

Additionally, it is imperative for the cathode to possess the ability to effectively and reversibly inject or withdraw numerous electrons per 3d metal. Possible cathode materials for future cost-effective applications encompass those derived from manganese (Mn) and/or iron (Fe). The issue of intrinsically limited conductivity calls for an innovative strategy, potentially leveraging the field of nanotechnology and nano-composites. The present cathode candidates under investigation have little potential for improving the working cell voltages. Composite cathodes composed of two or three transition metals from the 3d series, along with polyanions, demonstrate considerable potential. There is a possibility that novel cathode chemistry

could be developed within the upcoming decade. The novel cathode chemistry may necessitate the use of novel electrolytes as well.

The safety issue presents an additional obstacle that necessitates appropriate attention and resolution. The recent fires involving Li-ion batteries, specifically those occurring in Boeing 787 passenger aircraft and Tesla Model S cars have brought attention to the criticality of battery safety. In order to promote the widespread adoption of electric vehicles and facilitate the growth of the market for vehicles powered by lithium-ion batteries, automakers must make substantial investments in battery management systems. These technologies play a vital part in augmenting the safety of the expansive battery packs employed in automobiles. To effectively mitigate safety problems, it is crucial to investigate the advancement of lithium-ion batteries that possess nonflammable properties. This encompasses the examination of lithium-ion batteries employing aqueous electrolytes or ceramic electrolytes, alongside the exploration of all-solid-state batteries. The upcoming generation of lithium-ion batteries is expected to include cathodes featuring high voltage levels of approximately 5V, together with anodes possessing high capacity. These advancements may involve the utilization of materials such as silicon (Si) or tin (Sn). Hence, conducting thorough research to enhance our comprehension of electrode materials, particularly their stability and interaction with electrolytes, is imperative. Rather than solely prioritizing the intensive pursuit of high-energy density, it is imperative to place a growing emphasis on ensuring battery safety. The widespread implementation of standardized battery safety testing protocols is imperative.

The continuous issue lies in the development of electrode materials that possess a minimal carbon footprint, generally referred to as "green batteries." Ideally, future lithium-ion batteries should incorporate electrodes sourced from organic or inorganic materials originating from biological sources, while

employing an aqueous electrolyte. Biomasses has the inherent capacity to function as viable sources for the generation of carbon and silicon. The exploration of viruses as a means to fabricate electrode materials for lithium-ion batteries has recently attracted considerable attention [71]. The study of large-scale chemical reactions at ambient temperature, with biological templates such as genetically engineered viruses, is a fascinating area of investigation. The advancement of sustainable lithium-ion batteries shows promise with the further development of organic electrodes that demonstrate resistance to disintegration by electrolytes [72]. Hence, a potential avenue for further investigation could involve directing attention toward developing environmentally sustainable lithium-ion batteries.

In addition, it is crucial for next studies on batteries to incorporate the life cycle assessment (LCA) of these technologies to determine their environmental sustainability. The purpose of this assessment is to determine the extent to which the batteries may be categorized as environmentally sustainable. Further research is needed to investigate the life cycle assessment (LCA) of the current materials used in commercial lithium-ion batteries. These materials include cathodes such as $LiCoO_2$, $LiMn_2O_4$, $LiNiO_2$, and $LiFePO_4$, anodes such as graphite and $Li_4Ti_5O_{12}$, and electrolytes/salts such as ethylene carbonate, diethyl carbonate, $LiPF_6$, $LiBF_4$, and $LiClO_4$. Additionally, the separators used in these batteries are typically made of polypropylene and polyethylene. Limited information exists regarding the environmental ramifications associated with the manufacturing, utilization, and disposal of forthcoming Li-ion batteries [73]. The exponential growth in the production of lithium-ion batteries for electric vehicles will result in the generation of significant amounts of environmentally detrimental trash and the establishment of disposal facilities.

The proximity of mine sites may reduce agricultural productivity, while the presence of processing facilities could result in a decline in air quality. Additionally, establishing factories near may contribute to an increase in energy costs. Moreover, an increase in fossil fuel consumption may be necessary to satisfy factories' manufacturing requirements for Li-ion batteries. The Life Cycle Assessment (LCA) methodology provides a complete framework for evaluating the environmental characteristics and potential consequences associated with a given product or process across its full life cycle. This comprises a range of steps, which include the acquisition of raw minerals, the production process, utilization, end-of-life treatment, recycling, and final disposal. Hence, life cycle assessment (LCA) emerges as a significant instrument for advancing environmentally friendly lithium-ion batteries, fostering future sustainability. Another crucial domain that warrants appropriate consideration is lithium-ion batteries' techno-economic analysis (TEA). The Technical and Economic Assessment (TEA) will be utilized to ascertain the technical and economic viability of the newly developed lithium-ion battery system for potential large-scale manufacturing. Integrating life cycle assessment (LCA) and techno-economic analysis (TEA) methodologies will contribute to advancing future lithium-ion batteries, resulting in enhanced social, environmental, and economic outcomes. There is an increasing worldwide inclination towards the advancement of "Nano" materials with the aim of augmenting the storage capacity of forthcoming Li-ion batteries. The potential of nano-materials is of great importance due to the widely acknowledged understanding that the electrochemical properties of these materials are dependent on their size and form. The field of battery research has witnessed a substantial surge in interest over the past two decades, with "nanotechnology" emerging as a particularly noteworthy area of focus. However, it is important to acknowledge that the energy density, specifically in terms of volume, of nanomaterials is frequently disregarded,

primarily because of their low volumetric density. The considerable discrepancy in tap densities observed between graphene and MCMB graphite powder serves as a clear illustration of the problem of low tap density. As an example, the tap density of graphene, a material of great interest, is determined to be 0.03g/cc, but MCMB graphite powder exhibits a tap density of 1.3g/cc. This leads to a volumetric disparity of approximately 40-fold for a specified mass. Further considerations pertaining to electrode materials at the nano encompass inferior electrical characteristics arising from interparticle resistance, as well as diminished Coulombic efficiency coming from side reactions occurring between the electrode and electrolyte. These issues are further worsened by the increased surface area.

In addition, it is worth noting that the electrochemical properties of micromaterials demonstrate a level of performance that is comparable to that of nano-materials. There is a need for improvement in the design of devices that utilize Li-ion batteries in order to provide sufficient room for absorbing these batteries. This is particularly evident in the context of cell phones and electric vehicles. In essence, future electrode materials must possess a high tap density. Future research in battery technology should focus on developing next-generation batteries that are smaller yet offer improved performance compared to current battery models (Figure 1.12).

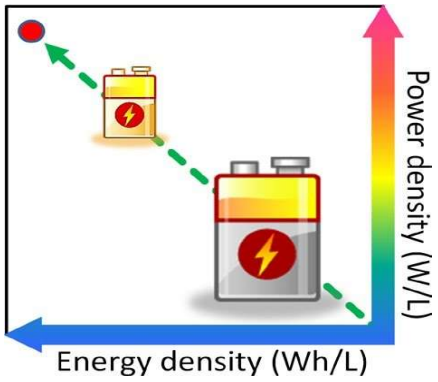

Figure 1. 12 The illustration to demonstration that future Li-ion batteries should be light and small without any compromise on energy and power (Adapted from [74]).

1.4 Cathode

$LiCoO_2$ is the cathode material frequently used in lithium-ion batteries [75]. The compound $LiCoO_2$ adopts the α-$NaFeO_2$ crystal structure, characterized by a distorted rock-salt arrangement, wherein the cations exhibit ordering in alternating (1 1 1) planes. The arrangement of atoms in this particular configuration leads to the formation of a trigonal structure with the space group notation $R\bar{3}m$. In the case of $LiCoO_2$, specific planes consisting of lithium ions facilitate the process of lithiation and de-lithiation [76]. While $LiCoO_2$ has proven to be an effective cathode material, researchers are actively exploring alternative options to reduce costs and enhance stability. Cobalt demonstrates a more restricted availability, leading to elevated pricing in comparison to other transition metals such as manganese, nickel, and iron. Moreover, it should be noted that $LiCoO_2$ exhibits lower stability compared to alternative electrode materials, rendering it susceptible to performance deterioration or even failure under overcharging conditions [77-79]. According to previous research [80], augmenting the charging voltage can potentially enhance the cell's capacity. However, it is essential to note that this increase in voltage may also result in a more accelerated decline in capacity as the cell undergoes recharging cycles. Multiple factors have contributed to the deterioration observed during the cycling process. An element worthy of

attention pertains to the phenomenon of cobalt dissolution occurring within the electrolyte during the process of de-lithiation of the electrode, namely during the charging phase [81]. This phenomenon leads to a decrease in the ability of lithium to undergo intercalation during the process of discharge. An additional aspect that warrants consideration is the development of the CoO_2 layer subsequent to full de-lithiation, resulting in the separation of said layer from the electrode's surface [82]. The following separation results in a reduction in the ability for lithium intercalation. Moreover, it is important to acknowledge that there is a substantial change in the lattice parameter when the lithium content is altered [83]. This phenomena has the potential to generate internal tensions and micro-cracks within the cathode particles [84]. The acquisition of stoichiometric $LiCoO_2$ can pose challenges [85], thus necessitating heat treatment to regulate the surface phase composition to enhance cycling performance [86].

$LiNiO_2$, which exhibits the α-$NaFeO_2$ crystal structure, is characterized by a lower cost and a higher energy density (15% higher by volume, 20% higher by weight) [87]. However, it is worth noting that $LiNiO_2$ is less stable [88, 89] and exhibits a lower degree of order [90] when compared to $LiCoO_2$. The reduced level of organization leads to the placement of nickel ions within the lithium plane, which hinders the process of lithiation and de-lithiation. Additionally, this situation presents difficulties in achieving the desired composition [91]. The introduction of cobalt into $LiNO_2$ results in an enhanced level of organization, resulting in the preferential placement of nickel ions within the nickel/cobalt plane as opposed to the lithium plane [92]. $LiNi_{1-x}Co_xO_2$, which predominantly consists of nickel ($x \sim 0.8$), has been employed to capitalize on the cost-effectiveness and greater capacity of nickel compared to cobalt [93-97]. The compound $LiMnO_2$ exhibits a monoclinic crystal structure instead of a rhombohedral structure [98]. The monoclinic structure has the ability to

undergo a transition into a layered hexagonal structure throughout the cycling process. [99]. The incorporation of nickel [100, 101], or more frequently nickel and cobalt, into $LiMnO_2$ has the potential to create the α-$NaFeO_2$ crystal structure [102, 103]. The lattice characteristics of the trigonal lattice, particularly the ratio of c/a, demonstrate a correlation with the composition. As the aforementioned ratio approaches the value of 1.633, the departure from cubic symmetry decreases.

As a result, there is a reduction in the ordering process, leading to an increased concentration of transition metal ions within the lithium-ion plane. The $Li(Ni,Mn,Co)O_2$ composition, which is widely utilized, consists of equal proportions of the three transition metals, specifically $Li(Ni_{1/3}Mn_{1/3}Co_{1/3})O_2$. This composition exhibits a high capacity [104], favorable rate capability [105, 106], and can function at elevated voltages. An elevated charging voltage has been found to enhance the capacity but is also associated with accelerated capacity degradation during cycling [107-109]. Similar to $LiNi_{1-x}Co_xO_2$, the inclusion of cobalt in the composition aids in diminishing the quantity of nickel present in the lithium layer [92]. Previous studies have demonstrated that adding small quantities of cobalt (up to 0.20–0.25) can enhance capacity [109-115]. The inclusion of higher levels of cobalt has been found to have the potential to mitigate capacity degradation during cycling [109, 116-118]. The enhanced operational efficiency has been ascribed to the influence of cobalt, which leads to an increase in conductivity [109, 117] and an enhancement in the cathode's structural stability [117, 118]. Although the inclusion of nickel in the ion layer may have negative implications for lithium transport, scholarly investigations have revealed that it can also bolster the integrity of the framework during de-lithiation, hence resulting in enhanced cycling performance. [119]. The enhancement of electrode performance through over-lithiation of $Li(Ni,Mn,Co)O_2$ has been observed, particularly in cases when the

cobalt concentration is minimal [120-122]. During the first cycle, there may be an occurrence of oxidative loss that is not recovered in following cycles [123]. However, prior research has indicated that deep discharging has the ability to successfully repair the initial capacity loss that is detected during the initial cycle [124].

The cathode material $LiMn_2O_4$ shows potential because of the spinel structure ($Fd3^{-}m$). Within this particular arrangement, the octahedral sites are predominantly occupied by manganese, whilst the tetrahedral sites are primarily occupied by lithium. [125]. In this particular scenario, it is observed that the pathways for the process of lithiation and de-lithiation exhibit a network of channels in three dimensions, as opposed to planes, as observed in the α-$NaFeO_2$ structure. $LiMn_2O_4$ is considered to be a more cost-effective and safer alternative to $LiCoO_2$ [92, 126, 127]. Nevertheless, it is important to acknowledge that $LiMn_2O_4$ demonstrates a reduced capacity in comparison to cathode materials that adopt the α-$NaFeO_2$ structure, as previously described. [104, 128]. One of the main challenges associated with the utilization of $LiMn_2O_4$ as a material for the cathode is to the occurrence of phase shifts throughout the cycling process [129-131]. An instance of field testing involved the utilization of $LiMn_2O_4$ cathodes within the direct current power supply of a functional telecommunications transceiver. During the experimental trial, there was an initial rapid decline in capacity within the first few days, followed by a subsequent decrease in the rate of capacity loss [132]. The primary cause of the initial loss has been ascribed to oxygen depletion during the charging process [133]. The phenomenon of capacity loss has also been documented in storage settings, primarily attributed to the dissolution of manganese in the electrolyte [134]. Furthermore, the occurrence of capacity loss can be attributed to changes in particle shape or crystallinity [135, 136]. Additional transition metals, such as iron [137] and cobalt [138-143], have

been incorporated into $LiMn_2O_4$. The presence of iron results in the appearance of an additional discharge plateau at higher voltages, while cobalt improves the capacity retention during repeated cycles by stabilizing the crystalline structure of the spinel material. Nevertheless, nickel is frequently incorporated into $LiMn_2O_4$ [144], decreasing both the lattice structure characteristic and the electric conductivity of $LiMn_2O_4$ [145]. The capacity of the material exhibits an upward trend as the manganese content is increased, particularly when maintaining a 3:1 ratio of manganese to nickel (i.e., $Mn_{1.5}Ni_{0.5}O_4$). This specific composition ($Mn_{1.5}Ni_{0.5}O_4$) is widely utilized in various applications [146, 147]. The arrangement of manganese and nickel cations on the octahedral sublattice has been observed. However, research has demonstrated that a disordered spinel structure exhibits a greater capacity [148]. The utilization of cobalt as a partial substitute for nickel (specifically, in the form of $Li[Mn_{1.42}Ni_{0.42}Co_{0.16}]O_4$) has been employed to mitigate the formation of $Li_xNi_{1-x}O$. This compound can detrimentally impact the cell's performance during cycling [149]. Using nickel as a surface coating on $LiMn_2O_4$, as opposed to its incorporation as a bulk dopant, has also demonstrated efficacy in enhancing capacity retention during cycling [150-152].

The layered structure of vanadium oxide enables it to exist in several valence states. As a result, vanadium oxides have been utilized as electrode materials in many applications. Specifically, cathode materials such as orthorhombic V_2O_5 [153-157] and monoclinic LiV_3O_8 [158-162] have been employed. The electrodes exhibit significant capacities, albeit with comparably lower voltages (usually 3V or lower) than the aforementioned compounds.

Phosphates with the chemical formula $LiMPO_4$, which possess the olivine crystal structure with the space group Pnma, are considered a promising class of cathode materials. inside this particular arrangement, the phosphorous

atoms are situated inside tetrahedral sites, whereas the transitional metal (M) atoms are positioned within octahedral sites. Furthermore, it should be noted that lithium atoms exhibit a tendency to arrange themselves in linear chains in the [0 1 0] crystallographic direction [163]. In general, the cathode commonly utilizes $LiFePO_4$ as the predominant phosphate molecule. During the de-lithiation process, Fe^{2+} undergoes oxidation to Fe^{3+}, leading to the creation of FePO4. [164]. The introduction of iron ions into lithium sites results in the formation of vacancies that accommodate lithium ions, hence maintaining charge neutrality [165-167]. A miscibility gap exists between $FePO_4$ and $LiFePO_4$ [168], resulting in a de-lithiation process characterized by the growth of a two-phase front rather than a continuous alteration in lithium content [169-174]. The establishment of a two-phase mixture contributes to the attainment of a stable level of activity, which in turn leads to a discharge profile characterized by a generally constant voltage [46]. The electronic conduction in $LiFePO_4$ is primarily facilitated by slight polaron hopping, as evidenced by previous research [175]. It is worth noting that the conductivity of pure $LiFePO_4$ is relatively low, measuring at approximately 10^{-9} Scm^{-1} [92]. The enhancement of conductivity can be achieved through heat treatment, which increases hole conductivity [176]. However, to achieve satisfactory performance, it is generally necessary to introduce a conductive phase [177]. The subsequent section will address the additives employed to enhance the conductivity of $LiFePO_4$. It is worth noting that the inclusion of Fe_2P, a conductive phase, has been observed to enhance the performance of $LiFePO_4$ during both preparation and utilization [178, 179]. Consequently, deliberate incorporation of Fe_2P is occasionally practiced in producing $LiFePO_4/Fe_2P$ composites [180-183]. The significance of Fe_2P lies in its impact on conductivity, whereby minimal quantities enhance it, while excessive quantities impede the paths of lithium ions [184].

Additional phosphates utilized as cathodes in lithium-ion batteries include $LiMnPO_4$ [185-187] and $LiCoPO_4$ [187, 188]. According to a study [92], $LiMnPO_4$ and $LiCoPO_4$ exhibit higher open circuit voltages of 4.1V and 4.8V, respectively, compared to $LiFePO_4$, which has a voltage of 3.5V. However, it should be noted that both $LiMnPO_4$ and $LiCoPO_4$ have lower capacities. The study by [187] revealed that the capacities of LiMnPO4 and $LiCoPO_4$, which were synthesized using microwave hydrothermal synthesis, were approximately one-sixth and one-third, respectively, compared to $LiFePO_4$ synthesized using the same method. Furthermore, it has been observed that $Mn_2P_4O_7$ and $Co_2P_4O_7$ are formed in de-lithiated $LiMnPO_4$ [186] and $LiCoPO_4$ [188] electrodes, respectively. This formation process leads to a degradation in the lifetime of the electrodes and raises safety concerns due to the evolution of oxygen during the decomposition reaction. Cathode materials have been utilized as mixtures of phosphates, such as $LiMnPO_4$ [189-191] or $LiCoPO_4$ [192, 193], in combination with $LiFePO_4$. The operating voltage of these mixtures demonstrates an upward trend as the manganese content increases [194, 195]. Conversely, the capacity of the mixtures exhibits a positive correlation with the iron content [192, 193, 196]. While $LiNiPO_4$ does exhibit the olivine structure [163], it is not commonly employed as a cathode material. In addition, nickel has been incorporated into various phosphate cathode materials, such as lithium transition metal phosphates (e.g., $LiFePO_4$ [197, 198] and $LiMnPO_4$ [199]), as well as more intricate compounds like $Li(Mn,Fe)PO_4$ [200, 201] and $Li(Mn,Fe,Co)PO_4$ [202, 203]. $Li_3V_2(PO_4)_3$ is an additional phosphate compound employed as a cathode material. It exhibits a monoclinic crystal structure with the space group $P2_1/n$ [204, 205]. $Li_3V_2(PO_4)_3$ exhibits a significantly elevated operating voltage and demonstrates commendable efficacy when subjected to high discharge currents, as evidenced by previous studies [206, 207]. Previous studies have reported the existence of plateau voltages exceeding 4V for discharge currents ranging

from 0.2C to 2C, as well as plateau voltages surpassing 3.9V for a discharge current of 10C [207]. Previous studies have demonstrated that including vanadium can enhance the capacity of $LiFePO_4$, particularly under conditions of high discharge currents [197, 208, 209]. As an illustration, when the temperature is at 0.1C, the enhancements in capacity are relatively moderate, ranging from 5% to 15%, according to sources [197, 208, 209]. However, at a higher temperature of 10C, significant capacity increases have been documented, ranging from 80% to over 200% [208, 209]. The positive impact of incorporating vanadium into the system has been ascribed to two main factors: the improvement of lithium diffusion [197, 209] and the reduction of energy needed for the nucleation of $LiFePO_4$ in the $LiFePO_4$–$FePO_4$ [208] two-phase region.

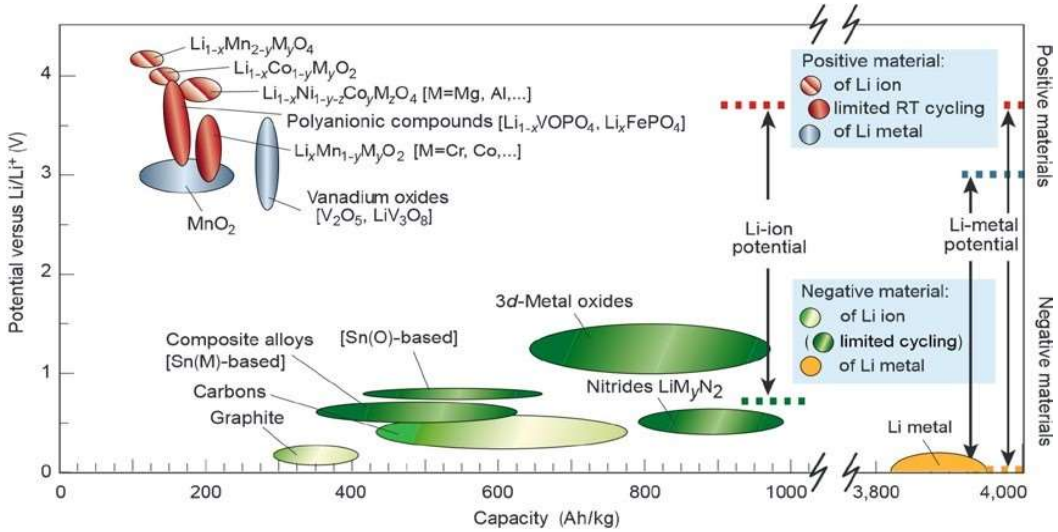

Figure 1. 13 The relationship between voltage and capacity is a critical aspect of the positive and negative electrode substances currently employed or being contemplated for the forthcoming generation of lithium-ion batteries (Adapted from [55]).

1.5 Anode

The prevailing rechargeable lithium-ion battery available in the market has carbon as the active ingredient for the anode. Graphite is composed of ABAB layers that are interconnected through van der Waals forces. Within each layer, there exists a conjugated sp2 bond structure. When lithium ions are

inserted between these layers, the arrangement of the layers is altered to AAA^{2-}. Graphite functions as the host matrix for lithium intercalation, exhibiting sufficient structural robustness to enable reversibility by facilitating the straightforward insertion and removal of lithium ions. Graphite exhibits a diverse range of forms, encompassing crystalline structures and nearly amorphous states. The components utilized in the fabrication of anodes consist of a range of primary substances, including natural graphite, which oil pitch, tar from coal, hydrocarbons gas, benzene, and different resins, among other substances. These anodes can be classified into three categories: (1) graphite, (2) non-graphitized glass-like carbon (also known as hard carbon), which retains its non-graphitic structure even when subjected to high-temperature heat treatment, and (3) soft carbon, which exhibits a high degree of malleability upon heat treatment. The diagram illustrating the structural characteristics of these carbon entities is presented in Figure 1.14 [210]. Anodes commonly employed in various applications include graphite and hard carbon materials. In practical applications, graphite has been observed to readily incorporate an adequate amount of lithium at standard room temperature, forming LiC_6. Upon subsequent removal of lithium ions, this compound exhibits a discharge capacity of 372 milliampere-hours per gram (mAh/g). Numerous researchers have documented the process of lithium intercalation into graphite and have extensively studied the electrochemical properties of graphite anodes [211-213] . Dahn et al. have provided a complete description of the relationship between the electrolytic insertion of lithium and the crystal structure of several carbon materials. Figure 1.15 [214] displays the charge-discharge curve of graphitized, micron-sized mesocarbon microbeads (MCMB).

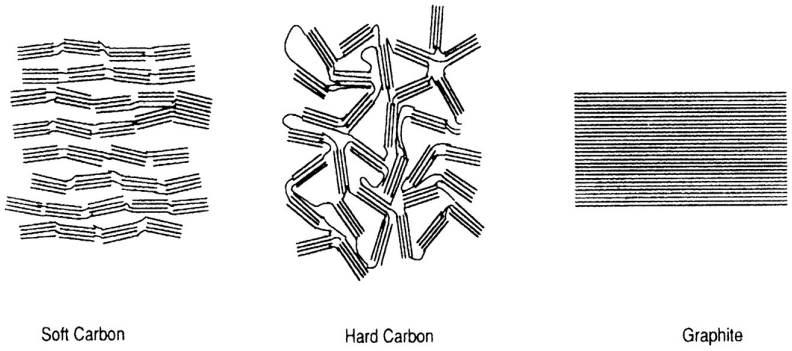

Figure 1. 14 Three types of carbon (Adapted from [215]).

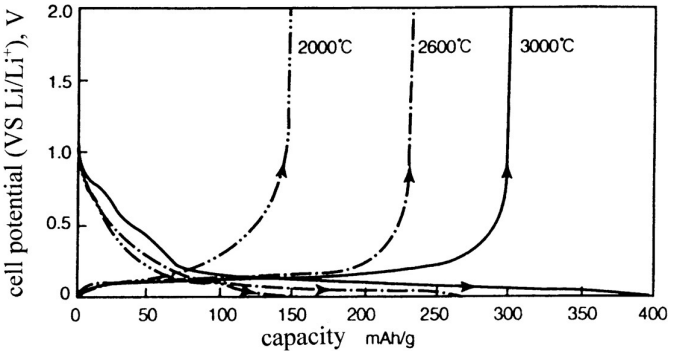

Figure 1. 15 Charge–discharge curve of MCMB heat treated at various temperatures (Adapted from [215])

The graphite anode, which has been subjected to sintering at a temperature of 3000°C, demonstrates a charging capability of 400 milliampere-hours per gram (mAh/g). Nevertheless, the capacity experiences a notable decrease to 290mAh/g throughout the discharge process. The topic under consideration pertains to the phenomenon of irreversible reaction, particularly the retention that takes place during the first charging procedure for graphite. The occurrence of this chemical process results in the creation of a slender layer consisting of athe lithium-ion conductive substance referred to as the interface of solid electrolytes (SEI) on the graphite's exterior. In the framework of graphite, it is evident that the charging and discharging voltage has a consistent and invariant profile. This characteristic remains unchanged when graphite is coupled with a cathode, preserving the flat voltage discharge

pattern. The discharge characteristic described is a fundamental necessity in most compact electrical devices. In contrast, the incorporation of lithium in hard carbon derived from the polycondensation of oil pitch occurs not only within the interlayer spaces of the carbon structure but also within the crevices between crystal particles, commonly referred to as doping sites. Consequently, this phenomenon enables hard carbon to accommodate a more significant amount of lithium predicted by the LiC_6 formula, thereby transforming it into a high-capacity anode. Figure 1.16 [216] displays the charge-discharge curve for the initial cycle of a representative hard carbon material, specifically pseudo-isotropic carbon (PIC).

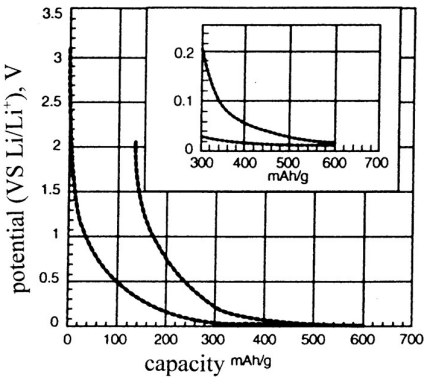

Figure 1. 16 Charge–discharge curve of a hard carbon (PIC) (Adapted from [215]).

Numerous theoretical frameworks have been put out to elucidate the microstructural attributes of hard carbon, wherein the presence of microcavities, encompassing pores and voids, is a prominent feature. [217]. Certain carbon materials have been hypothesized to exhibit intercalation or absorption of lithium ions within graphene layers [218]. In the case of hard carbons, the retention of irreversibility during the first cycle and the associated potential change resulting from intercalation exhibit significant differences when compared to graphite. The discharge voltage of hard carbon as an anode material exhibits a gradual temporal variation. The discharge

above pattern facilitates a straightforward assessment of the remaining capacity of the cell. Moreover, in the case of cells with varying initial discharge voltages due to capacity imbalances in a battery, connecting them in parallel results in a balanced voltage being maintained across the entire battery system during discharge.

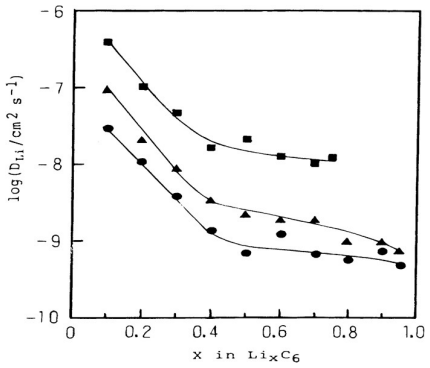

Figure 1. 17 Variation of chemical diffusion coefficient of lithium in carbons ((solid square) mesophase pitch-based carbon fiber heated at 3000°C; (solid triangle) artificial graphite; (solid circle) natural graphite) in 1 M $LiPF_6$–EC/DEC (1:1) electrolyte (Adapted from [215]).

Carbon anodes demonstrate a restricted energy capacity, and the velocity of Li^+ ion diffusion through carbon interlayers is comparatively sluggish. The interdependence between the chemical diffusion coefficient ($\tilde{D}$) of Li^+ in graphite and the power density of a battery is significant. The observed $\tilde{D}$ value of a certain graphitized carbon fibre is approximately ten times higher than the $\tilde{D}$ value found in natural graphite, as illustrated in Figure 1.17. [219]. In a recent study conducted by Takamura et al. (2013), it was shown that the application of metallic Ag, Zn, or Sn using evaporated layer deposition on the complete surface of a graphite fibre exhibits considerable promise in augmenting charging and discharging reaction rates. The creation of a novel solid electrolytes interphase (SEI) on the metal surface is the most feasible reason for the observed phenomenon. Based on a report, there is data indicating that the electrical charging ability of B-doped mesophase pitch-

based carbon fibre (MPCF) demonstrates an approximate 10% augmentation, coupled by an improved cycle efficiency [220].

The pursuit of more advanced and efficient anode materials has prompted the exploration of alloy anodes utilizing tin (Sn) [221] and silicon (Si) [222] . Despite the high capacity of approximately 800-3000mAh/g exhibited by lithium intercalated into Li_4M-$Li_{4.4}M$ (where M represents a metal), the cycling performance was not stable because of changing volume exceed four times during lithium insertion. The utilization of an oxide anode has also been suggested, with investigations conducted on various tin oxides [223], In VO_4 [224], $FeVO_4$ [224], and Brannerite-type MnV_2O_6. Most of these oxides transition from a crystalline structure to an amorphous state upon lithium intercalation. Figure 1.18 depicts the structural arrangement of Brannerite. The initial intercalation process demonstrates a notably high $1000mAhg^{-1}$ capacity. However, subsequent observations reveal a significant irreversible reaction and decreased lithiation capacity. The issue of significant capacity degradation during cycling needs to be addressed for practical applications. It is hypothesized that the oxide materials' stability can be improved by selectively substituting certain transition metals with other elements.

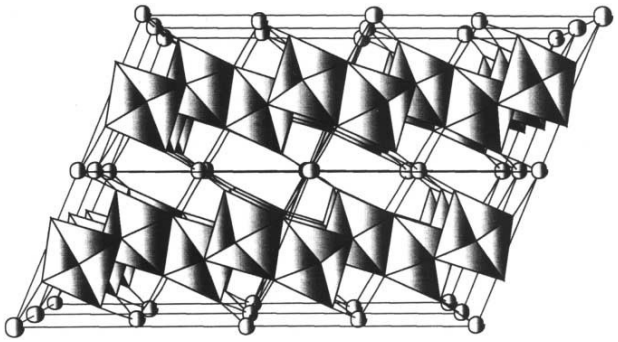

Figure 1. 18 Structure of Brannerite. Mn is represented by the circles and vanadium is located in the center of each octahedron (Adapted from [215]).

Table 1. 1 Different Anode materials for LIBs [225].

Anode	Capacity (Theoretical)	Advantages	Challenges
Alloy/de-alloy materials a. Silicon b. Germanium c. Tin d. Antimony	4212 1621 993 660	Higher specific capacities, High energy density, Good safety	Large irreversible capacity, Huge capacity fading, Poor cycling
Conversion materials a). Metal oxides (Fe_2O_3, Fe_3O_4, CoO, Co_3O_4, Mn_xO_y, Cu_2O/CuO, NiO, Cr_2O_3, etc.)	500 – 1200	High capacity, High energy, Low cost, Environmentally compatibility,	Poor capacity retention, Short cycle life, High cost of production, Low columbic efficiency,
b). Metal phoshides/sulfides/nitrides (MXy; M ¼ Fe, Mn, Ni, Cu, Co etc.)	500 - 1800	High specific capacity, Low operation potential, and Low polarization than counter oxides	Unstable SEI formation, Large potential hysteresis, Poor cycle life
Insertion/de-insertion materials A. Carbonaceous a. Hard carbons b. CNTS c. Graphene	200 – 600 1116 700/ 1116	Good working potential, Low cost. Good safety	Low columbic efficiency, High voltage hysteresis, High irreversible capacity
B. Titanium oxides		Extreme safety,	Very

a. $LiTi_4O_5$ b. TiO_2	175 330	Good cycle life, low cost High power capability	low capacity, Low energy density

1.5.1 Alloying/Dealloying Mechanism:

The mechanism of alloying/dealloying facilitates the storage of lithium in silicon and tin, as indicated by previous studies [226-228]. In an electrochemical lithiation process, the anode materials of the alloying type engage in a chemical reaction with lithium, leading to the creation of various alloys based on lithium. This reaction might take place either via a solid solution or through an addition reaction. [229]. The method of de-lithiation enables the separation of lithium from alloying-type anode materials. The subsequent reactions elucidate the mechanism underlying the process of alloying and dealloying:

$$xLi^{+} + xe^{-} + M \rightarrow Li_xM; \quad \text{Where, (M= Si, Sn, Ge, Pb, etc.)} \quad \text{Eq: 1.7}$$

where M denotes a metal or an alloy compound. During the lithiation process, it is observed that there is no alteration in phase or structure when lithium (Li) is introduced into the solid solution reaction with M. Nevertheless, a modification in the phase structure does transpire when M undergoes lithiation, resulting in the formation of Li_xM by the process of addition. The electrochemical processes pertaining to lithium and both amorphous and crystallized silicon can be classified into two categories: solutions reactions and reactions of addition [229].

Silicon lithiation and de-lithiation occur in multiple stages at varying temperatures [230-234]. The electrochemical reaction occurring among li and silica at a temperature of 415°C is in accordance with the equilibrium state of the Li-Si binary phase diagram. This reaction formed $Li_{12}Si_7$, Li_7Si_3, $Li_{13}Si_4$, and $Li_{22}Si_5$ during the lithiation process, as reported in reference [230]. Nevertheless, the electrochemical process occurring between lithium and silicon at normal temperature conditions was contrary to the state of equilibrium Li-Si binary state diagram, which specifies the completely lithiated phase as $Li_{15}Si_4$. [232]. After the initial alloying cycle, the crystalline silicon demonstrated a significant plateau potential of 0.1V. This potential was consistently observed at 0.4V for all subsequent dealloying cycles [226]. This suggests that silicon's alloying and dealloying process can be attributed to a single two-phase addition reaction. According to X-ray diffraction (XRD) studies [231-234], there was a suggestion that a transformation had place wherein crystalline silicon was converted into an amorphous Li-Si alloy. Following this, the shapeless phase underwent a process of crystallization, resulting in the formation of crystalline Li15Si4 at a voltage of roughly 50mV compared to the Li^+/Li reference electrode during the first cycle of alloying. During the ensuing dealloying process, the crystalline $Li_{15}Si_4$ underwent a conversion into amorphous Li-Si alloys, which was subsequently followed by a transformation from amorphous Li-Si alloys to amorphous silicon. Therefore, the phenomenon of relithiation, which entails the interaction between amorphous silicon and lithium, can be characterized as a solid solution. This characteristic explains the absence of distinct plateau potential regions commonly observed during the reaction.

In the context of alloying-type materials, significant volumetric variations arise due to phase transitions during the electrochemical processes of lithiation and de-lithiation. The significant fluctuations in volume give rise to

considerable mechanical stresses, which can be alleviated using cracking and pulverization. Consequently, the integrity of the connection of electricity between the particles that are active and the electrically conductive matrix is damaged, resulting in their subsequent loss [226, 235-240]. The fundamental factor that contributes to the insufficient cycle durability and kinematics of alloying-type anode components is the main reason. The effectiveness of minimizing substantial volume changes through the reduction of bulk substances to the nano is generally acknowledged. The electrochemical properties of nanostructured materials are enhanced as a result of several factors, including a shortened diffusion length, greater structural integrity, enhanced ionic/electronic conductivity, and an increased number of active sites for the storage of lithium through electrochemical processes..

1.5.2 Conversion Mechanism

Several transition metal oxides, including CoO, Fe_2O_3/Fe_3O_4, and CuO, have been observed to exhibit a conversion reaction mechanism during the electrochemical process of lithium storage [241, 242]. In the lithiation process, it is common for metal oxides to undergo conversion into metallic clusters that are embedded within a Li_2O matrix. Subsequently, these metallic clusters transfer back into metal oxides during the de-lithiation process. The de-lithiation process encompasses the irreversible reduction and oxidation reactions of metal oxides, which are followed by the creation and subsequent consumption of Li_2O. The chemical equation provided can be employed to understand the reaction mechanism involved in the transformation of metal oxides.

$$M_xO_y + 2yLi^+ + 2ye^- \rightarrow yLi_2O + xM; \quad \text{Where M= Metal} \qquad \text{Eq: 1.8}$$

Within the given structure, the sign "M" is representative of a metallic element. It is vital to recognise that phase structures of anode materials of

conversion reactions undergo modifications subsequent to the lithiation process. The process of lithium storage in conversion reaction-type anode The process of components involves the transfer of many electrons.

The influence of discharging/charging rate and the characteristics of the active material, including crystallite dimensions and specific surface area, have been reported to affect the reaction pathway for the lithiation/de-lithiation of anode materials with conversion reaction-type behavior. [243]. The reported lithiation reaction pathways of Co_3O_4 were found to exhibit variations depending on current density and size of the crystallite. The observed variation can be ascribed to the presence of two antagonistic reactions occurring during the early phase of lithiation. Figure 5 illustrates the schematic depiction of the two unique reaction paths that can be seen throughout the lithiation procedure for Co_3O_4 [243]. The formation of a CoO/Li_2O composite is favoured during the initial lithiation stage when Co_3O_4 is highly divided and/or a low discharge current is applied. As the lithiation process continues, this composite transforms into a metallic Co/Li_2O composite. In another approach, the formation of $Li_xCo_3O_4$ was observed under conditions involving active materials characterized by a significant crystallite size and/or the application of a high discharge current. Following that, the aforementioned compound followed a comparable breakdown mechanism, resulting in the formation of a composite consisting of metallic Co and Li_2O [243]. Thackeray et al. (year) also reported the presence of the $Li_xCo_3O_4$ phase in their study on the quick chemical lithiation process. In the context of the lithium storing reaction using Co_3O_4, it was observed that a total of eight electrons were transported.

Chen et al. revealed the influence of geometry on the electrochemical lithium storing characteristics of conversion reaction-type materials. The lithium capacity for storage and cycling reversibility exhibited by Co_3O_4 nanotubes

were found to be superior in comparison to both nanoparticles and nanorods. During the electrical conversion process, substantial structural reorganisation and volumetric alterations occur, resulting in the segregation of nanoparticles and the development of fissures within the active materials. Therefore, the aforementioned phenomenon leads to the detachment of Li_2O from the metal particles, leading to a gradual decrease in electrochemical capacity with each successive cycle. Nanostructured anode materials demonstrate markedly improved cycling characteristics in comparison to their bulk counterparts. The observed enhancement can be ascribed to the decrease in volumetric fluctuations of the particles and the mitigation of active material fracturing. In addition, the retention of lithium ions inside the interface, surface, and nanopores in the converting reaction-type materials could potentially account for the observed connection between morphological and lithium capacity for storage.

1.5.3 Intercalation/De-intercalation Mechanism

The fundamental principle underlying the intercalation method involves the reversible incorporation of lithium ions (Li+) into the anode's layered structure. The phenomena of interlayer gap expansion between two layers during insertion is commonly attributed to the influence of the forces of van der Waals. The process of expansion is made possible through the exchange of energy resulting from the potential for redox reactions that exists between the solid materials of the guest and host.

The absence of excess mass in pure lithium renders it a prime candidate for ideal anode material. However, the propensity for dendrite formation during the charging process can lead to internal short circuits. Additionally, it exhibits a low Columbic efficiency. When considering safety concerns, it is worth examining different types of lithium titanate (LTO), such as $Li_4Ti_5O_{12}$. The material is categorized as a zero-strain materials owing to its negligible

volume fluctuation of about 2% throughout the process of intercalation, leading to a notably stable cycle performance. During the course of this investigation, the researchers observed the occurrence of shrinkage or stretching in the Ti-O bonds as a result of the intercalation or de-intercalation of Li+ ions. This observation allowed for the characterization of the structure, which exhibited a lower electron conductivity of 10-13 Scm^{-2}. The commercial utilization of LTO in electrochemical energy storage systems is constrained by gas formation resulting from the interfacial reactivity between the surface and electrolytes. Therefore, it is necessary to conduct further investigations in order to improve the low reversible specific capacity of 175$mAhg^{-1}$, which is approximately half of the theoretical capacity of bulk TiO_2 (335$mAhg^{-1}$) [69, 244]. Furthermore, the issue of sudden voltage drop can be effectively addressed by creating a nanocomposite consisting of $Li_4Ti_5O_{12}$ and $Li_2Ti_3O_7$ [245]. The observed reversible capacity of layered Li_3VO_4 is 2.5 times greater than that of $Li_4Ti_5O_{12}$. However, it has been reported that Li_3VO_4 exhibits a high rate of capacity fading and poor rate performance. [246]

The capacity of soft carbon is relatively low, while its hysteresis voltage is significant. Therefore, these constraints impose restrictions on its potential as a feasible anode material for future generations of batteries made from lithium- (LIBs). Contrarily, there is a significant focus on the hard carbon material owing to its notable reversible capacity of 500$mAhg^{-1}$. However, the diffusivity of electrons exhibits a slow behaviour, leading to a limited rate capability. As reported in numerous articles, the reversible capacity typically falls within the range of 200 – 600$mAhg^{-1}$. However, its extensive utilization is hindered by low tap density and suboptimal columbic efficiency. Therefore, the application of a thin layer of soft carbon demonstrates subsequent enhancements. [247]

In a recent study, the utilization of carbon nanotubes, or CNTs, as a potential insertion anode material has been described. The study reports a specific capacity of 1168 $mAhg^{-1}$, which is considered noteworthy. The observed phenomena can be ascribed to the process of lithium intercalation into stable pseudo graphite layer sites that are situated both on the outermost layer and within the walls of the tubes. However, despite demonstrating promising electrochemical performances, the mass production and cost-effectiveness of carbon nanotube (CNT) technology remain significant barriers to its maturity. [248-250]

Graphene, a lattice arrangement composed of sp2 carbon atoms, frequently exhibits a notable specific capacity within the 790 – 1050 $mAhg^{-1}$ range. The researchers reported an initial capacity of 1200 $mAhg^{-1}$ and a reversible capacity of 850$mAhg^{-1}$ after 40 cycles. However, the presence of disordered surfaces can lead to diminished electron conductivity. The van der Waals force acting between neighboring layers leads to a reduction in the particular area of surface, hence causing a decline in the specific capacity. [251, 252].

Titanium dioxide (TiO_2), classified as a member of the group of transition metallic oxides (TMOs), exhibits promising characteristics that make it a viable contender for use as the anode material in lithium-ion batteries (LIBs). However, specific characteristics can be derived from others. Titanium dioxide (TiO_2) possesses a range of favorable attributes, rendering it a viable selection for anode material in diverse applications. The attributes of this material encompass a high energy density, an operating voltage of 1.7V compared to Li/Li^+, the capability to hinder the development of a solid electrolyte the interphase (SEI) layer, notable electroactivity, exceptional oxidation characteristics, abundance, diverse allotropy, amazing chemical stability, the ease of large-scale production, structural stability during the process of lithium-ion (Li^+) insertion and de-intercalation (with a change in

volume of less than 4%), favorable capacity retention, and relatively rapid kinetics of Li+ ions. In order to position the material as a viable candidate, it is necessary to address certain limitations. The experimental results indicate that it exhibits relatively lower reversible capacities than other transition metal oxides (TMOs) when subjected to lithium insertion, as demonstrated by Equation (1.9).

$$Li^{+} + TiO_2 + xe^{-} \rightarrow Li_xTiO_2 \quad (0 \leq x\ (\text{molefraction}) \leq 1) \qquad \text{Eq: 1.9}$$

The theoretical capacity of titanium dioxide (TiO_2) is reportedly 335milliampere-hours per gram ($mAhg^{-1}$), with x equal to 1. However, an observed capacity of up to 180 $mAhg^{-1}$ was practically achieved for the corresponding x=0.5. The capacity of the bulk material is significantly enhanced by reducing its size to the nanoscale and selecting an appropriate allotrope, resulting in a maximum reported value of $340mAhg^{-1}$. [253-258]

1.6 Motivation and Research Objective

Certain difficulties have been observed in the utilization of traditional graphite as a material for anodes in lithium-ion batteries (LIBs). Common issues that arise in graphite anodes include the formation of SEI layers, dendritic effects, exfoliation over cycling, toxicity, and structural collapse. The primary impetus behind this thesis stems from the need to address these limitations and explore alternative anode materials that possess desirable properties, with the ultimate goal of proposing a potential replacement for conventional graphite anodes. In light of this matter, TiO_2 has been given careful consideration due to the presence of a range of intrinsic properties mentioned earlier in the preceding section. While the theoretical capacity of TiO_2 is slightly lower at $330mAhg^{-1}$ compared to graphite's capacity of $372mAhg^{-1}$, the focus of research has primarily been on the structural stability of TiO_2.

Titanium dioxide (TiO_2) displays a range of polymorphs, such as anatase, rutile, and brookite, amongst other variations. Anatase is regarded as more desirable owing to its capacity to offer a higher quantity of Li+ insert sites. Once again, the process of nano scaling significantly enhances electrochemical phenomena. The diffusion of Li^+ is contingent upon the particle size, as indicated by Equation (1.10) [259].

$$\lambda = L_{ion}^2/D_{Li} \qquad \text{Eq: 1.10}$$

Within this particular framework, the symbol λ is utilized to denote the duration of diffusion, whereas Lion is indicative of the distance covered during diffusion. Furthermore, DLi represents the measurement of the size of the particles of Li^+. This equation posits that the manipulation of particle size to the nanoscale can potentially augment the process of diffusion. The phenomenon of reducing particle size to the nano has been reported to yield instantaneous improvements in diffusing kinetics and rate performance. These advantages are related to the reduction in diffusion lengths. On the other hand, it has been noted that the particular area of surface exhibits a notable disparity compared to the bulk, thus offering additional substantiation of an augmented electrode-electrolyte interface [260]. It is crucial to emphasize once more that the battery's performance is greatly impacted by the three-dimensional morphology, which possesses a hierarchical structure. This is especially true in the case of the highly organized nanotubular array, where the optimized aspect ratio plays a key role. The particular shape under consideration confers notable benefits by improving the transport characteristics of electrons and lithium within the electrode [261, 262].

The unique nanostructures are the result of various distinct preparation methods employed by different individuals. Anodization is a straightforward

method for the production of TiO_2 nanostructures, particularly porous and tubular films [93]. The main aim of the paper is to present a thorough examination of the manufacturing procedure for a nanostructure, specifically either porous or tube in nature, that is made up of anatase TiO2 and designed for practical applications. This objective will be accomplished by employing a direct anodization method, followed by the subsequent integration of the resulting nanostructure into lithium-ion batteries (LIBs) as an anode materials. The thesis encompasses precise objectives and prospective consequences.

- Fabrication of TiO_2 Nanotubes from pure Ti foil and characterization by using SEM and XRD.
- Use of TiO_2 Nanotubes as anode of high-performance LIBs.
- Analysis of charge-discharge capacity, cycle life and internal resistance of as assembled LIBs.

1.7Thesis Outlines

The present thesis paper, **"Experimental Investigation of Cycling Characteristics of Anatase TiO_2 Nanotubes as Negative Electrode of Lithium-ion Batteries"** encompasses the experimental methodology, morphological analysis, and electrochemical performance evaluation of its anode utilization. This section offers a succinct summary of the chapters encompassed in the aforementioned paper, so providing convenient access to the subject matter and meaning of each individual chapter.

Chapter-01: Introduction

This chapter elucidates the fundamental principles underlying batteries, highlights the significance of batteries, and provides an overview of their various classifications. It also emphasizes lithium-ion batteries (LIBs) and their contributions as a reliable energy support system for both present and future generations. Moreover, this study highlights the active components of LIBs, specifically focusing on the anode material. The objective of this study is to emphasize the constraints associated with traditional graphite and emphasise the advantages of anatase nanotubes made of TiO_2 as a potential alternative for the existing anode in lithium-ion batteries (LIBs).

Chapter-02: Literature Review

This chapter comprehensively reviews the various aspects of nanostructured anatase TiO_2 explored in previous research about work-related applications. This comprehensive discussion encompasses various crystal structures, nanostructures, and techniques associated with nanofabrication, mainly focusing on the anodic oxidation method and its corresponding controlling parameters. Furthermore, an examination of the electrochemical properties of these nanotubes is also undertaken.

Chapter-03: Materials and Methodology

This chapter provides a full exposition of the experimental process, encompassing a meticulous depiction of the experimental configuration, characters, and electrochemical performance evaluations. The chapter also presents information regarding the materials, tools, and instruments used during the experiment.

Chapter-04: Result and Discussion

This chapter presents the results obtained through the application of structural analysis procedures, including SEM, EDX and XRD. The findings are accompanied by appropriate visual representations such as images and graphs. The electrochemical behaviors were examined using appropriate diagrams, and a comparative analysis was conducted among various prepared samples.

Chapter-05: Conclusion

This chapter critically analyses the findings derived from structural and electrochemical analyses by the objectives outlined in this thesis. Additionally, the paper includes suggestions for future research and a discussion of the limitations of the research.

Chapter 02

Literature Review

2.1 Introduction:

The field of batteries for energy has witnessed considerable interest in the domain of nanofabrication. The present focus in the subject of battery chemistry revolves around the careful selection and synthesis of suitable materials, with a particular emphasis on anodes. It is important to remember that the efficiency of batteries is predominantly dependent on the active elements found in both the cathode and anode. A multitude of materials for anodes have been identified, therefore instigating continuous investigations aimed at ascertaining feasible alternatives. The utilization of TiO_2, a transition oxide of metals, as a material for anodes in batteries powered by lithium ion offers a potentially advantageous substitute for traditional graphite. This substitution is made feasible by adjusting the morphology of TiO_2, as graphite is associated with various limitations and drawbacks. Extensive research is currently being conducted on various nanostructures of TiO_2, including their modification techniques, morphological analysis, and electrochemical performances. Utilizing research works from PhD and M.Sc. theses and various web sources can prove beneficial in acquiring knowledge and comprehending the characteristics of TiO_2 anode material. In addition, scholarly publications with notable impact factors such as "Journal of Energy Chemistry," "Journal of Nanomaterials," "Nature Nanotechnology," and "Advanced Materials" are collected and analyzed to derive findings of beneficial characteristics, limitations, challenges, research deficiencies, and potential remedies. The evaluations of these pertinent research studies serve to substantiate the viability of TiO_2 as a potential candidate for anode applications and to advocate for continued research efforts in advancing this material.

2.2 TiO_2 Crystal Structures

The investigation into the use of TiO_2 substances for anode applications may be traced back to the identification of the capability of lithium titanites to conduct lithium insertion activities. The insertion of Li properties of the spinel oxides $Li_{1+x}Ti_{2-x}O_4$, where x ranges from 0 to 1/3, have been extensively investigated and reported by Dahn, Thackeray, Ohzuku, and their colleagues since the early 1990s [263-265]. Both metallic $LiTi_2O_4$ and semiconducting $Li_{4/3}Ti_{5/3}O_4$ ($Li_4Ti_5O_{12}$) demonstrate comparable electrochemical behaviour in terms of Li-insertion, with Li-insertion potentials ranging from 1.36–1.338V for $LiTi_2O_4$ and 1.55–1.562V for $Li_4Ti_5O_{12}$, as reported in references [263]. The titanite electrodes possess a higher potential than Li, rendering them inherently safer than graphite. The utilisation of graphite, which operates at a voltage close to the electroplating potential of Li, gives rise to safety considerations. Based on the given equation, it can be inferred that $Li_4Ti_5O_{12}$ possesses the ability to incorporate lithium, resulting in an approximate capacity of $175mAhg^{-1}$. This determination is based on the total weight of the original host material.

$$[Li]^{8a}[Li_{1/3}, Ti_{5/3}]^{16d}[O_4]^{32e} + e^- + Li^+ \leftrightarrow [Li_2] \quad [Li_{1/3}, Ti_{5/3}]^{16d}[O_4]^{32e} \quad \text{Eq: 2.1}$$

In this particular situation, the superscripts are utilized to denote the number of similar sites possessing Wyckoff symbols within the group of spaces $Fd3^-$ m. The Li-insertion and de-insertion process in Li-titanites is distinguished by little or negligible changes in size and structural strain. As a result, these materials have exhibited a remarkable lifespan in repeated cycles [265]. The diffusion coefficients of Li^+ have been reported to be approximately $10{-}6cm^2s^{-1}$ using neutron radiography [266] and approximately $2 \times 10^{-8}cm^2s^{-1}$ by electrochemistry [267].

The titanites demonstrate a spinel structure that is distinguished by a structure of oxygen atoms in a cubic close-packed configuration. In this particular arrangement, the presence of lithium ions is observed in both the tetra (8a) or octahedral (16c, 16d) positions, but titanium ions exclusively occupy the octahedral sites (16d) within the cubic unit cell ($Fd3^{-}m$)[263-265, 268]. The quantity of unoccupied octahedral sites constrains the Li-insertion capacity. The titanite spinel possesses a framework of $[Li_{1/3}Ti_{5/3}]O_4$, which enables the easy diffusion of Li^+ ions through a three-dimensional network of channels [269]. Additionally, this framework demonstrates minimal expansion in volume even when fully lithiated. Therefore, the little modification in the composition during the process of lithium insert and extraction makes it a highly appealing option for the anode in batteries that need both high rates and prolonged cycle life. Peramunage and Abraham (2016) conducted a study on $Li_4Ti_5O_{12}$/PAN electrolyte//$LiMn_2O_4$ batteries, which exhibited a high level of rechargeability with a columbic efficiency close to 100% when the system was run at a rate of 1C. The authors have made a noteworthy contribution through the introduction of the idea of passivation-free negatively charged electrodes and the utilization of aluminium as the current collector of the anode.

The utilisation of nano-structuring has been employed in order to enhance the characteristics of Li-intercalation in lithium titanites. This is achieved by expanding the surface area of contact of the electrode and electrolyte, as well as improving the transit of charges. The effectiveness of this technique is notable due to the absence of side reactions between lithium titanites and electrolytes that are directly linked to irreversible capacity. In their study, Kim and Cho (2018) fabricated $Li_4Ti_5O_{12}$ nanowires with a diameter of 150nm through the process of heating a combination of $TiO_2 \bullet 1.25H_2O$ nanowires and Li acetates at a temperature of 800°C for 3 hours. The synthesized spinel

nanowires exhibited an initial discharge capacity of 165mAhg^{-1} when tested at a 1/10C rate. Additionally, the nanowires displayed a capacity retention of 93% when tested at a 10C rate, as shown in Figure 2.1. In their study, Kavan and Grätzel [270] documented the characteristics of a thin film-nanocrystalline spinel, which exhibited a thickness ranging from 2.0 to 6.0nm. The researchers observed that this particular spinel demonstrated a superior rate to composite spinels. Nanostructured lithium titanites exhibit higher efficiency due to their nano-structuring, together with their inherent structural stability, favorable interface chemistry, and safety features. These characteristics make them a highly viable alternative for inexpensive, lasting, high-power lithium-ion batteries. The utilizations of nanostructured titanites as anodes in readily accessible lithium battery systems has demonstrated their viability for widespread use.

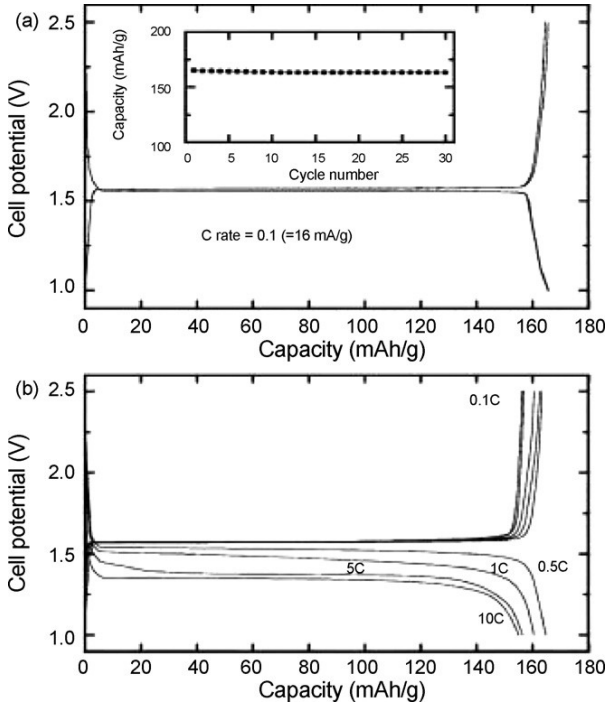

Figure 2. 1 Voltage profiles of (a) $Li_4Ti_5O_{12}$ nanowires in a coin-type half-cell and discharge capacity as a function of cycle number and (b) rate capability test of the $Li_4Ti_5O_{12}$ nanowires at different C rates (0.5, 1, 5 and 10C). The charge rate was fixed at 0.1C (=16mA g^{-1}) (Adapted from [271]).

Recently, there has been a growing interest in exploring the potential Li-insertion properties of titanite spinels. This has led to a heightened focus on investigating different nanostructures of TiO_2 polymorphs, specifically for their applicability in Li-ion battery systems. Although $Li_4Ti_5O_{12}$ demonstrates favourable characteristics as a host material for reversible Li-insertion/extraction, its specific capacity is constrained to a maximum of 175mAhg^{-1}. When comparing different materials, it is observed that TiO_2 can reach its theoretical capacity of 335 or 1.0 Ti per TiO_2. To date, various polymorphs of TiO2 have been documented, including rutile, anatase,

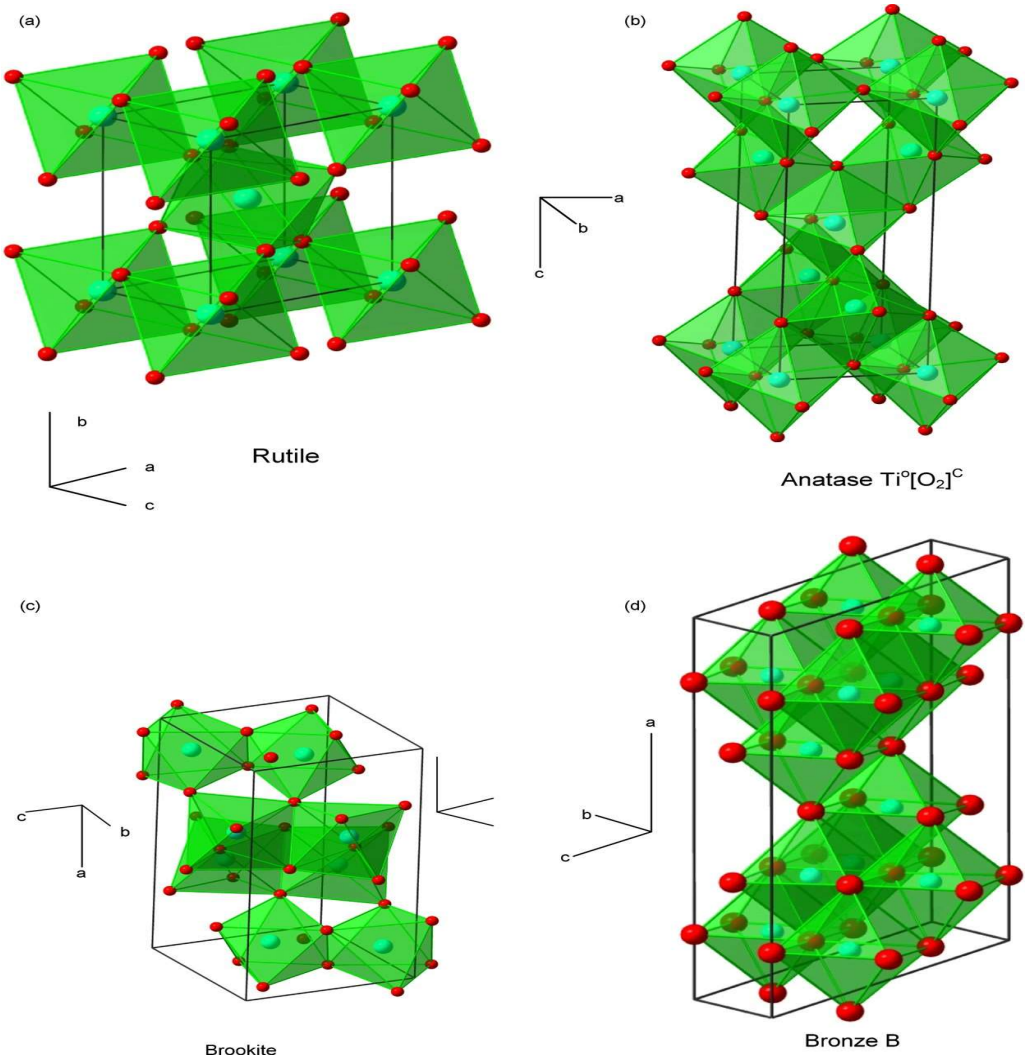

Figure 2. 2 (a) Rutile, (b) anatase, (c) brookite, and (d) bronze(B) of TiO_2 (Adapted from [48]).

brookite, TiO_2-B (bronze), TiO_2-R (ramsdellite), TiO_2-H (hollandite), TiO_2-II (columbite), and TiO_2-III (baddeleyite). Table 2 presents a comprehensive overview of the distinctive polymorph structures, providing relevant details. Within the various polymorphs of TiO_2, namely rutile, anatase, brookite, and TiO_2-B as depicted in Figure 2.2.

Table 2. 1 Crystal properties of different TiO_2 polymorphs [48]

Structure	Space group	Density(gcm^{-3})	Lattice Parameter
Anatase	Tetragonal $I4_1/amd$	3.79	a=3.79 c=9.51
Rutile	Tetragonal $P4_2/mnm$	4.13	a=4.59 c=2.96
Brookite	Orthorhombic *Pbcv*	3.99	a=9.17 b=5.46 c=5.14
TiO_2-B (Bronze)	Monoclinic *C2/m*	3.64	a = 12.17 b=3.74 c=6.51 β =107.298º
TiO_2-II (Columbite)	Orthorhombic *Pbcn*	4.33	a = 4.52 b = 5.5 c = 4.94
TiO_2-H (Hollandite)	Tetragonal*14/m*	3.46	a = 10.18 c = 2.97
TiO_2-III (Baddelyite)	Monoclinic $P2_1/c$		a=4.64 b=4.76 c=4.81 β = 99.28º

TiO_2-R (Ramsdellite)	Orthorhombic *Pbnm*	3.87	a = 4.9 b=9.46 c=2.96

2.2.1 Rutile:

Rutile, which is considered the most thermally stable polymorph of titanium dioxide (TiO_2), demonstrates a restricted ability to incorporate lithium ions, with a capacity of fewer than 0.1 lithium ions per unit of TiO_2 at room temperature [266, 272]. Li-reactivity was higher at a temperature of 120°C when using a polymeric electrolyte instead of a liquid electrolyte. In these conditions, the first discharge reversible capacities were reported to be 0.5 Li [273] and 1 Li [274] per formula unit of TiO_2. There is a consensus among scholars that the diffusion of Li in rutile exhibits a significant degree of anisotropy, characterized by rapid diffusion primarily along the channels aligned with the c-axis[275-279]. Previous research has provided empirical evidence and computational models to support the assertion that the diffusion coefficient of Li^+ in the direction of the c-axis is estimated to be around 10^{-6} cm^2s^{-1}, whereas in the ab-plane, it exhibits a significantly lower value.

The diffusion coefficient was reported to be approximately $10^{-15}cm^2s^{-1}$ in previous studies [276, 277, 280]. As a result, the velocity of ion transportation in the ab-planes experiences a notable reduction, which hinders the easy migration of lithium ions to the thermally preferred octahedral sites and imposes constraints on the inclusion of lithium inside the c-channels. As a result, the velocity of ion transportation in the ab-planes experiences a notable reduction, which hinders the easy migration of lithium ions to the thermally preferred octahedral sites and imposes constraints on the inclusion of lithium inside the c-channels [276, 277].

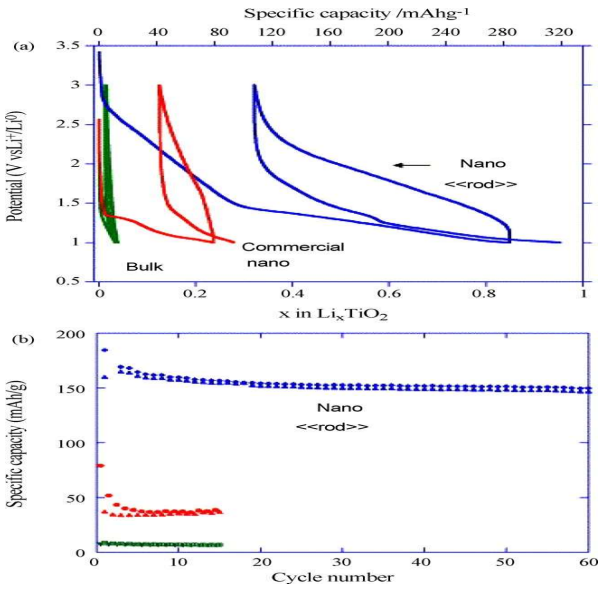

Figure 2. 3 Galvanostatic cycling curves of rutile TiO_2 samples using a 30mA g^{-1} current between 3 and 1V in 1 M $LiPF_6$ EC/DMC electrolyte at 20°C. The capacity retention is reported for these different samples (Adapted from [281]).

It is noted that the reactivity of Li exhibits an upward trend as the particle size decreases. Hu et al. [282] observed a maximum lithium insertion of 0.8mol into nanostructured rutile TiO_2 (10 nm x 40 nm) at ambient temperature in their study. In contrast, 0.1-0.25mol of lithium was inserted to micrometer-sized rutile. A specific charge of approximately 160milliampere-hours per gram ($mAhg^{-1}$) was achieved at a rate of one-twentieth of the capacity (C/20) after undergoing 50 charge-discharge cycles. This specific charge decreased to 150mAh g^{-1} when the rate was increased to one-fifth of the capacity (C/5), and further decreased to 100 mAh g^{-1} when the rate was increased to ten times the capacity (10C). The researchers discovered that the storage of Li on the surface of nano-sized particles is more energetically advantageous than bulk insertion. The investigation of particle size effects was additionally conducted by Baudrin et al. [281], as illustrated in Figure 2.3. The research findings indicated that nano-sized TiO_2 particles with a diameter of 50 nm can accommodate till 0.23 lithium ions per TiO_2 rutile unit. This specific capacity of 77milliampere-hours per gram ($mAhg^{-1}$) at a

rate of 1/10C during the initial reduction process until reaching a voltage of 1.0 V. Following this, it is possible to extract roughly 0.11 lithium ions during the next oxidation process. When the particle size was decreased to 10nm, the reaction between Li and the nanostructured matter the rutile rods particles (10 nm × 200 nm) led to a Li intake of as much as 0.85 during the initial decrease, while keeping the experimental conditions constant. The Li-reaction occurred through the traversal of two solid solution domains, subsequently leading to an irreversible phase transition into electrically charged rock salt type $LiTiO_2$ (ccp) as a result of an increase in volume in the ab-plane. The nanostructured $LiTiO_2$ material was subjected to additional oxidation and cycling processes, which led to the achievement of a reversible ability of 0.5 Li peroxide. The capacity of this material is similar to that of the whole anatase type of TiO_2, which is well recognized as a more electrically active host for lithium insertion (to be elaborated on in following sections). The nano-rutile material exhibited volt composition curves that displayed a smooth and uninterrupted pattern, reminiscent of the Li-insertion/extraction mechanism observed in layered V_2O_5. [283]. In general, it was noted that the principal kinetic constraints were connected with physical strains, which were alleviated with decreased particle size. As a result, this decrease in size enabled a more efficient process of lithium insertion. It was hypothesised that the effect of size on the phenomenon would be more pronounced for nano-rods oriented along the c-axis. This phenomenon can be attributed to the fact that the primary expansion predominantly takes place along the small dimension within the ab-planes. In a study conducted by Anji Reddy et al. [284], it was demonstrated that Li-insertion can occur at room temperature in nanocrystalline rutile TiO_2 synthesized using the sol-gel method. The researchers shows the insertion of 1 Li per formula unit. In a recent study by Jiang et al. [285], it was observed that the Li-insertion capacity of TiO_2 rutile nano-electrodes could reach up to 1.0 Li at the initial

discharge cycle performed at a rate of $0.05Ag^{-1}$ (equivalent to approximately 1/6C). Furthermore, it was found that reversible cycling of 0.6-0.7 Li can be achieved. Following 100 cycles, the ultra-fine nano-rutile electrodes exhibited a discharge capacity of 132 and 118 $mAhg^{-1}$ when subjected to cycling at 5 and $10Ag^{-1}$ (approximately equivalent to 16 and 32C), respectively.

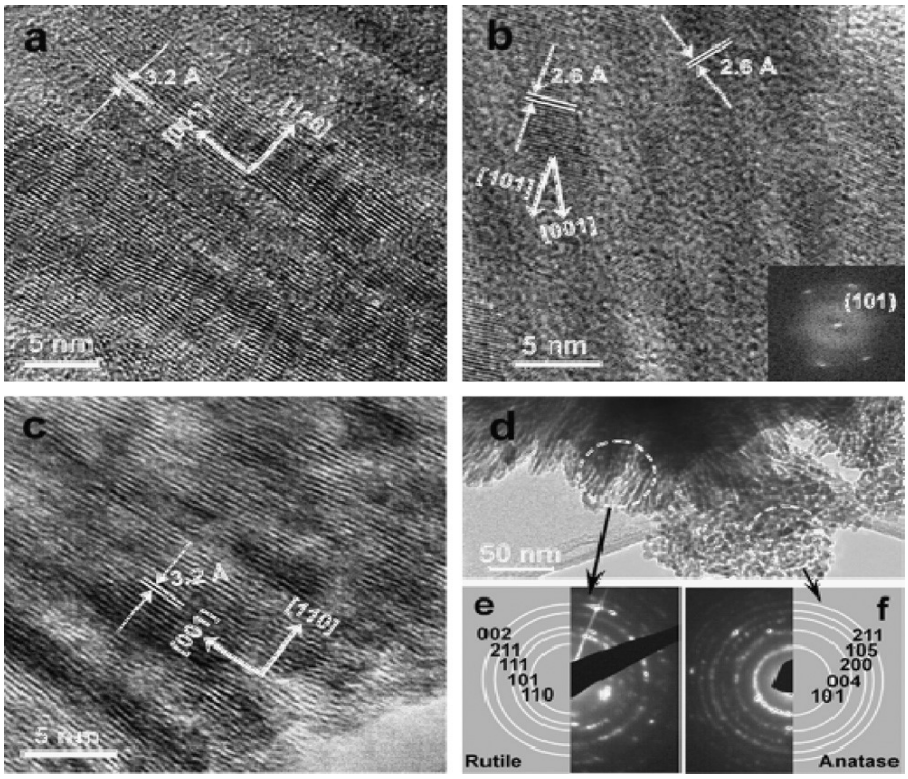

Figure 2. 4 (a, b) High-resolution TEM images of as-synthesized mesoporous crystalline TiO_2. Inset in (b) shows corresponding SAED pattern. (c) High-resolution TEM image of calcined mesoporous crystalline TiO_2. (d) TEM image of aggregated spherical anatase particles outside of nano-rod-based mesoporous rutile in mesoporous crystalline TiO_2. (e) SAED pattern from the oriented rodlike nanocrystal area circled in (d). The diffraction ring pattern is consistent with that of rutile crystal structure. (f) SAED pattern from spherical nano-particle area circled in (d). The diffraction ring pattern is consistent with that of the anatase crystal structure (Adapted from [286]).

Furthermore, the investigation by Liu et al. [286] focused on examining Li-insert capabilities in rutile TiO_2, which also contained a small quantity of the anatase. The present sample was produced through an innovative solution

growth technique at low temperatures, wherein TiO_2 nanocrystals were formed within a matrix of anionic surfactants. The mesoporous TiO_2 material discussed in Figure 2.4 exhibits a high degree of crystallinity and possesses a large surface area ranging from 245 to $300 m^2 g^{-1}$. This material is characterized by aligned rutile nano-rods that have grown along the [0 0 1] direction. The Li-insertion properties of the mesoporous rutile material are depicted in Figure 2.5. At a rate of C/5, the initial discharge between 1 and 3V vs. Li^+/Li, it was observed that the material $Li_{0.7}TiO^2$ could accommodate more than 0.7 Li with a capacity of $235 mAhg^{-1}$. This reversible capacity was 0.55 Li (185mAhg−1) for $Li_{0.55}TiO_2$. The mesoporous crystalline rutile exhibits remarkable capacity retention, demonstrating a capacity loss of less than 10% even after undergoing over 100 cycles. The research findings revealed that the rutile nano-rods experienced an irreversible transition, leading to the creation of cube rocksalt $LiTiO_2$ nano-rods during the initial discharge process. Nevertheless, the stability of the meso-structure of $LiTiO_2$ remained consistent after repeated discharge/charge cycling.

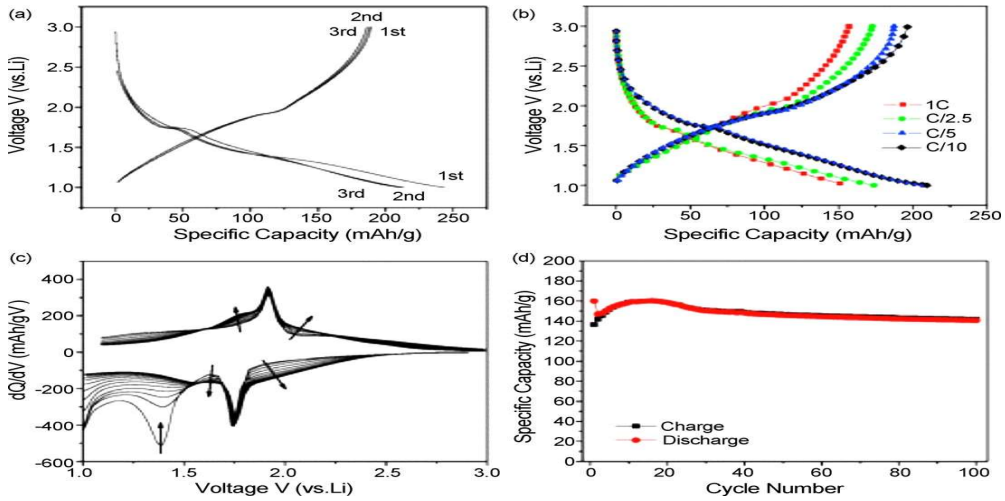

Figure 2. 5 (a) First three potential-capacity profiles of mesoporous crystalline TiO_2 at a rate of C/5 between voltage limits of 1 and 3V vs. Li+/Li. (b) Fifth cycle discharge–charge capacity profile of the mesoporous crystalline TiO_2 at the various rate (1C–C/10) between voltage limits of 1 and 3V. (c) dQ/dV vs. potential plot of lithiated/delithiated mesoporous crystalline TiO_2. (d) Cycling behavior of mesoporous crystalline TiO_2 up to 100 cycles at a 1C rate (Adapted from [286]).

2.2.2 *Anatase:*

When comparing the rutile structure to the anatase lattice, it can be observed that the incorporation of Li+ ions is more easily achieved in the latter. The material exhibits a tetragonal body-centered space group with the notation I41/amd. The structure consists of octahedral TiO_6 units which share two edges that are adjacent with additional octahedra, resulting in the formation of planar double chains [59]. The diffusion of Li-ion within an anatase framework takes place along a chemical pathway that establishes a connection between the octahedral interstitial sites [287-289]. The introduction of Li into the anatase unit cell leads to a reduction in symmetry. Specifically, when the Li content is at x = 0.5 ($Li_{0.5}TiO_2$), the unit cell's original I41/amd symmetry is transformed into the orthorhombic Pmn21 space group. This transformation occurs due to the loss of symmetry along the y direction [290].

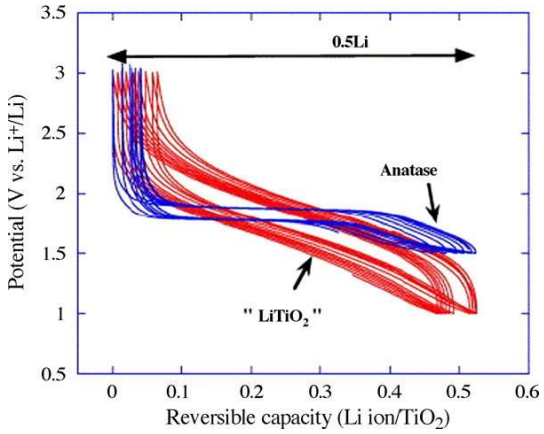

Figure 2. 6 Comparison between the electrochemical behavior of rutile (nano-rod) and anatase type TiO_2 after the first reduction in a galvanostatic mode with 30 mAg^{-1} between 3 and 1V in 1 M $LiPF_6$. EC/DMC electrolyte at 20°C (Adapted from [291]).

The change in symmetry is accompanied by a decrease in the size of the single cell along the c-axis and an increase along the b-axis, resulting in an overall increase of 4% in the total area of the unit cell. This change is also associated with a swift deterioration in capacity [292]. Therefore, it has been consistently reported in the literature that the maximum electrochemical insertion of Li in bulk anatase occurs when x = 0.5 [291, 293-295]. Additional research conducted by Wagemaker et al. [296-299] revealed that, in the process of Li-insertion, the anatase material exhibited an inherent tendency to undergo phase separation, resulting in the formation of distinct $Li_{0.01}TiO_2$ and $Li_{0.6}TiO_2$ domains at a nanoscale level. The voltage curves of bulk anatase, as depicted in Figure 2.6, exhibit a flat profile, suggesting a conventional bi-phase electrochemical reaction mechanism involving the insertion and extraction of Li-ions. The electrochemical processes and reactivity towards lithium are influenced by a decrease in the size of particles to the nanoscale region, particularly below 100nm, in a manner akin to the rutile structure. The manner in which Li interacts with nanostructures deviates of the two-phase equilibrium typically seen in bulk materials, rather exhibiting similarities to

the behaviour exhibited by solid solutions [300]. The reduction in dimensions and unique morphological characteristics led to an increased capacity that surpassed 0.5 Li/unit of equation. This can be attributed to the charge storage

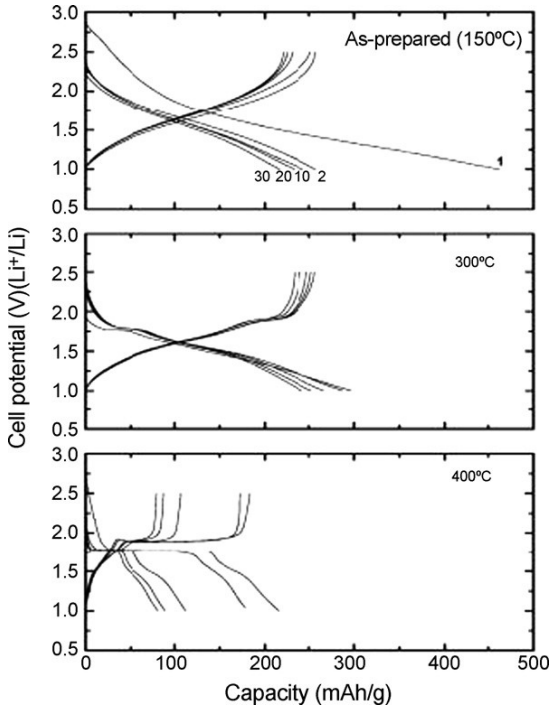

Figure 2. 7 Nano-anatase TiO_2 voltage profiles of the as-prepared (150°C), annealed nanotubes (300°C), and nano-rods (400°C) between 2.5 and 1V at a rate of 0.1C(=25 mAg^{-1}) after 1st, 2nd, 10th, 20th, and 30th cycles using coin-type half-cells (electrode density was $2gcm^{-3}$) (Adapted from [301]).

occurring primarily on the surface and using different lithium reaction mechanisms compared to those observed in bulk materials [302, 303]. In their study, Gao et al. [304]documented the initial discharge and charge capacities of 340 and $200mAhg^{-1}$, respectively, for anatase nanotubes. These nanotubes were synthesized through annealing hydrothermally prepared protonated nanotubes at 500°C in an argon atmosphere. The dimensions of the nanotubes were measured to be 10–15 nm in outer diameter and 200–400nm in length. In their study, Li et al. [291] fabricated anatase TiO_2 nanotubes with outer diameters measuring 9 nm and lengths spanning several hundred nanometers. The aforementioned outcome was attained through the process

of annealing at an average temperature of 350°C, employing hydrothermal-treated protons titanate nanotubes. The anatase nanotubes exhibited an initial discharge capacity of 314mAhg^{-1} and an initial charge capacity of 248mAhg^{-1}, despite having a comparatively low active substance loading of only 3–4mgcm^{-2}. Zhang et al. [305] employed a hydrothermal method to synthesize anatase nanotubes with dimensions of approximately 10nm in diameter and lengths ranging from 200 to 400 nm. During the process of Li-insertion and extraction, the TiO_2 polymorph exhibited a potential peak at 1.73 and 1.88V in one dimension. The initial capacity for Li-insertion/extraction was recorded as 290 and 238 milliampere-hours per gram (mAhg^{-1}) at a current density of 36 milliamperes per gram (mAg^{-1}) respectively. In their study, Kim and Cho [301] documented the synthesis of anatase TiO_2 nanotubes and nano-rods through annealing a mixture of $H_2Ti_2O_5 \bullet H_2O$ and anatase TiO_2 nanotubes. The annealing temperatures employed were 300 and 400°C, respectively. The two nanostructures demonstrated initial discharge capacities of 296mAhg^{-1} ($Li_{0.88}TiO_2$) and 215mAhg^{-1} ($Li_{0.64}TiO_2$), as depicted in Figure 2.7. This was achieved under galvanostatic conditions with a current density of 25mAg^{-1} (approximately 1/10C) in an electrolyte consisting of 1M $LiPF_6$ dissolved in a mixture of ethylene carbonate (EC) and dimethyl carbonate (DMC). The voltage range for the discharge was set between 2.5 and 1V. The irreversible capacity ratios for anatase nanotubes and nano-rods were documented as 14% and 15%, respectively. The nanotubes exhibited a capacity retention of 81%, whereas the nano-rods only demonstrated a capacity retention of 40% after undergoing 30 cycles. The study revealed that the electrode density significantly impacted the high performance of nano-rods. The nano-rods, having a density of 0.5gcm^{-3} (equivalent to 12mgcm^{-2}), exhibited discharge capacities of 200 and 160mAhg^{-1} when subjected to discharge rates of 0.5 and 10C, respectively. In contrast, the nanotubes exhibited no decrease in capacity at discharge rates of 0.5C or 10C when subjected to electrode densities of

either 1.0 or 0.5gcm^{-3}. At a density of less than 2gcm^{-3} (equivalent to 31mgcm^{-2}), the nanotubes exhibited a capacity of 245mAhg^{-1} at a 0.5C rate and 185mAhg^{-1} at a 2C rate. In a recent study, Bao et al. [306] presented their findings on synthesizing nanoporous anatase nano-rods. During the process of Li-insertion and extraction, the TiO2 polymorph exhibited a potential peak at 1.73 and 1.88V in one dimension. The initial capacity for Li-insertion/extraction was recorded as 290 and 238 milliampere-hours per gram (mAhg^{-1}) at a current concentration of 36 milliamperes per gram (mAg^{-1}), respectively. Additionally, it displayed uniform and regular structures in rod shapes. The nano-porous structure exhibited favorable cycle-ability and a notable rate capability.

2.2.3 Bronze or TiO_2-B

The synthesis of TiO_2-B was initially achieved by Marchand et al. [307] in 1980 through an ion-exchange process, where K+ ions were substituted with H^+ ions in $K_2Ti_4O_9$, resulting in the formation of a hydrated hydrogen titanate. Subsequent heating at a temperature of 500°C led to the transforming of the hydrated hydrogen titanate into TiO_2-B. Like rutile and anatase, TiO_2-B comprises corrugated sheets consisting of TiO_6 octahedra that share edges and corners [308]. Nevertheless, in the case of TiO_2-B, the octahedra exhibit an arrangement that gives rise to routes that bear a resemblance to perovskite structures. These pathways enable easy transportation of inserted Li^+ ions. The structural arrangement of TiO_2 exhibits a higher degree of porosity than alternative polymorphs, as evidenced by its lower density of 3.73gcm^{-3}. In contrast, rutile and anatase possess densities of 4.25gcm^{-3} and 3.89gcm^{-3}, respectively. The presence of an open structure may potentially facilitate the transport of Li^+ ions.

The synthesis of TiO_2-B nanowires was conducted by Armstrong et al. [309-311] through a hydrothermal reaction involving sodium hydroxide (NaOH)

and TiO_2 anatase. The subsequent electrochemical assessment yielded a capacity of 305mAhg^{-1}, denoted as $Li_{0.91}TiO_2$-B, in contrast to the bulk TiO_2-B which exhibited a capacity of 240mAhg^{-1}. The incremental capacity plots, precisely the rate of change of capacity with respect to voltage (dQ/dE vs. E), did not demonstrate any significant structural modifications taking place during the process of lithium insertion and extraction. Although the capacity of TiO_2-B nanowires was found to be similar to that of nano-particulate TiO_2-B, the nanowires exhibited superior capacity retention. Following 50 iterations, the TiO_2-B nanowires exhibited a capacity approximately twice as high as the nano-particulate TiO_2-B.

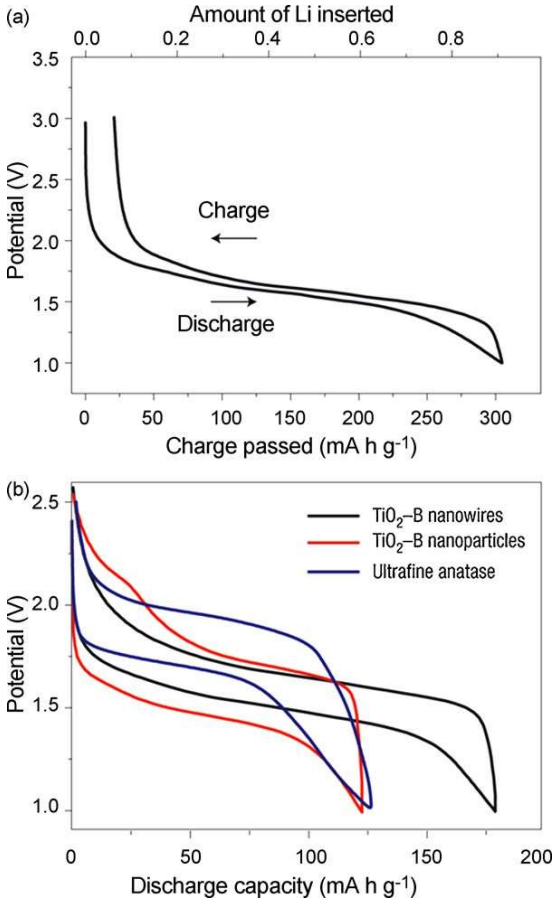

Figure 2. 8 (a) Charge–discharge curves for Li_xTiO_2-B nanowires (rate of 10 mAg^{-1}); (b) comparison of cycling behavior for TiO_2-B nanowires, TiO_2-B nano-particles and nano-particulate anatase, all at 200mAg^{-1} (Adapted from [309, 310]).

Furthermore, there have been reports indicating that the activity of TiO_2-B nanowires surpasses that of nano-particle anatase, while possessing an average particle size comparable to the size of the TiO_2-B nanowires. (refer to Figure 2.8). Like other types of polymorphs, whether they are in the form of nanostructures or bulk materials, an irreversible capacity loss was seen during the initial cycle. The tentative explanation for this phenomenon was the insufficient conductivity of TiO_2. In recent times, there have been notable advancements in the understanding of the interaction between lithium (Li) and nanostructured titanium dioxide (TiO_2(B)). The investigation and analysis of pseudocapacitive lithium storage in TiO_2(B) was reported as well as discussed by Graetzel and colleagues [303]. The electrochemical process of Li-insertion in TiO_2(B) exhibits distinguishable characteristics compared to that observed in anatase. The chemical processes of lithium storage are primarily controlled by solid-state diffusion of Li^+. However, the TiO_2(B) host enables the adaptation of lithium via a pseudocapacitive faradic mechanism. This process is not governed by diffusion control under identical conditions.

In order to conduct a more comprehensive analysis of the electrochemical capabilities of TiO_2-B nanowires, Armstrong et al. [312] fabricated lithium-ion batteries with the nanowires serving as the anode, a gel electrolyte, and either a $LiFePO_4$ or $LiNi_{0.5}Mn_{1.5}O_4$ cathode. The average cell voltages were approximately 2V and 3V, respectively. The cycling stability demonstrated an outstanding level of efficiency, as did the rate capability, achieving a remarkable 80% preservation of the low-rate capacity recorded at 5C. The batteries employing the TiO_2-B anode cells had a higher capacity in comparison to batteries with similar design that utilized $Li_4Ti_5O_{12}$ (225$mAhg^{-1}$ as opposed to 150$mAhg^{-1}$ at C/5) [313].

2.2.4 Brookite

Recently, there has been a study conducted to evaluate the Li-electrochemical reaction of brookite, rutile, anatase, and bronze structures. The synthesis of brookite was reported by Anji Reddy et al. [314, 315], who conducted thermolysis of $TiCl_4$ at a temperature of 100°C. The acquired rutile and brookite mixture underwent separation through peptization in a solution of 3M nitric acid, followed by centrifugation. The brookite material, with a nano-scale size of 10nm, was subjected to testing as a lithium-ion anode. The testing results revealed a reversible capacity of 170mAhg^{-1}, which was sustained for over 40 cycles. The specific capacity of brookite exhibited variations based on particle size. For instance, brookite particles measuring 20nm and 33nm demonstrated specific capacities of 60mAhg^{-1} and 35mAhg^{-1}, respectively, after undergoing 50 cycles. In a study by Lee et al. [316] brookite was synthesized through urea precipitation. The researchers examined brookite particles ranging from 10 to 20nm combined with multi-walled carbon nanotubes. This composite material exhibited a capacity of 160mAhg^{-1} throughout 50 cycles. The Li-insertion/extraction process was seen at voltage levels of 1.7 V and 2.02 V, respectively. In comparison, anatase exhibited Li-insertion/extraction at voltage values of 1.64 and 2.1V (refer to Figure 2.9).

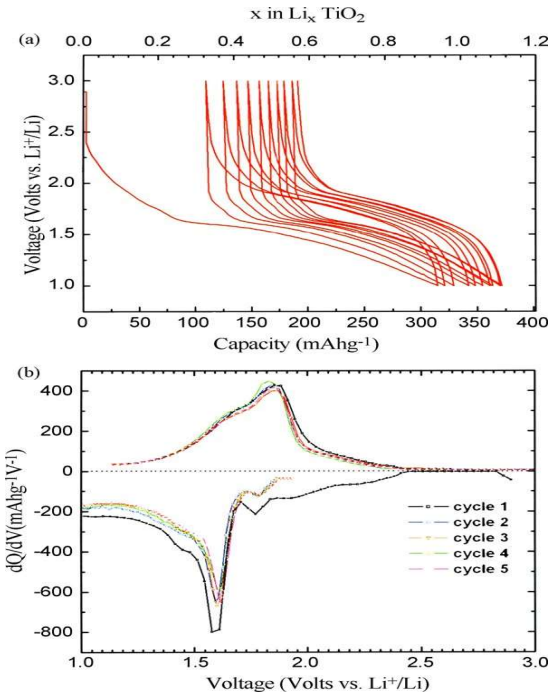

Figure 2. 9 (a) Voltage-capacity profiles of brookite TiO_2 for the first 10 cycles carried out in the voltage range 1.0–3.0V at C/10 rate; (b) the corresponding differential capacity plot for the first 5 cycles (Adapted from [316]).

2.3 Influence of Experimental Conditions:

The amount and type of crystallinity is greatly influenced by numerous associated factors, such as pH, temperature of annealing, and preparation processes. Numerous methodologies have been employed in the fabrication of TiO_2 crystal structures. The impact of pH on the optimization of the crystal lattice is of utmost importance. A study conducted by Ibrahim et al. [317] demonstrated that a decrease in acidity levels promotes higher crystallinity. Specifically, the formation of anatase was observed at a pH of 9. Using a straightforward sol-gel technique produced TiO_2 nanocrystalline powders with particle sizes ranging from 3 to 7 nm, achieved by adjusting the pH to 1. The solution saw a rise in pH from 2 to 7, leading to the formation of a composite of anatase and rutile phase. The process of further incrementation has resulted in transforming the substance into brookite [318]. In their study, Molea et al. [319] employed the hydrolysis method to generate nanocrystal

powder of TiO_2, exhibiting diverse crystal structures. A mixed phase of anatase (approximately 30%) and rutile (approximately 70%) was obtained at a pH of 3. However, as the pH value increased, a phase transformation was observed. The presence of pure anatase crystal phase with varying lattice parameters was observed at pH levels of 8.5 and 10. In their study, Yang et al. (2017) conducted the synthesis of TiO_2 nanorods using a hydrothermal technique. Their findings supported the hypothesis that there is a relationship between pH and crystal structure. Specifically, they observed that the presence of the brookite phase was only evident at pH values below 8, while pH values ranging from 8 to 10 indicated the presence of a mixed rutile-brookite phase. The presence of the pure anatase phase was observed concurrently when the pH exceeded 10. Once again, it is worth noting that crystallography exhibits a notable correlation with the annealing temperature. Barki et al. (year) demonstrated, as depicted in Figure 2.1, that the initiation of anatase phase occurred at a temperature of 300°C, while the transition from anatase to rutile phase was observed at 900°C. The transformation from anatase to rutile phase takes place at a temperature of 600°C [320]. The X-ray diffraction (XRD) analysis revealed the transformation of amorphous TiO_2 nanotubes into a fully developed anatase phase upon calcination at a temperature of 500°C. The calcination process, when extended to a temperature of 850°C, resulted in a significant increase in the intensity of

rutile peaks, as depicted in Figure 2.10 [321]. Simultaneously, there was a corresponding decrease in the intensity of anatase nanotubes.

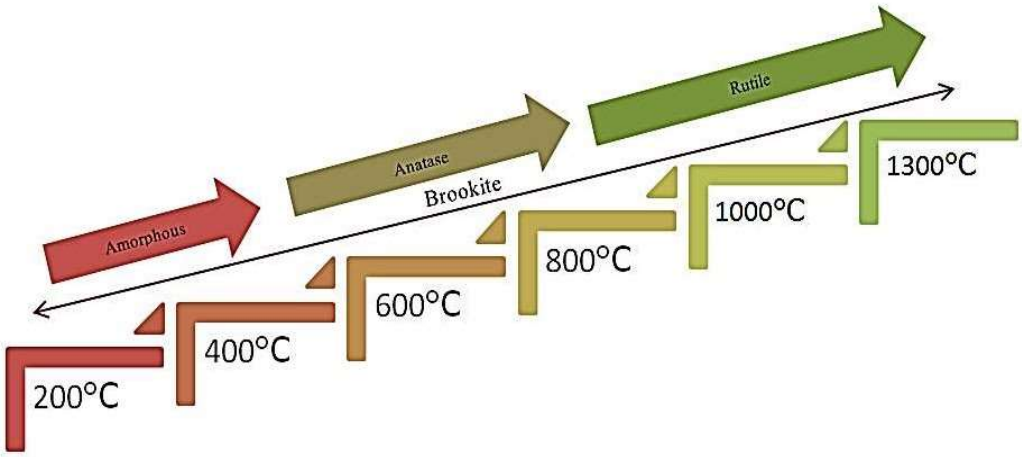

Figure 2. 10 TiO_2 crystal phase dependency on annealing temperatures (Adapted from [321]).

2.4 Different Nano-Structures

Various morphologies of TiO_2 exhibit distinct properties due to their different nanostructures. Granular titanium dioxide (TiO_2) exhibits greater advancement and distinct characteristics than other forms. The increased surface area of the band gap in boarded TiO_2, as compared to bulk TiO_2, promotes improved electron transport and heightened interfacial contact between electrolyte and electrodes. Therefore, they are provided with enhanced electrochemical properties [322].

2.4.1 One-Dimensional Structure

In recent years, there has been considerable scholarly attention directed towards the study of one-dimensional nanostructured titanium dioxide (TiO_2). This research has explored a range of morphologies, including nanowires, nanorods, nanoneedles, nanobelts, and nanotubes. Extensive research has been conducted on nanoparticles due to their ability to possess all the properties of conventional particles while exhibiting distinctive

characteristics. The artificially created structures feature the inherent property of being comprised of a minimum of one dimension ranging from 1 nm to 100 nm, and also demonstrate a high aspect ratio [323]. The nanobelt is considered to be a highly desirable one-dimensional nano-structure composed of titanium dioxide (TiO_2). The higher crystallinity of TiO_2 nanobelts is associated with a relatively large specific surface area. Moreover, facilitate the transportation of electrons in the axial orientation. Moreover, the uncomplicated procedure of synthesis is considered to possess greater benefits [323, 324].

The researchers, J. Tian et al., conducted a study in which they recorded the identification of a distinctive heterostructure in the form of a belt formed of TiO2. The aforementioned architecture is attained by organizing secondary nanoparticles of varying morphologies, including nanowires, nanorods, nanoneedles, or nanotubes, onto the surface of one-dimensional nanostructures. Several methodologies have been utilized in the synthesis of metal nanoparticles and one-dimensional nanostructures, including the wet in-situ reduction method, photo reduction in-situ method, and immobilization method. The resultant products display a diameter that spans form 3 to 5 nm and exhibit a greater level of homogeneous distribution throughout the outermost layer of the nanobelt with one-dimensional characteristics. Furthermore, due to the absence of inorganic reagents in this procedure, it can be considered a more environmentally friendly and non-toxic process. Furthermore, numerous research studies have incorporated the immobilization technique, which involves assembling metal nanoparticles or 1D nanobelts on the surface, or both, to establish interconnections between them. The capacity to exercise exact manipulation over metal nanoparticles, together with their morphology, bestows notable benefits. Nevertheless, it is crucial to implement alterations to surfaces within this specific methodology

[325-327]. Furthermore, the effectiveness of this method cannot be sufficiently explained due to the diverse aggregation, since the nanoparticles are coupled with the nano-structured substrate by chemical bonding. Within the framework of in-situ methodologies, the lattices exhibit a physical attaching mechanism that establishes a connection with the substrate [328].

The utilization of 1D nanobelts as the negative anode in LiB's has garnered significant interest among research groups. Due to its comparatively expansive specific area, the electrode exhibits enhanced interfacial reactivity with the electrolyte, thereby facilitating a greater extent of Li+ intercalation. Furthermore, the notable degree of crystallinity exhibited by the material, coupled with its porous structure, serves to augment both electrons conductivity and diffusion. Additionally, the layered structure of the nanobelts offers improved durability as well as versatility in their architecture throughout the process of lithium ion insertion and extraction. However, the potential of regarding it as a system for storing energy is uncertain due to its inherently limited electronic conductivity. The aforementioned rationale can be ascribed to the substantial surface area, which leads to a diminished current density and subsequently enhances the rate of charge and discharge. Additionally, the substantial surface area facilitates the occurrence of side reactions with electrolytes, resulting in the thickening of the solid electrolyte interface. The presence of a thicker layer hinders the transport of electrons and Li^+ ions. In addition, it should be noted that the high rate of charge and discharge may not always be advantageous due to the phenomenon of nanoparticle aggregation, which leads to increased inter-particle resistance. In order to address this issue, a potential solution involves incorporating nanobelts with conductive materials, such as C/TiO_2 nanowires, C/TiO_2 nanotubes, functionalized graphene sheet/TiO2 nanorods, and Sn/TiO_2 nanotubes, as suggested by reference [329].

As previously stated, nanostructured TiO_2 exhibits superior electrochemical activity compared to bulk TiO_2 material. Numerous research studies have been published highlighting the superior electrochemical performance of the anatase crystal structure of TiO_2 compared to other polymorph structures. Specifically, the anatase structure exhibits enhanced Li^+ ion storage capacity, making it a promising candidate for use as an anode material in lithium-ion batteries (LIBs). The discharge process of anatase TiO_2 can be primarily categorized into three distinct steps. During the initial phase, a reduction in potential occurs as a result of the formation of conductive Li_xTiO_2 in the solid solution stage. Phase switching takes place during the second stage due to the simultaneous presence of two phases: Lipoor phase (tetragonal $Li_{0.001}TiO_2$) and Lirich phase (orthorhombic $Li_{0.5}TiO_2$) under equilibrium conditions. This phenomenon represents the reversible insertion and extraction of Li+ ions into and out of the octahedral site of anatase TiO_2. During the third step, the Li^+ ions are immobilized on the anode's surface through the formation of a Li_1TiO_2 phase, wherein the intercalation potential x is equal to 1. The cause of this problem can be attributed to the pseudo-capacitance characteristics of the anode material. The pseudo-capacitance phenomena, as observed, is influenced by the unique morphology and crystal arrangement of the anode material, which is formed of TiO_2. Enhancing the surface to volume ratio has the potential to augment the pseudo-capacitance characteristic, as well as promote greater interfacial interaction between the electrode and electrolyte, thereby facilitating a faster diffusion rate of Li^+ ions. As a result, the capacity for lithium storage is enhanced. Nevertheless, the efficiency of the method is impeded by numerous notable constraints, including a lack of thermodynamic stability and challenges associated with its handling. To tackle these concerns, one potential solution could involve the adoption of a micro hierarchal nano-structure. This approach has several benefits, including the utilization of micro hierarchal building blocks, the achievement of high

current density, and the establishment of thermodynamic stability. The mesoporous form of titanium dioxide (TiO_2), composed of nanocrystals, has attracted considerable interest owing to its distinctive amalgamation of nano/micro hierarchical architecture, substantial surface area, and notable pore volume. [330], [329].

Tian et al. proposed a straightforward approach for synthesizing one-dimensional mesoporous anatase TiO_2 (1DMA-TiO_2). The resulting product exhibits a stable hierarchical structure and retains the distinctive properties associated with one-dimensional nanoparticles. One-dimensional (1D) titanium dioxide (TiO_2) exhibits a highly efficient electron pathway and a reduced diffusion length for ions. The fabrication procedure included a two-step methodology, wherein a carbon nanotube (CNT) was employed as a template. The morphological examination of anatase nanoparticles, with dimensions ranging from 5 nm to 12 nm, reveals a Coulombic effectiveness of 96.3%. Furthermore, it should be noted that these nanoparticles demonstrate a prolonged lifespan, the ability to operate at high rates, and a substantial reversible capacity, as depicted in Figure 2.11(a-f).The exceptional performances observed can be attributed to the unique architectural characteristics of 1DMA TiO_2. This material possesses a hierarchical structure at the nano/micro scale, which enables efficient electron transport. Additionally, the facile fabrication process further enhances the electron pathway, contributing to the overall efficiency of the system. The enhanced surface area facilitates increased interfacial contact and improved thermodynamic stability as a result of agglomeration and strain during cycling. However, future studies have the potential to expand upon this topic by modifying certain synthesis parameters, such as the template and parent materials. The aforementioned alterations have the potential to result in additional improvements in surface area, as evidenced in conventional

anatase mesoporous TiO_2, which possesses a specific surface area of around 505 m^2g^{-1}. The investigation of the electrochemical characteristics of 1DMA TiO_2 holds potential for enhancing the comprehension in this field [331].

In their study, Tang et al. (year) presented a novel hybrid structure, denoted as Gr-TNT, which consists of TiO_2 nanotubes integrated onto graphene sheets. This hybrid structure was developed through a combined approach that involved the incorporation of TiO_2 nanotubes onto graphene. The purpose of this approach was to enhance the electrochemical properties of the material. This hybrid structure is visually depicted in Figure 2.12 (a-d). Numerous research endeavors have been dedicated to the development of composites featuring nano-structures of TiO_2, owing to the exceptional electroconductivity of graphene. This characteristic facilitates a notable diffusion rate of charges and an increased capacity for Li^+ ion storage on the

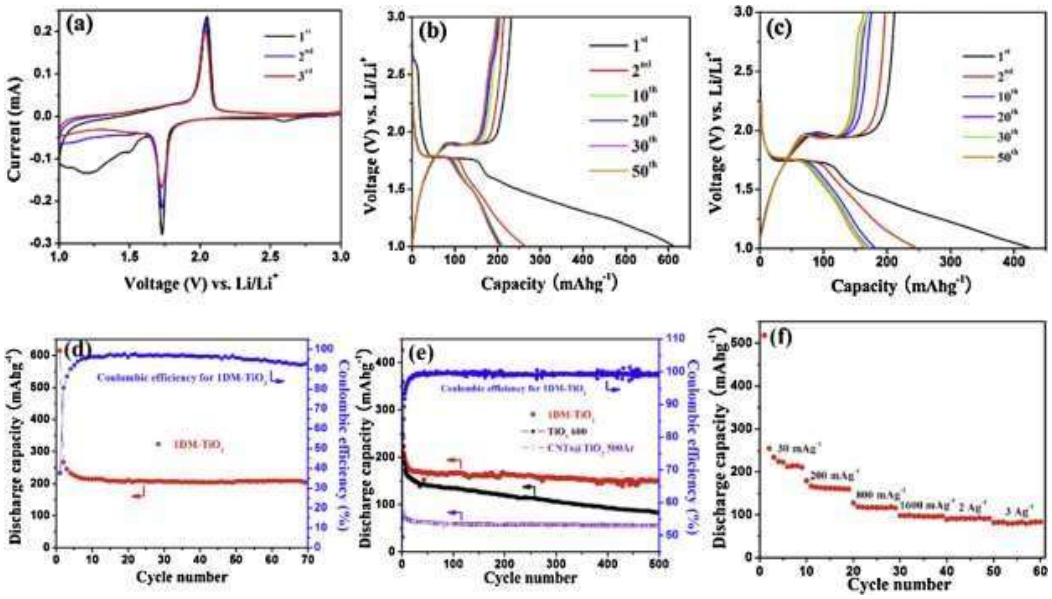

Figure 2. 11 (a) CV diagram (b,c) Charge/discharge profiles at 30mAg^{-1} and 200mAg^{-1} within 1V and 3V ; (d) Cycling performance and Columbic efficiency of 1DMA-TiO2 at 30mAg-1 between 1.0V and 3.0V. (e) Comparative cycling performance between different samples and Columbic efficiency at 200mAg^{-1} between 1.0V and 3.0V; (f) Rate capabilities of 1DM-TiO_2.(reprinted) [331].

surface of the composite structure. A gentle hydrothermal method is

employed to synthesize titanium dioxide nanotubes on graphene nanosheets. Titanium dioxide (TiO_2) colloids are employed as nucleation seeds on graphene oxide (GO) sheets, which serve as the central plane for the initiation of nanotubes. Graphene-Titanium Nitride (Gr-TNT) has demonstrated superior performance as an anode material for Lithium-ion Batteries (LIBs) compared to other nano-structures such as Gr-TiO_2 and bare TiO_2. Gr-TNT exhibits enhanced rate capabilities, improved cycle stability, and higher Li^+ storage capacity. Notably, Gr-TNT outperforms bare TiO_2, which only achieves a Li^+ storage capacity of 80 $mAhg^{-1}$ at a rate of 10C. The enhanced electrochemical properties observed in the high conductive graphene sheet/TiO_2 nano-structure can be attributed to several factors. Firstly, the graphene sheet improves electron conductivity, facilitating efficient charge transfer during electrochemical processes. Additionally, the nano-structure accommodates the strain resulting from intercalation and deintercalation processes, ensuring structural stability and prolonged cycling performance. Moreover, the increased surface area of the nano-structure enables a larger interface between the electrodes and the electrolyte, promoting enhanced electrochemical reactions. Lastly, the hierarchal architecture of the nano-structure contributes to these improvements. It is worth noting that while significant advancements have been reported for various other TiO_2 nano-structures, the combined effects of the aforementioned factors in the high conductive graphene sheet/TiO_2 nano-structure result in notable enhancements in electrochemical behavior [332].

In their study, Tammawat et al. (year) presented a novel 1D nano-structure of titanium dioxide (TiO_2) referred to as nanofibers, as depicted in Figure 2.12 (e-h). The nano-structure in question has attracted considerable attention due to its potential utilization as a material for anodes in lithium-ion batteries (LIBs) without necessitating the use of binders or conductive substances. The electrospinning technology was developed to fabricate nanofibers, which

were later subjected to the calcination at temperature of 400°C, 600°C, 800°C, and 1000°C for a duration of three hours. The study reported an average diameter of 200 nm for the as-prepared nanofibers, while for the calcined fibers at temperatures ranging from 400^0C to 800^0C, the average diameters were found to be between 100 nm and 120 nm. The presence of contamination in carbon-based amorphous polymer is the cause of this phenomenon. Following the process of calcination, the substance underwent a reduction in weight percentage at various calcination temperatures. The recorded weight percentages were 0.35%, 0.09%, 0.14%, and 0.74% for temperatures ranging from 400^0C to 1000^0C. Additionally, it was observed that the calcined products at a temperature of 1000^0C exhibited a characteristic morphology, consisting of interconnected particles with an average size of 100 nm. Enhanced electrochemical performances were observed in the case of anatase, as it is widely recognized that electrochemical performances tend to improve with decreasing crystallite sizes. The Columbic efficiency was observed to range from a minimum of 96% to a maximum of 100%. The positive outcomes observed in the 400^0C calcined material can be attributed to several factors. Firstly, the high surface to volume ratio of the material plays a significant role. This ratio allows for increased contact between the active material and the surrounding environment, facilitating more efficient reactions and interactions. Additionally, the higher nonstoichiometric parameters, specifically the presence of both Li^+ rich and Li^+ poor regions, contribute to the positive outcomes. This variation in lithium ion concentration within the material can enhance its electrochemical performance, leading to improved overall functionality.

Furthermore, the 100% active material composition ensures high electron conductivity. This characteristic is crucial for efficient charge transfer within the material, enabling better electrochemical reactions and ultimately

enhancing the material's performance. In brief, the favorable results seen in the calcined material at 4000C can be ascribed to its elevated area to volume ratio, the coexistence of regions with high and low Li+ concentrations, and the enhanced electron conductivity facilitated by the composition consisting entirely of active material [333].

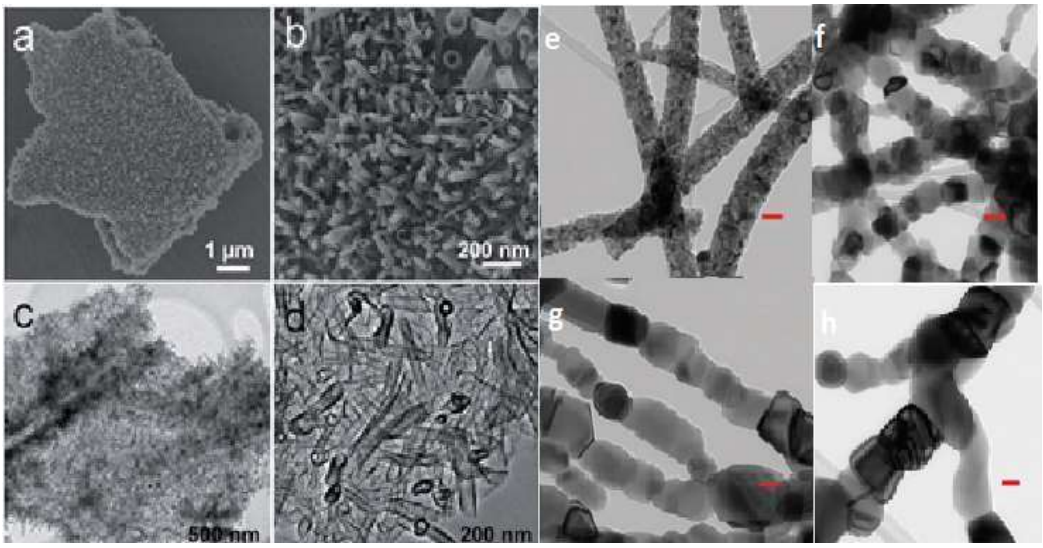

Figure 2. 12 (a and b) Scanning electron microscope (SEM) images of Gr–TNTs; inset in (b) high-magnification image showing TiO_2 nanotubes on the grapheme sheets; (c and d) transmission electron microscope images of the Gr–TNTs. (reprinted) [332] TEM images + of carbon-coated TiO_2 nanofibers (e-h) calcined in air for 3 h at 400^0C, 600^0C, 800^0C, and $1{,}000^0$C, respectively (reprinted) [333].

The authors, A. R. Armstrong et al., employed a straightforward preparation technique to fabricate nanowires using TiO_2-B polymorphs. The as-prepared nanowires exhibit a stable architecture, resulting in excellent capacity retention for a range of 2 to 100 cycles, as shown in Figure 2.13 (a). The capacity fading gradient at a rate of 50 mAg^{-1} (C/4 rate) was found to be 0.1%, and even more notably, it was only 0.06% for cycles 20 to 100. The high-rate capabilities, as depicted in Figure 2.13 (b), were observed to be 160 $mAhg^{-1}$ at a current density of 500 mAg^{-1} and 100 $mAhg^{-1}$ at a current density of 2000 mAg^{-1}. Moreover, the observed potential was approximately 1.6 V compared to Li^+ (1M) / Li, indicating that it offers a higher level of safety in comparison

to various other anodes such as alloys. The TiO_2-B nanowires possess several advantageous characteristics that position them as a highly promising contender for lithium-ion batteries (LIBs). However, it is crucial to prioritize the dissemination of comprehensive information regarding the precise source of irreversibility in order to further enhance their potential. The application of a conductive coating onto materials presents a potential solution that has the capacity to significantly enhance electronic conductivity [310].

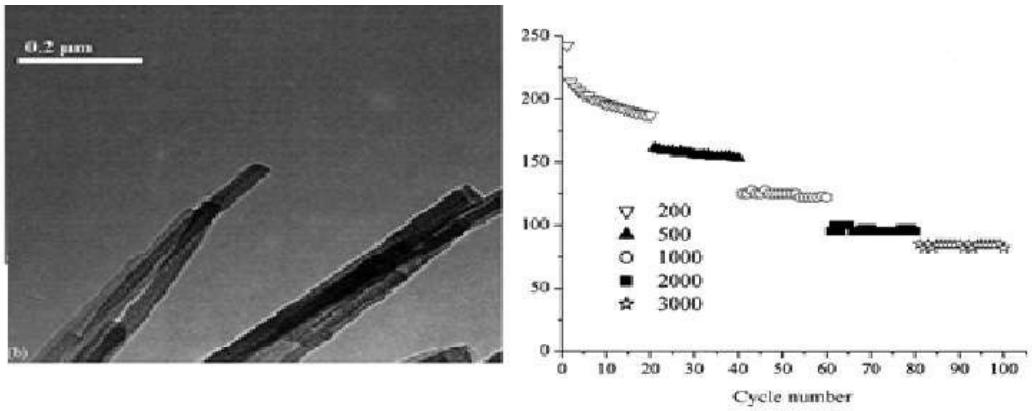

Figure 2. 13 (a) TiO_2-B nanowire TEM image, (b) discharge capacities corresponding to cycle number at different current densities (reprinted) [310].

H. R. Xia et al. carried out the fabrication of TiO_2 nanorod films by a hydrothermal technique at the liquid-gas interface. These films were subsequently utilized as anode materials in lithium-ion batteries without the addition of any additives. This material exhibits exceptional qualities as an anode in lithium-ion batteries (LIBs). Firstly, it can be utilized as an anode without the need for conductive agents or binders. The initial discharge capacity of the sample was observed to be 31.44 $mAhg^{-1}$ when subjected to a current density of 30 mAg^{-1}. After undergoing 100 cycles of cycling, the observed capacity was measured to be 32.66 $mAhg^{-1}$, which surpasses the initial capacity as depicted in Figure 2.14 (a, b). The matter described above can be effectively resolved by taking into account the chemical durability and improved electron channel provided by the provided structure. Nevertheless, the specific capacity demonstrated by this specific TiO2 structure was rather

inferior in comparison to other structures. Hence, it is deemed unsuitable for utilisation as an anode in lithium-ion batteries. The production of hetero-nanostructures and their subsequent application of a conductive coating, such as carbon, holds promise for substantial enhancements in specific capacity, charging and discharging rate, rate capacity, and cycles stability [334].

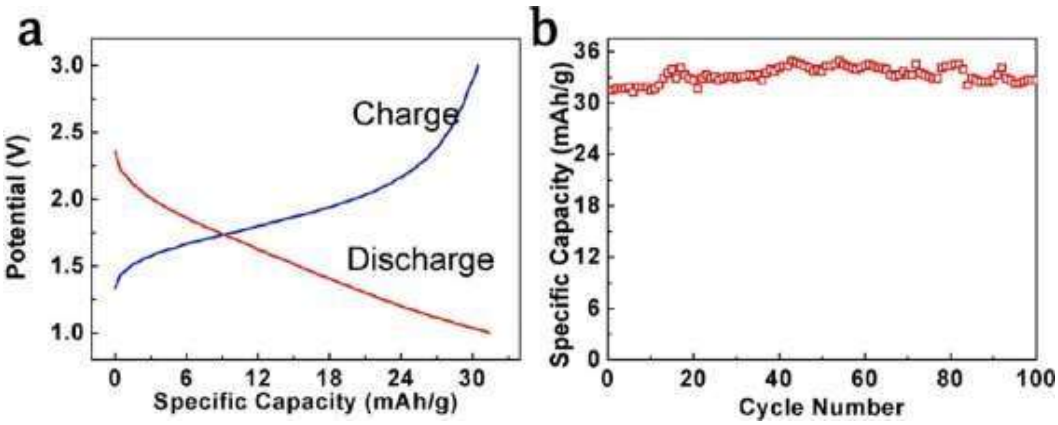

Figure 2. 14 (a) Initial charge-discharge profile (b) The corresponding cycle performance of TiO_2 nanorods as anode of LiBs (reprinted) [334].

2.4.2 Two-Dimensional Structure

In order to achieve a high capacity for lithium ion (Li+) storage, several features must be present, including a significant specific surface area, prominently visible aspects, and short diffusion distances. Utilizing a two-dimensional (2D) framework in a material can effectively enhance these properties. Moreover, the benefits of open charge transfer and the structural stability exhibited during the process of intercalation and deintercalation of Li^+ ions are advantageous for achieving the same goal. Extensive research has been conducted to enhance the practicality of nanostructured TiO_2 as an anode material for lithium-ion batteries (LIBs). This has led to exploring various two-dimensional (2D) nanostructured frameworks of TiO_2, such as nanosheets, nanoflakes, nanobelts, and nano hollow spheres.

In their study, Chen et al. (year) presented the synthesis of ultrathin carbon-supported anatase TiO_2 nanosheets (referred to as C-TiO_2 NS) using a straightforward solvothermal method consisting of two steps. The sample exhibits enhanced electrochemical performances compared to antase-TiO_2 due to its high electronic conductivity of carbon. The observed results demonstrated a notable specific charge/discharge capacity of 203 mAhg-1 and 314 $mAhg^{-1}$. At a charge/discharge rate of 1C, approximately 100% of the theoretical capacity of anatase TiO_2 was maintained at 170 $mAhg^{-1}$. However, at a higher current rate of 5C, the capacity decreased to 88% of the theoretical capacity after 100 cycles. Despite this decrease, the results remain highly promising. The improved rate capability and high cycle efficiency can be attributed to the presence of a highly stable microstructural architecture, which is facilitated by the existence of void space and exposed (001) energy facet [335]. In a separate study, J. S. Chen successfully synthesized high-purity anatase TiO_2 nanosheets using a straightforward hydrothermal method. The morphological analysis conducted using Field Emission Scanning Electron Microscopy (FESEM) and Transmission Electron Microscopy (TEM) indicated (as shown in Figure 2.15) that the nanosheets in their original state exhibited a square shape with dimensions ranging from 20 nm to 100 nm, and a thickness of 10 nm. The aforementioned dimensions offer significant benefits by enhancing the structural integrity of the system during the process of lithium ion insertion and extraction, thereby mitigating the effects of volume change. Furthermore, it should be noted that these average dimensions played a significant role in the exposure of approximately 62% of the high energy facets, specifically those oriented along the (001) crystallographic plane.[335]

Huang introduced a novel hybrid nano-structure called G-TiO_2(B) in their research. This nano-structure was created by using the synergistic impact of a one-dimensional mesoporous TiO_2-B nanobelt with a two-dimensional

conducting graphene sheet. The hybrid nano-structure was suggested as a potential anode with high power capabilities for lithium-ion batteries (LIBs). The experimental procedure utilised a hydrothermal approach with the addition of a graphene sheet, and then the calcination at an elevated temperature of 400^0C over a period of 4 hours. The meticulous hybrid nanostructure under consideration exhibits promising potential for achieving enhanced electrochemical performance. This is primarily attributed to its possession of one- dimensional mesopores, which facilitate efficient transport of Li^+ ions by minimizing diffusion distances. Moreover, the utilization of nanostructures facilitates enhanced interfacial interaction between the anode's surface and electrolytes, thereby facilitating efficient electron transport pathways. Moreover, the inclusion of a graphene sheet further enhances electron conductivity, making it an excellent choice for serving as a superior current collector. Graphene demonstrates substantial investments in terms of its elevated specialized capabilities and rate performances. Ding et al. (2019) successfully synthesized hollow spheres of TiO_2 that possess prominently exposed energy facets oriented along the (001) crystal plane. [336]. The microspheres consisted of nanosheets that have a remarkably thin structure. The researchers employed a straightforward hydrothermal preparation technique, and subsequently subjected the samples to calcination at a temperature of 550^0C for a duration of 8 hours. This process successfully verified the presence of the anatase phase in the prepared samples. The first irreversible loss of capacity is estimated to be around 32%, and this might be attributable to the development of the solid electrolyte interfaces (SEI) layer along deformed lithium ion (Li^+) insertion sites. Furthermore, the reversible capacities exhibit considerably lower values in comparison. The voltage plateaus observed at 1.7 V (during the conductive swept) and 2.1 V (during the anodizing swept) demonstrate a polarization effect that exceeds that of various nanosheet TiO_2 configurations. Therefore, it is imperative to direct

attention towards examining the origins of these deficiencies in order to achieve more favorable outcomes.

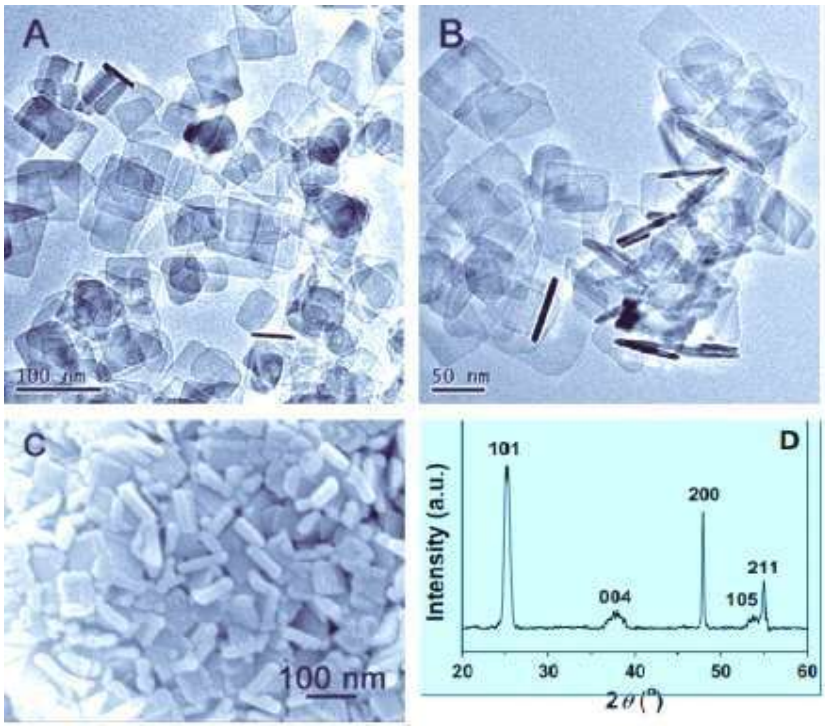

Figure 2. 15 (a),(b) TEM images, (c) HRTEM image and (d) XRD pattern of TiO_2 nanosheets (reprinted) [335]

In their study, Wu et al. successfully synthesized a TiO_2 nanosheet with a petal-like morphology using a straightforward and environmentally friendly preparation method. The initial discharge and charge capacities were documented as 382 $mAhg^{-1}$ and 326 $mAhg^{-1}$, respectively, when subjected to a low current density of 20 mAg^{-1}. Additionally, an initial irreversible capacity loss of 14.7% was observed. In subsequent cycles, the loss was reduced to zero. The extent of the loss is comparatively minimal when compared to alternative titanium-based anode materials with maximal capacity. The occurrence of this phenomenon can be ascribed to the absorption of minute quantities of water by the extensive area of surface during the process of preparation. At a significantly elevated current density of 400 mAg^{-1}, the discharge capacity over 50 cycles exhibits a noteworthy capacity retention of

93% compared to its original capacity. The observed values indicate a favorable level of cycle stability in the samples that were prepared. When considering the rate capabilities of the anode material, it can be observed that it exhibits moderate behavior. However, in order to gain a more comprehensive understanding of its rate performance, it is necessary to conduct experiments at higher rates [337].

The sandwich-like arrangement of ultrathin titanate nanosheets (CTN) supported by carbon is an innovative addition to the family of 2D nanostructures composed of titanium-based anode materials, as depicted in Figure 2.16 (a, b). Liu et al. introduced an innovative and uncomplicated approach in their research, wherein they employed the hydrothermal procedure to fabricate a structure resembling a dag-wood. The phenomenon of Oswalt ripening imposes a limitation on the process of diffusion when a certain threshold is reached. In this research, the author proposes the application of an ion exchange liquid (IL) as a prospective solvent group to tackle the aforementioned difficulties. Ionic liquids (ILs) possess a range of desirable attributes, such as low volatility, elevated boiling points, remarkable design adaptability, and noteworthy solubility. During the evaluation of electrolytic performances, it was noted that there were no discernible plateaus seen for certain charge/discharge voltages. The gradual changes in the charging and discharging capacity of CTNs can be ascribed to the distinctive structure of these materials. The enhanced development of grain boundaries can be attributed to the robust interaction between amorphous carbon and ultrathin nanosheets of TiO_2. The diffusion of Li^+ ions and charge transfer take place predominantly at the surface of carbon-based transition-metals nitrides (CTNs), which are commonly utilised in electrochemical capacitors. As a result, a dearth of clearly defined voltage plateaus was found. The investigation documented a notable high-rate capacity of 190 $mAhg^{-1}$ at 50C,

which was ascribed to the unique sandwich-like architecture and improved conductivity facilitated by carbon nanoparticles [338].

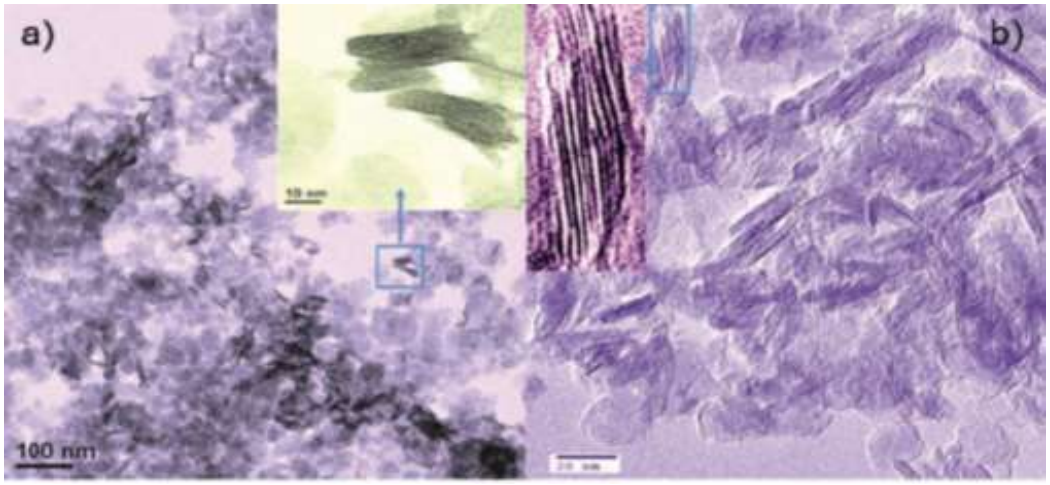

Figure 2. 16 TEM image of a) as-synthesized sandwich structure b) anatase sandwich structure (reprinted) [338]

2.4.3 Three-Dimensional Structure

The favorable qualities of three-dimensional nanostructures of TiO_2 have attracted considerable attention among investigators in the discipline of lithium-ion battery (LIB) research. These properties include the capacity to adjust pore sizes, interconnected structure, a significantly exposed surface area, and high porosity. The aforementioned features contribute to the improvement of the electrochemical performance of the material when employed as an anode. The enhancement of diffusion kinetics is mostly attributed to the supply of short diffusion lengths for Li^+ ions. An expanded surface area promotes greater infiltration of electrolytes into the electrode, resulting in improved storage of Li^+ ions. In addition, the integration of porous structures offers empty areas that help alleviate the volumetric changes that arise during the charging and discharging process, thereby maintaining the structural integrity. In addition, the interconnected nature of their structures demonstrates superior electrochemical capabilities compared to nanocrystals that are loosely packed.

The precursor utilized in this investigation for the fabrication of porous TiO_2 creatures characterized by spherical cores and shells made of nanochains was TiO_2/oleylamine. The material derived from TiO_2 demonstrates remarkable electrochemical properties, including a high ability, superior rate capacity, and outstanding cycle stability. The improved electrochemical performance can be ascribed to the unique porous structures and remarkable structural stability. Moreover, it is crucial to acknowledge that ex-situ structural characteristics offer compelling evidence supporting the claim that trace anatase nanocrystals experience an irreversible conversion into cubic Li_1TiO_2 nanodots. This transformation serves as an explanation for the relatively modest degradation in capacity observed in the porous TiO_2 material over extended cycling periods. Ongoing efforts are being made to enhance the geometric properties and pore structure of the TiO_2 material in order to achieve enhanced cycle stability. Furthermore, there have been proposals regarding the potential utilization of porous TiO_2 creatures and protonated titanates in sensitized solar cells, photo-catalysis, and adsorption processes. [339]. J.Y. Shin et al. [340] employed a straightforward in situ hydrolysis technique to effectively generate a hierarchical, nanoporous TiO_2 structure. The material demonstrates an extended ability to store lithium when used as an anode, especially in situations with rapid rates of charging and discharging, owing to its substantial surface area. The presented material exhibits two unique storage modes, specifically bulk insert and pseudo-capacitive interface storage, which jointly contribute to 64% of the total capacity. The interfacial storage is kinetically emphasized by cycling at high rates, resulting in a completely reversible discharge capacity of 302 $mAhg^{-1}$ and 200 $mAhg^{-1}$ at charge/discharge rates of 1C and 5C, respectively. Furthermore, this process exhibits exceptional cycle stability.

The researchers, G. Lui et al., introduced a new structure of TiO_2 known as a 3D-ordered macroporous interconnected (3DOM) structure in their study. The fabrication of this structure was accomplished by a direct in-situ preparation approach, utilizing polystyrene beads and carbon cloth as the template materials. The TiO_2 structure that was obtained demonstrated a remarkably high initial capacity of 402 mAhg-1, that can be attributed to the substantial presence of carbon content. In addition, voltage plateaus were observed at a rate of 1.79 V from the charge/discharge curve.

The voltage value of 1.9 V exhibits a reduced plateau region and an elevated slope region. This suggests that the porous interconnected structure is responsible for improved interfacial lithium storage. At a significantly elevated current density, the material retained a capacity of 69 $mAhg^{-1}$ at a temperature of 73.5°C, which can be attributed to its ability to maintain a high degree of structural stability through its porous architecture.[341]

X. Wang et al. presented a novel homogeneous yolk-shell hierarchical TiO_2 macroporous structure (referred to as HYSM) in Figure 2.17 (a, b), which was fabricated using a straightforward solvothermal method. The sample that was prepared demonstrated a notable initial discharge capacity of 267.6 $mAhg^{-1}$ at a rate of 0.25 C and maintained a capacity of 191 $mAhg^{-1}$ even after undergoing 40 cycles. These results indicate a robust electrochemical performance, suggesting that the sample holds promise as a potential anode material for lithium-ion batteries. The exceptional electrochemical performances observed in this study can be attributed to the distinctive hierarchical structure of the yolk-shell, which provides short routes for Li-ion and electron transport. Additionally, the structure offers a sufficient elastic buffer area to accommodate significant volume fluctuations.[342]

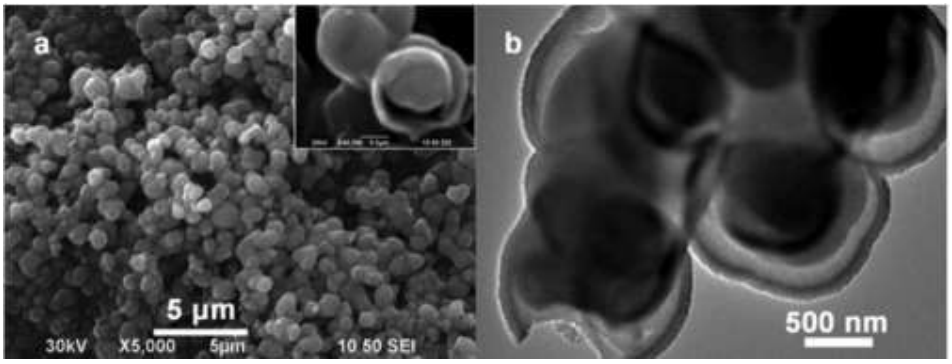

Figure 2. 17 (a) SEM (b) TEM images Yolk-shell TiO2 (reprinted) [341].

The sacrificial templating method is a widely employed technique for the synthesis of nanostructured TiO_2. The bio-ingredients templating method has garnered significant attention in research, as it involves the utilization of living organisms as templates. The contribution of bio templates to the enhancement of specific surface area, exposure of the skeleton, and interfacial density has been duly acknowledged. Various microorganisms, including bacteria, fungi, animal cells, and plant cells, serve as templates for studying molecular subunits such as proteins, enzymes, and DNA. Both yeast and glucose have been separately identified as template contributors in the pore formation process of TiO_2 nanostructures. Y. Chang successfully synthesized a novel macroporous anatase TiO_2 sample, denoted as PT, utilizing yeast and glucose as bio templates. The sol-gel method was employed to create the macroporous structure, with pore sizes ranging from 2.5 nm to 3 mm and mesopores measuring between 4 nm and 51 nm. The individuals worked together in order to collectively produce the ultimate porous structure. The presence of a porous topology facilitated the existence of extensive surface areas and unobstructed voids. Due to the facile intercalation and deintercalation of lithium (Li), the material exhibited favorable performance as an electrode material in lithium-ion batteries, demonstrating significant capacity retention. The electrochemical properties of porous TiO_2 were

significantly enhanced by the incorporation of a carbon-coated network. The hierarchical porous structure demonstrated a notable diffusion coefficient, as well as exceptional cycle stability and rate efficiency, which are essential characteristics for the effective operation of rechargeable batteries under high-rate conditions. [343]

Doping serves as an additional approach to enhance the electrochemical performance of the titanium dioxide (TiO_2) anode in lithium-ion batteries (LiBs). The elements iron (Fe), tin (Sn), zinc (Zn), and niobium (Nb) have been subject to extensive investigation. Numerous studies have demonstrated that nitrogen-doped titanium dioxide (N-doped TiO_2) exhibits exceptional anodic performance and notable availability, rendering it one of the most promising candidates in this domain. In their study, G. Hasegawa et al. successfully produced a three-dimensional N-doped TiO_2 material by utilizing ethylenediamine macroporous organic-inorganic hybrid gels based on titanium. The N-doped TiO_2 samples were prepared and subsequently calcined at various temperatures (400^0C, 500^0C, 600^0C, 700^0C) under ambient conditions. This thermal treatment led to the formation of a hierarchal porous structure consisting of macro-micro pores of different sizes, with the interstices being occupied by TiO_2 crystallites. In contrast, the calcined samples at a temperature of 500^0C exhibited superior electrochemical performances. The presented samples exhibited reversible discharge capacities of 252 $mAhg^{-1}$ at a rate of 20 mAg^{-1} and 172 $mAhg^{-1}$ at a higher rate of 200 mAg^{-1}, within the voltage range of 1.9 V to 2.1 V. An impressive cyclic performance, with a capacity exceeding 200 $mAhg^{-1}$ at a rate of 100 mAg^{-1}, was observed over a span of 300 cycles. The enhancement of electrochemical properties can be ascribed to both the presence of a porous hierarchical structure and the introduction of nitrogen doping. The enhanced electron conductivity and improved Li^+ ion diffusivity can be attributed to the

incorporation of nitrogen doping, despite its relatively low concentration. Moreover, the introduction of nitrogen into the Ti-O lattice bonding may have an impact on the electrochemical reactions occurring at the interface between the electrolyte and the active material, potentially influencing the overall performance. [344]

F. Di Lupo et al. [345] have presented a straightforward and efficient hydrolytic method for the synthesis of mesoporous TiO_2 nanocrystals (TiO_2-NC). In this process, the researchers employed tetra butylammonium bromide surfactant. The electrochemical performance of these materials as anodes for high-rate Li-ion batteries at room temperature was effectively demonstrated, even after undergoing an extensive number of cycles exceeding 1000. The samples were comprehensively characterized using X-ray diffraction, transmission electron microscopy, nitrogen physisorption studies, and electrochemical methods. A novel synthesis method was employed to produce a mesoporous TiO_2 anatase phase with a specific surface area of 258 m^2g^{-1} and a notable level of crystallinity, eliminating the requirement for additional post-synthesis treatments. Additionally, the material underwent calcination at temperatures ranging from 250^0C to 550^0C in order to promote crystallization and evaluate the influence of structural modifications on electrochemical characteristics. The impressive rate capability and exceptional stability exhibited by the produced materials indicate their potential for utilization in next-generation high-power lithium-based batteries, even when subjected to highly extended cycles.

2.5 Nanostructured TiO_2 by Electrochemical Anodization

The utilization of potentiostatic anodization as a method for the fabrication of nanostructured TiO_2 is highly significant and has garnered considerable attention in academic research. Various methods can be employed to achieve nanostructure. However, it is important to consider the presence of a highly

ordered and densely packed structure with appropriate alignment. This can be effectively achieved through the process of electrochemical anodization. The self-templating method also achieved controlled geometry. However, the anodization process has emerged as a more cost-effective and easily prepared alternative, leading to increased interest and potential for widespread applications [346]. In their research paper, X. Quan et al. (year) demonstrated the successful growth of highly organized and densely packed titanium dioxide nanotubes (TNT) with pore diameters ranging from 30 nm to 90 nm and lengths between 300 nm and 500 nm. This growth was achieved through anodization, utilizing an optimized voltage parameter of 20 V and a 0.2 wt% hydrofluoric acid (HF) aqueous electrolyte solution (Quan et al., page number). However, diverse outcomes have been documented by altering the anodization parameter. Positive outcomes were obtained by Ruan et al. through the anodization of a pure titanium substrate using 4 wt% hydrofluoric acid electrolytes in an organic solution. A surface structure composed of well-aligned TiO_2 nanotubes, characterized by an inner pore diameter of 60 nm, a thickness of 40 nm, and a length of 2.3 μm, was successfully generated through the application of a 20 V direct current (DC) supply for a prolonged duration of 72 hours. The obtained results have garnered significant attention, prompting further research into optimizing anodization parameters such as electrolyte combination, temperature, agitation, applied voltage, anodization time, pH, etc. This is done in order to gain a deeper understanding of the mechanism behind nanostructure formation and to explore potential applications in future research endeavors. [347]

The process of anodization of titanium is an electrochemical phenomenon in which a Pure Ti substrate or a titanium alloy serves as the anode, while Pt or graphite is used as the cathode simultaneously. The application of voltage

over a specific duration results in the development of a bilateral oxidation layer and the dissolution of the oxide layer into the electrolyte. When the reaction rates of these two substances reach equilibrium, a stable dimensional structure emerges, leading to the formation of various types of nanostructures. Nanostructures with precisely controlled dimensions, such as wall thickness and length, can be achieved through the manipulation of certain parameters during anodization. These parameters include the applied voltage, time, and electrolyte composition, which contains F- ions. The tapered, conical-shaped TiO2 nanotube, as depicted in Figure 2.18 (a,b), was introduced by G.K. Mor et al. The authors observed that the influence of voltage sweep rates on light emission was evident. The researchers have demonstrated the impact of a gradual increase in applied voltage ranging from 10 V to 23 V, with a rate of 0.43-2.0 V per minute.

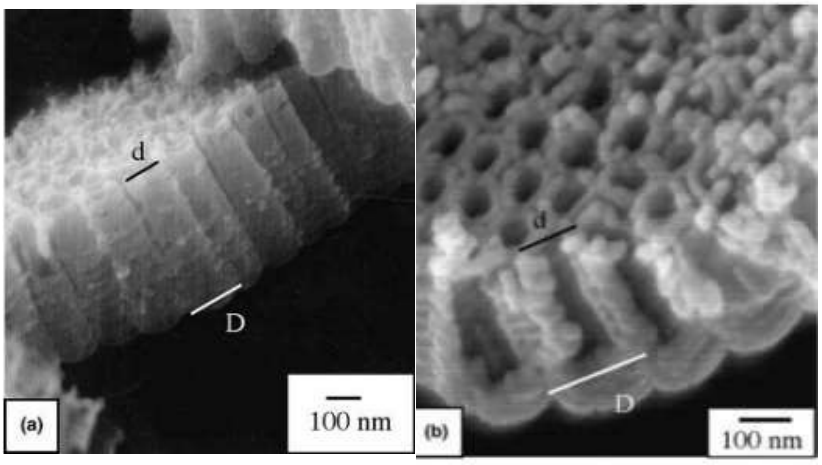

Figure 2. 18 (a) Tapered nanotubes obtained using the ramp rate of 0.43V/min to raise the voltage from 10–23V within 30 min and then holding the voltage at 23V for 10 min. (b) Tapered nanotubes obtained by initially anodizing the sample at 10V for 20 min (reprinted) [348].

The lowest inner diameter of 65 nm was achieved at a voltage ramp rate of 0.43 V/min and subsequently increased as the voltage ramp rate increased. However, when the voltage is applied in the reverse direction, ranging from

23 V to 10 V, at various sweep rates, there is no observable impact on the tapered shape. Furthermore, nanotubes exhibiting consistent diameters have been observed during the application of a constant voltage ramp. It is evident that the application of voltage at an increasing sweep rate has a discernible impact on the progressive expansion of the oxide layer, resulting in the formation of conical tubular structures.[348]

In their study, Gong et al. successfully fabricated TiO_2 nanotube arrays with diameters ranging from 25 nm to 65 nm through the process of anodizing a pure Ti substrate. The resulting arrays exhibited a high density and demonstrated self-organization and self-growth characteristics. This study demonstrates a direct correlation between the increase in voltage and the corresponding increase in tube diameter. However, beyond a specific threshold of applied voltage, the nanotube structure becomes indistinct. Once more, it was observed that a greater potentiostatic effort was required to achieve a well-defined tubular architecture in a dilute electrolyte solution of hydrofluoric acid (HF). This suggests that the concentration of the HF solution has a significant influence on the formation of nanotubes. Research has also demonstrated that the duration of time is indeed a factor. However, it has been observed that over an extended period, this duration does not have any discernible effect on the thickness or depth of the tube. [349]

In their study, Liu et al. introduced a straightforward approach for the synthesis of nanotube TiO_2 using a two-step anodization method. The initial stage of anodization, conducted at a voltage of 60 V for a duration of 1 hour, resulted in the formation of a well-organized array of nanotubes. The average diameter of these nanotubes was approximately 140 nm, while the thickness of their walls measured around 15 nm. The nanotubes obtained through the final step of anodization, conducted at a voltage of 20 V for a duration of 1

hour, exhibited a compact structure and possessed a small diameter while exhibiting no discernible defects.

Zwilling et al. conducted a study on the anodic oxidation of pure Ti substrate and TiA_6V alloy (composed of 6% Ti and 4% Al) using chromic acid (CA) at a concentration of 0.5 mol/L. The investigation also involved the addition of hydrofluoric acid (HF) at a concentration of 0.0095 mol/L, which served as a source of fluoride ions (F^-). This study provides further evidence that the inclusion of F^- ions facilitates the development of a porous structure, as the absence of HF in the CA electrolyte solution resulted in the absence of any observable porous layer. The objective is to discuss the process of pore initiation and subsequent removal of metal ions from the bottom of pores in a metal or alloy substrate. This occurs as a result of the breakdown of the thin, compact layer that forms in a corrosive agent (CA) solution at a rate of 3 V/se. The repair of this layer is facilitated by a significant associated current. The thickening of both the compact layer and the duplex porous layer is facilitated by the residual current. The electrochemical efficiency exhibits a maximum value of 50% and experiences a significant decline as the anodizing period increases. The chromium species present in the CA solution exhibited a detrimental effect on the growth dynamics, while the fluoride species acted as an antidote.[350]

The crucial role of electrolytes in the anodization mechanism is well-established. Consequently, researchers have been diligently investigating modifications to the electrolyte solution over an extended period of time in order to identify the necessary adjustments and obtain valuable insights. Research findings have demonstrated the successful growth of highly organized titanium nanostructures at room temperature through anodization, with the crucial requirement of incorporating a source of fluoride ions (F^-) in the electrolyte solution [351]. A distinct nanotube texture was observed in a

pure electrolyte solution containing 0.5 wt% hydrofluoric acid (HF). The tube length is observed to increase up to 2.5 μm when using a neutral electrolyte solution containing Na_2SO_4, $(NH_4)_2SO_4$, and NH_4F. This phenomenon can be attributed to the higher dissolution rate of Ti4+ ions from the Ti substrate in this particular solution [352]. The utilization of an F-based organic electrolyte, which incorporates an organic solution such as Ethylene glycol (EG), effectively addresses the problem of surface roughness. The presence of EG in the electrolyte solution slows down the movement of ions, resulting in a controlled and smooth etching process of metal ions, as illustrated in Figure 2.19. EG, also known as ethylene glycol, is a fluid characterized by its high viscosity and a significant level of homogeneity. These properties contribute to the reduction of the diffusion constant of the electrolyte. The initiation of EG pits allows for the confinement of the pH burst to a specific location and the localized suppression of concentration. The outcome of this procedure yields a significantly elongated tube length of up to 1000 μm, exhibiting a high aspect ratio. This is achieved through the utilization of an organic solution during a multistep anodization process, which effectively transforms the oxide film into a tubular architecture with a hexagonal shape. Once again, it has been demonstrated that the utilization of F- free electrolytes, such as $HClO_4$, leads to the formation of disordered and shorter nanotubes [353]. The optimization of the concentration of F^- species is a crucial factor that must be taken into consideration. The utilization of an electrolyte with a significantly low weight percentage of F^- species (< 0.5 wt%) leads to the formation of a non-uniform porous structure characterized by a scattered and uneven distribution of pores on the titanium substrate. The optimal outcome was observed for a concentration range of 0.5 - 1 wt%, characterized by a well-organized and substantial (2.5 μm) porous architecture. Conversely, concentrations exceeding 1 wt% did not yield a significantly enhanced structure, likely due to the solubility of F-ions acting as a constraining factor.

As previously stated, pH is a critical parameter in the process of anodization. By adjusting the pH level, it becomes possible to regulate the chemical dissolution of TiO_2. An increase in pH value leads to an enhancement in chemical etching and a simultaneous reduction in the thickness of the oxide layer. The presence of acidic ambient conditions enhances the corrosive nature of metals, leading to increased metal degradation. There are multiple factors that exert an influence on the pH value of the electrolyte during the process of anodization [354]. The local acidity observed in this context is attributed to the generation of hydrolysis products at the working electrode. The extension of tube length was facilitated by adjusting the localized acidity to promote the degradation of TiO_2 and create a more safeguarded environment to prevent dissolution in the vicinity of the tube opening. The counter electrode is the site at which the process of hydrogen formation and the generation of OH^- species occur. [355, 356]

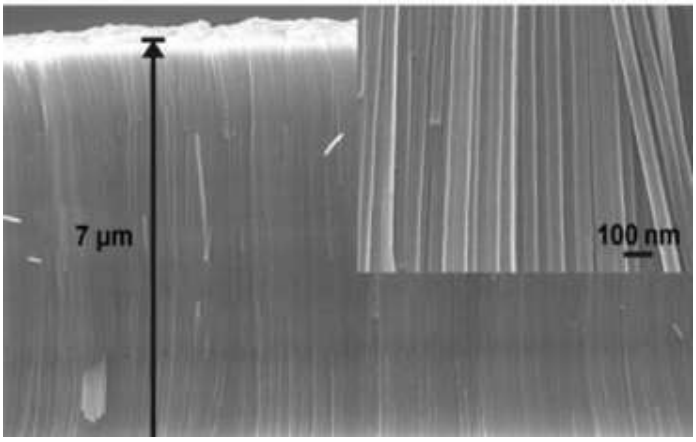

Figure 2. 19 TEM image of smooth nanotube in 0.5 wt% NH_4F based electrolyte (reprinted) [353].

TNTs have been synthesized using electrolytes that do not include fluoride ions. Hahn et al. [357] employed anodization techniques using perchlorate and chloride-containing electrolytes to produce TNT with an enhanced aspect ratio. The anodization process involved the utilization of electrolytes containing oxalic, formic, or sulfuric acid electrolytes with the inclusion of

chlorine ions. Electrolytes that are chlorine-based and do not contain fluoride offer a distinct benefit in comparison to electrolytes that incorporate fluoride. The utilization of a fluoride-free electrolyte has been observed to significantly expedite the formation of long TNT molecules compared to fluorine-based media. For instance, the time required for this process is reduced from 17 hours to just 10 minutes, resulting in a thousand-fold increase in the rate of TNT formation [358]. The rapid evolution of bromide-based solvents in TNT was observed, although the mechanisms behind self-organization and shooting alignment remained unclear [359]. The utilization of previously employed electrolytes for anodization has also demonstrated favorable outcomes, leading to improved nanostructures [360]. The utilization of electrolytes for a subsequent application demonstrated an enhancement in pore diameter, accompanied by a reduction in wall thickness, resulting in a convergence towards a higher chemical etching rate. The observed enhancement in electrolyte conductivity can be ascribed to its utilization in subsequent anodization processes. As a result, it enhances the rates of chemical reactions and contributes to the improved formation of TNT. [361]

The dissolution rate of metal oxides and the size of pores are influenced by different current densities. The rate of electrochemical etching, power consumption, and electric field intensity are all directly proportional to the current density. Pits exhibit a tendency to enlarge before the formation of channels, which subsequently partition the pores. The increase in Ti foil current density is accompanied by a corresponding rise in the pore size of TNT. Consequently, altering the current density has the potential to result in diverse tube widths [362]. The presence of an aqueous electrolyte facilitates a convenient pathway for the flow of electric current. Hence, it can be inferred that the current density in this particular scenario is greater compared to the organic solution [363]. According to the research findings presented in

reference [364], it has been observed that the formation of TNT (titanium nanotubes) is not possible during anodization processes lasting less than 5 minutes. However, after the 10-minute mark, the formation of nanotubes begins. Increases in solution temperature have been found to enhance the development of pores. This phenomenon can be attributed to the inverse relationship between temperature and the viscosity of the electrolyte, which leads to an accelerated etching process. When the rate of the etching process is increased, the oxide layer experiences a more rapid degradation, leading to the formation of pores. The dispersion of fluoride ions was observed to decrease at lower temperatures, leading to a corresponding reduction in the rate of etching. At lower temperatures, the development of consistent holes was not observed due to the sluggish etching rate of the oxide layer [365, 366]. The simultaneous optimization of applied voltage and time scale has a significant positive impact on the outcomes of anodization. When the potential applied is below 50V, the porous oxide undergoes a self-organized process, resulting in a densely packed texture. The process of anodization over a brief duration yields a structured arrangement of tubular oxide film, characterized by a length on the order of a few hundred nanometers and a diameter on the order of a few tens. Ripples emerged at the interconnectivity junction of these nanotubes. However, over time, these ripples gradually vanished due to the dissolution of TiO_2. Once the applied voltage reaches or exceeds 50 V, the layer undergoes a transformation into a localized burst morphology, resembling the appearance of coral reefs as depicted in Figure 2.20 (a, b). The formation of an ordered array structure at higher potentials has been observed [367]. Bio-sensitive TiO_2 hexagonal nanotubes are synthesized on Ti_6Al_4V and Ti_6Al_7Nb alloys using organic ethylene glycol and glycerol solutions. The annealed Ti_6Al_4V sample at a temperature of 550^0C demonstrated the presence of a homogeneous and evenly distributed oxide

layer consisting of both rutile and anatase phases. The sample that was treated with glycerol exhibited a higher degree of bio-sensitivity. [368]

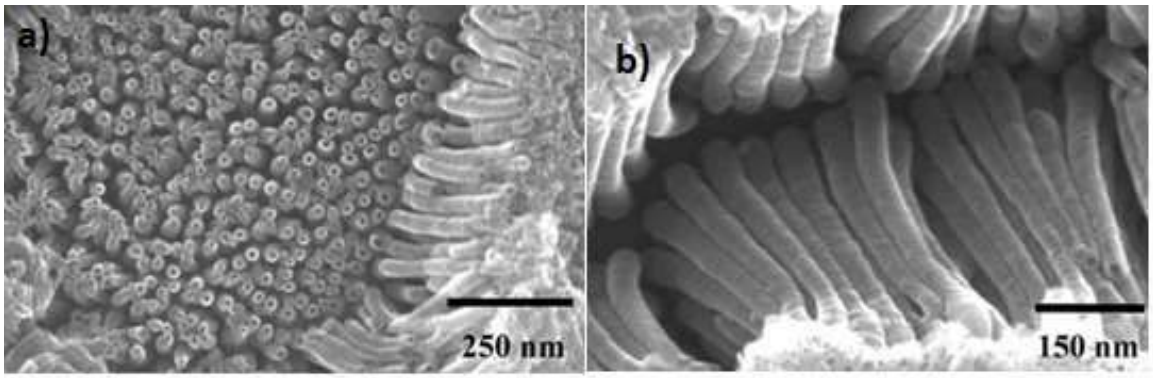

Figure 2. 20 SEM image of TiO_2 'coral reefs' nanotube structures formed at 50V in CH_3COOH+0.5wt% NH_4F solution a) inside and b) outside (reprinted) [367]

2.6 Anodized TiO_2 as promising Anode of LiBs

The process of electrochemical anodization of titanium leads to the formation of nanostructured titanium dioxide, which provides the ability to adjust the dimensions of the resulting structure. The utilization of a well-aligned and self-organized TiO_2 nanostructure array presents a promising opportunity for its application as a potential anode material in Lithium-ion Batteries (LiBs). The utilization of nanostructures is advantageous due to their high surface area, which facilitates the desired electrochemical properties. This is achieved by reducing the pathway for Li^+ ions, enhancing ionic conductivity, and providing structural stability during Li^+ insertion and deinsertion. Consequently, the reduction of the polarization effect at the anode occurs, leading to an increase in the discharge capacity with a high charge. [346]

The investigation conducted by S. Ivanov and colleagues focused on the characterization of amorphous and crystalline TiO_2 nanotubes prepared anodically. The study involved conducting electrochemical analyses in two distinct electrolyte environments: a solution consisting of 1 M $LiPF_6$ in ethylene carbonate/dimethyl carbonate (EC: DMC), and a solution containing

1MLi[TFSI] in 1-buthyl-1-methyl pyrrolidinium, (trifluoromethyl) sulfonylimide ([BMP][TFSI]). The latter scenario exhibited a slightly greater electrochemical efficiency as a result of its inert nature towards the anode surface and exceptional stability. In contrast, the initial type of side reaction exhibits instability when exposed to water. Both the amorphous and crystalline materials exhibited a significant charge/discharge capacity ranging from 180-200 $mAhg^{-1}$, which can be attributed to the presence of an open hierarchal structure. The amorphous samples demonstrated complete retention of capacity, whereas a decrease in capacity was observed in the crystal structure. The presence of surface defects resulting from heat treatment can be attributed to this phenomenon.[369]. In a study conducted by Li et al., it was observed that the synthesis of highly stable nanotubes can be achieved through the utilization of ionic liquid (IL) during anodization, as opposed to the conventional use of NH_4F, EG (AF) based electrolytes. The presence of microstructural cracks on the calcined anatase crystal TiO_2 nanotubes, as depicted in Figure 2.21 (a,b), can be attributed to the carbonaceous product. The rapid decomposition of the unstable AF electrolytes, which forms a composite with the anode, is the underlying cause. The electrochemical behavior of IL nanotube products exhibited remarkable performance, as evidenced by their capacity retention of over 1200 cycles. Throughout these cycles, the samples remained intact with minimal material loss, which can be attributed to their high conductivity and consequent slow decomposition rate. In contrast, it can be observed that AF-based products experience a decline in capacity after approximately 380 cycles, which may suggest a gradual breakdown of their structural integrity. [370]

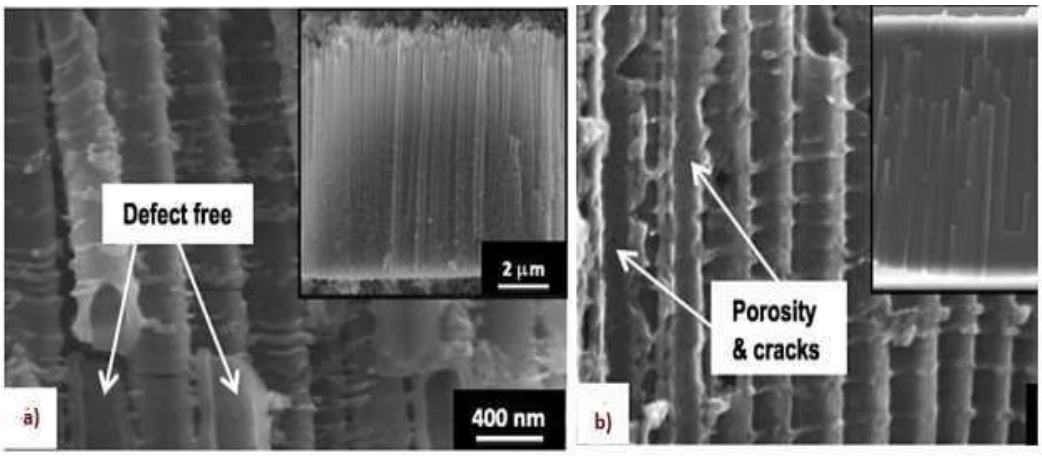

Figure 2. 21 Cross-section of (a) ILNTs and (b) AFNTs. Insets in (a) and (b): low- magnification side views showing tube lengths (reprinted) [370].

The detrimental consequences of carbon contamination in nanotube structures are swiftly evident. The authors, R. Kirchgeorg et al., have successfully fabricated a self-organized nanotube array characterized by a high degree of order and a tube length of 32 μm. However, this array demonstrated a lower insertion efficiency. The decrease in efficiency can be attributed to the longer tube, as the increased length results in a higher level of carbon contamination. The phenomenon known as the double layer effect involves the presence of a nanograss coating that is responsible for the generation and distribution of surface charges. The dissolution methods employed to assess the carbon content involve the utilization of a mixture comprising ethylene glycol and dimethyl sulfoxide, as well as an aqueous solution of Na_2SO_4. These approaches have resulted in a respective increase in charge of 33% and 17%.[371]

In a study conducted by Ryu et al., it was demonstrated that amorphous TiO_2 nanotubes exhibit a more efficient mechanism for Li^+ ion intercalation compared to the crystalline anatase structure. This enhanced performance can be attributed to the amorphous nanotubes' ability to accommodate a greater amount of lithium per TiO_2 unit (x=1), whereas anatase can only

accommodate a maximum of 0.5 lithium ions. The phenomenon of the initial irreversible capacity can be attributed to the occurrence of side reactions involving water molecules and the partial crystallization of trapped Li^+ ions. Furthermore, amorphous TiO_2 nanotubes exhibit several advantages over anatase nanotubes, including the absence of inherent phase transition strain, high-rate capability, desirable cycle performance, and superior reversible charge/discharge capacity. These characteristics further support the notion that amorphous TiO_2 nanotubes provide a facile pathway for Li^+ insertion/deinsertion. However, the presence of dispersed spatial defects on the amorphous surface results in reduced electronic conductivity and promotes the formation of the anatase structure. Furthermore, the extended durability of bulk nanotube structures is not well understood [372]. D. Guan's study [373] provides additional support for the aforementioned argument by demonstrating the high lithium ion insertion capacity of amorphous TiO_2 nanotubes. The amorphous TiO_2 nanotubes, prepared anodically, exhibited a notable specific capacity of 533 $\mu Ahcm^{-2}$ at an applied current density of 400 μAcm^{-2}. Furthermore, the nanotubes demonstrated a capacity retention of 77% after undergoing 50 cycles, as depicted in Figure 2.22. This phenomenon can be attributed to the high diffusion coefficient of lithium and the structural stability exhibited by the amorphous state. In contrast, the anatase phase and the mixed anatase-rutile phase exhibited relatively subpar performance. The underlying causes of certain crystal defects in anatase. The application of voltage plays a significant role in shaping the morphology of nanostructures, and it also serves as an important parameter for determining electrochemical behavior. The formation of a nanotube array film through sequential anodization at 20 V and subsequent annealing results in a film that exhibits satisfactory cyclability. However, it displays a relatively low initial capacity of 180 $mAhcm^{-3}$, which can be attributed to the narrow opening of the nanotubes. The observed phenomenon of enhanced intercalation capacity is

attributed to the application of higher voltages, specifically 40 V and 60 V. However, when subjected to significantly higher voltages (80 V and 100 V), the tube wall experiences erosion and exhibits a collapsed morphology, resulting in poor cyclability [374]. Nanotubes that exhibit a high degree of order consistently provide a convenient pathway for the mechanism of lithium intercalation, resulting in improved reversible capacities. This correlation is particularly evident when the nanotubes possess thicker walls. In their study, W. Wei et al. successfully synthesized a tubular nanostructure with a length of 9 μm. This nanostructure exhibited a high-rate capability of 96 $mAhg^{-1}$ (0.24 $mAhcm^{-2}$) when subjected to a two-step annealing process. The battery underwent 500 cycles at a rate of 0.1 C, demonstrating outstanding performance with a mere 6% initial capacity loss. This can be attributed to the battery's stable architecture, which effectively absorbs the volume strains that occur during the process of intercalation and deintercalation. [375]

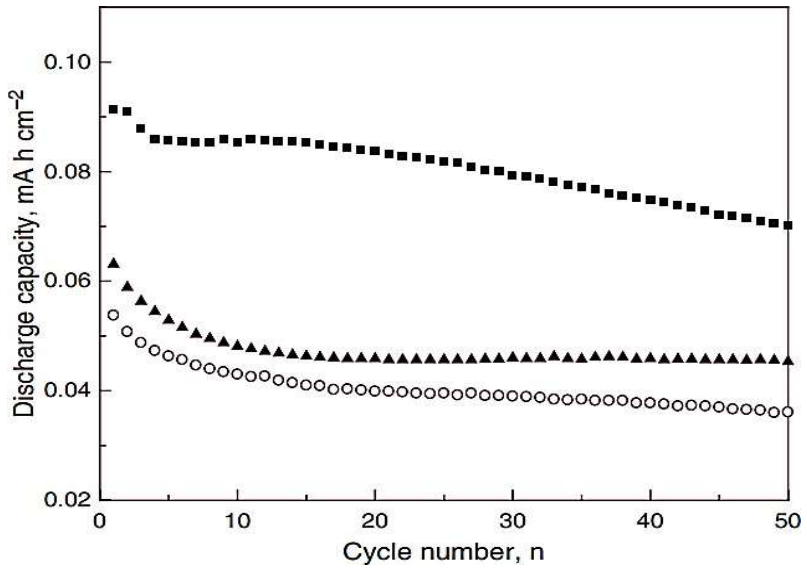

Figure 2. 22 Specific discharge capacity versus cycle number for the amorphous TiO_2 nanotube arrays (solid squares), anatase TiO_2 nanotube arrays (circles), and TiO_2 nanotubes of mixed phases (solid triangles), cycled at a current density of $400Acm^{-2}$. (reprinted) [373].

The relationship between specific surface area and discharge capacities has been extensively documented (see Figure 2.23). In addition, nanostructures exhibit a greater specific surface area compared to their bulk counterparts. The relationship between specific surface area and calcination temperature, as well as crystal structure, has been extensively demonstrated. The calcined nanotube at a temperature of 300^0C exhibited a significantly higher specific surface area of 78 m^2/g compared to the amorphous calcined products at 400 ^{0}C (70 m^2g^{-1}) and 500^0C (57 m^2g^{-1}). Furthermore, the figure associated with certain crystal defects demonstrates that 300^0C calcined nanotubes exhibit higher discharge capacities at various cycles compared to other products. The conductivity of TiO_2 nanotube layers can be enhanced by annealing at temperatures ranging from 450^0C to 550^0C. However, annealing at temperatures exceeding 550 ºC leads to a notable reduction in conductivity. This decrease in conductivity can be attributed to the formation of the rutile phase, which has been demonstrated to exhibit lower electrochemical efficiency. Furthermore, it should be noted that extended exposure to elevated temperatures within this range can also be attributed to increased conductivity, as stated in reference [376].

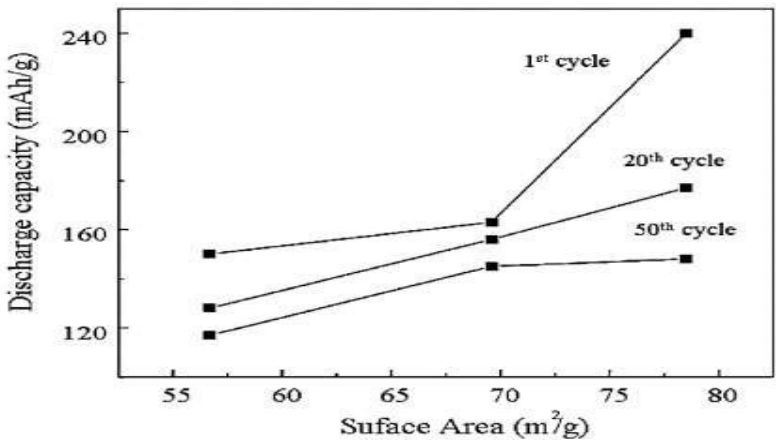

Figure 2. 23 A study of the discharge capacities of anatase TiO_2 nanotube arrays annealed for three hours at 300, 400, and 500°C in nitrogen, based on the specific surface area of the nanotubes (reprinted) [376].

The conductive properties of TiO_2 nanotube arrays can be significantly influenced by the appropriate annealing atmosphere, even with minor changes in factors such as morphology, size, and valence band structure. The sample was subjected to annealing in a reductive environment consisting of 5% H_2 and 95% Ar. This process resulted in a controlled expansion of volume, which was effectively mitigated due to the presence of a facile lithium-ion intercalation/deintercalation mechanism. The generation of a suitable quantity of oxygen bubbles serves to mitigate the repulsive forces between lithium ions, which in turn leads to the distortion of the c-length of the unit cell. This distortion plays a crucial role in significantly enhancing the high-rate capability, as demonstrated in reference [377]. The carbon-modified TiO_2 nanostructure, as reported by F. Mole et al., is achieved through the presence of a combination of 16% CH_4 and 20% H_2 in the annealing environment. The charge capacitance of this double layer nanostructure exhibited a significant increase when optimized at 40 V [378]. The electrochemical performance of Ar annealing was found to surpass that of air, exhibiting a high initial discharge capacity of 227.9 $mAhg^{-1}$, notable capacity retention, enhanced rate capability, and cycle stability. Notably, the annealing of TiO_2 at 450^0C resulted in an anatase crystal structure, which was determined to be the most beneficial among other crystal structures for TiO_2. The primary advantage of the sample with a carbon content of 5.22% is its propitious nature compared to the air annealed sample. The absence of electrochemical depth was observed when the annealing temperature was increased to 600^0C and 800^0C, resulting in the disappearance of the anatase crystal [379].

2.7 Summary

The literature reviewed in this study presents various methodologies for synthesizing nanostructured TiO_2. However, an examination of the significant

factors involved in fabrication methods will aid in addressing the challenges that arise post-synthesis, specifically in terms of cost efficiency, structural integrity, electrochemical performance, and environmental sustainability. Anatase titanium dioxide (TiO_2) exhibiting various nanostructures has been developed to address several limitations, thereby enhancing its electrochemical performance and ensuring structural stability. The forthcoming chapter will present a straightforward method for producing anatase TiO2 nanostructures, drawing upon the knowledge and findings gathered from the existing literature.

Chapter-03

Materials and Methods

3.1 Overview

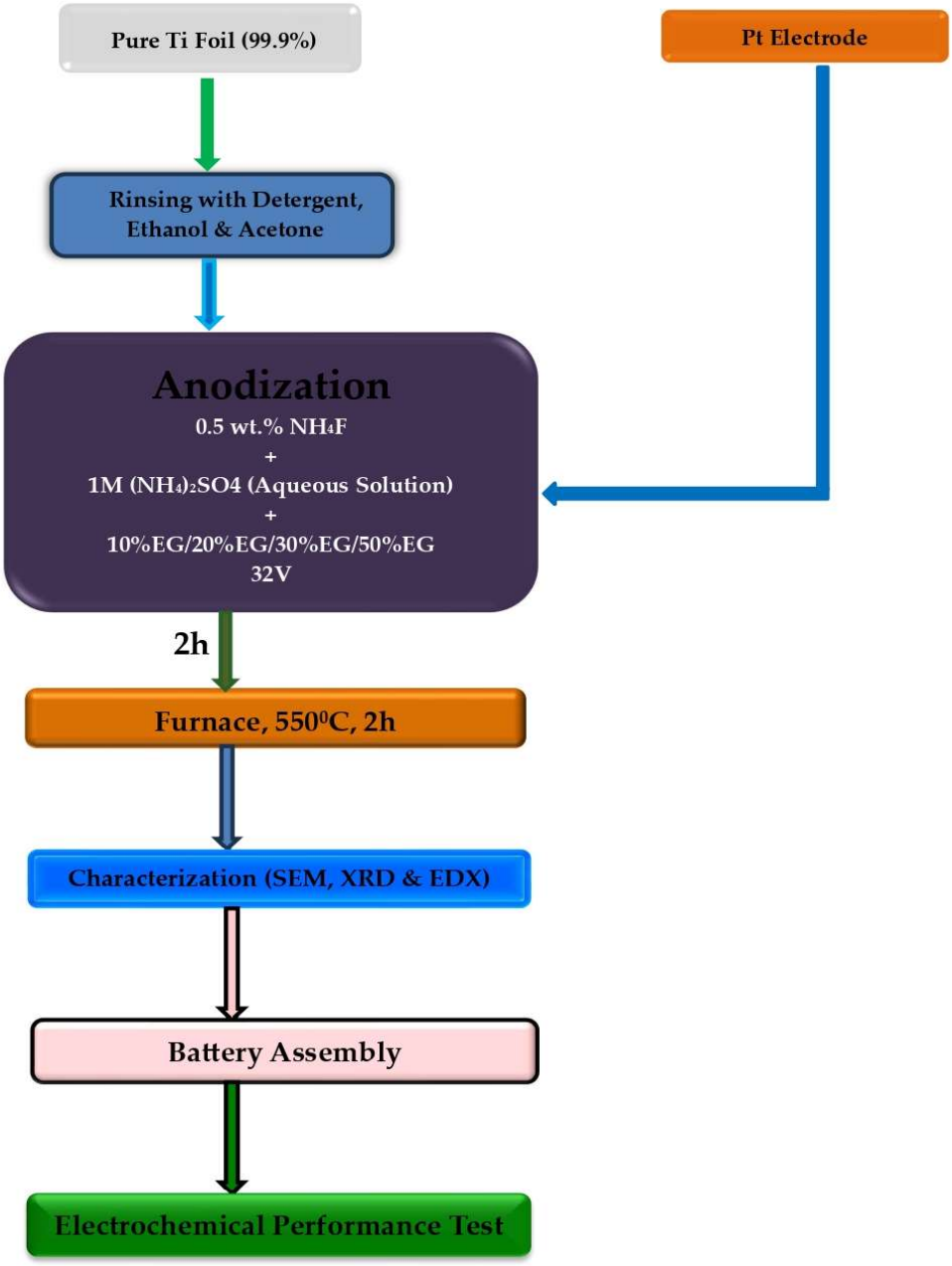

Figure 3. 1 Flow Chart of Working Procedure.

The comprehensive methodology employed in this thesis encompasses several key stages, namely material fabrication, characterization, battery assembly, and electrochemical measurements. All of these elements are depicted in a flow chart, as shown in Figure 3.1. This flowchart aims to enhance the understanding of the methodology employed in the thesis.

3.2 Chemicals and Instruments:

The chemicals and instruments utilized in this thesis are enumerated in Table 3.1 below.

Table 3. 1 Chemical and Instruments

Chemical/material/instrument name	**Formula**	**Grade**	**Reason**
Lithium Cobalt Oxide	$LiCoO_2$	100%	Cathode material
Battery Electrode Separator	Battery grade PVC	100%	As separator
Pure Titanium Foil	Ti	99.99%	As for the fabrication of anode material
Platinum Plate	Pt	99%	Electrode for Anodization
Li-Battery grade electrolyte	$LiPF_6$	100%	As electrolyte
Ethanol	C_2H_5OH	100%	Cleaning Agent
Acetone	CH_3COCH_3	100%	Cleaning Agent
Deionized Water	H_2O	100%	Cleaning Agent
Ammonium Sulphate	$(NH_4)_2SO_4$	100%	Electrolyte Solute for Anodization
Ammonium Fluoride	NH_4F	100%	Electrolyte Solute for Anodization
Ethylene Glycol	$(CH_2OH)_2$	100%	Electrolyte Solute for Anodization
Weight Balance	Weight Measuring Purpose		
Magnetic Stirrer	For Making Homogenous Mixture		
DC Power Supply	For DC Voltage Supply		

Furnace	Heat Treatment Purpose
Coin Cell Battery Case	For Assembly Purpose
Battery Crimper Machine	For Assembly Purpose
Battery Tester	For Electrochemical Performance Test
Multimeter	For Voltage and Current Measurement Purpose

3.2.1 Pure Ti Foil

The parent material of this thesis is a pure titanium foil with a purity level of 99.7%. The foil was imported from Suen Studio Co. The foil has a thickness of 0.1 mm and a width of 200 mm. Figure 3.2 depicts the titanium foil that was utilized in the present thesis.

Figure 3. 2 Pure Ti foil.

3.2.2 Pt Plate

Platinum plates, exhibiting a purity level of 99%, were procured from Suen Studio Co. These plates were subsequently utilized as cathodes for the purpose of anodization, as depicted in Figure 3..3. The plate possesses dimensions of 10mm in length, 10mm in width, and 0.1mm in thickness.

Figure 3. 3 Pt plate.

3.2.3 Ethanol (C_3H_5OH)

The 95% pure laboratory-grade ethanol utilized in this thesis for the initial cleaning of both the Ti foil and Pt plate samples was procured from Dalian Future Int. Co., China (refer to Figure 3.4).

Figure 3. 4 Ethanol.

3.2.4 Acetone (CH_3COCH_3)

Acetone was employed as the cleaning agent in the subsequent step of the sample purification process, which was obtained from a local market as depicted in Figure 3.5.

Figure 3. 5 Acetone.

3.2.5 Deionized Water

The deionized battery-grade water, which was obtained from a local market, was utilized for the subsequent third step cleaning process. This involved rinsing both the cathode and anode after each anodization, as well as preparing the anodization solution.

3.2.6 Ammonium Sulphate ($(NH_4)_2SO_4$)

The primary solute utilized in the anodizing electrolyte is Ammonium Sulphate ($(NH4)_2SO_4$), which was obtained from Suren Studio Co., China, with a purity level of 99% as depicted in Figure 3.6.

Figure 3. 6 Ammonium Sulphate.

3.2.7 Ammonium Fluoride (NH_4F)

An additional electrolyte solute, namely Ammonium Fluoride (NH4F), is essential in a minimal quantity but serves as the primary precursor for the formation of nanotubes. This particular solute was procured from Suren Studio Co., China, as depicted in Figure 3.7.

Figure 3. 7 Ammonium Fluoride.

3.2.8 Ethylene Glycol

The inclusion of an extra solute, specifically Ethylene Glycol $(CH_2OH)_2$, is necessary in a limited amount as it acts as the key precursor for the generation of nanostructures in figure 3.8.

Figure 3. 8 Ethylene Glycol.

3.2.9 Weight Balance

A precision weight balance was employed in order to quantify the various weight percentages of solutes present in the electrolyte solution. In this thesis, the SCIENTECH precision electronic weight balance (shown in Figure 3.9) was utilized. The maximum precision readability of this instrument ranges from 0.01gm to 0.001gm for weights ranging from 40 gm to 400 gm, respectively. Through the utilization of this apparatus, we conducted measurements on the concentration of NH_4F, yielding a value of 0.5 weight percent. Additionally, we determined that $(NH_4)_2SO_4$, with a mass of 13.2 grams, is equivalent to a molar concentration of 1 mole per liter in a 100 milliliter aqueous solution.

Figure 3. 9 Precision weight balance.

3.2.10 Magnetic Stirrer

In this study, a Yaeccc brand magnetic stirrer hotplate, specifically the '78-1 Magnetic Stirrer Hotplate' model, was employed to facilitate the attainment of a uniform mixture of solutes within the electrolyte. The specifications can be found in Table 3.2, which is accompanied by Figure 3.10.

Table 3. 2 Specifications of Magnetic Stirrer

AC 220V 50Hz	Power 25 W
Heat Power 150 W	Speed 2400 rpm

Figure 3. 10 Magnetic stirrer.

3.2.11 DC Power Supply

In order to obtain a direct current (DC) voltage supply for the process of anodization, a DAZHENG brand DC power supply, specifically the PS-3050 model as shown in Figure 3.11, was utilized.

Figure 3. 11 DC power supply.

3.2.12 Furnace

The furnace is a necessary requirement for the annealing process. The fabrication process employed in this study involves the utilization of a furnace for the annealing step. The electric furnace utilized in this study, manufactured by Noberthem Co., is depicted in Figure 3.12. It possesses a maximum temperature capability of 3000^0C and was employed for the purpose of annealing the anodized samples. The samples underwent a heat treatment for a duration of 2 hours at a temperature of 550^0C within the furnace.

Figure 3. 12 Electric furnace.

3.2.13 X-Ray Powder Diffraction (XRD)

X-ray diffraction data were acquired using the Empyrean, PANalytical machine from the Netherlands (see Figure 3.13).

Figure 3. 13 Empyrean, PANalytical (Netherlands) XRD machine.

3.2.14 Scanning Electron Microscope (SEM) and Energy Dispersive X-ray (EDX) Machine

SEM images and EDX spectra were taken using JSM 7600F JEOL (Japan) SEM-EDX machine, Showed in Fig.3.14.

Figure 3. 14 JSM 7600F JEOL (Japan).

3.2.15 Lithium Hexa Fluoro Phosphate ($LiPF_6$)

In this thesis, the battery grade electrolyte utilized during battery assembly was Lithium Hexa Fluoro Phosphate ($LiPF_6$), as illustrated in Figure 3.15. The product was sourced from Xiamen Tmax Battery Equipments Ltd., a company based in China. The specifications are presented in Table 3.3.

Figure 3. 15 Lithium Hexa Fluoro Phosphate.

Table 3. 3 Specifications of $LiPF_6$

Organic Solvent	EC+EMC; 3:7 in volume
Chromaticity	<50 Hazen
Moisture	≤20ppm
Free Acid (HF)	≤50ppm
Density	1.20±0.03g/ml @ 25ºC
Electrical Conductivity	7.4±0.5mS/cm
Chlorine (Cl)	<1ppm
Sulfate (SO4)	<10ppm
Potassium (K)	<10ppm
Sodium (Na)	<10ppm
Calcium (Ca)	<10ppm
Iron (Fe)	<6ppm
Lead (Pb)	<5ppm

3.2.16 Coin Cell Battery Case

The coin cell battery CR2032 coil cell cases, along with spacer and wave springs (as shown in Figure 3.16), were procured from Xiamen TOB New Energy Company Ltd. in China. The diameter of the cases is 20 mm, while their thickness measures 3.2 mm.

Figure 3. 16 CR2032 Coin cell battery case.

3.2.17 Battery Crimper

In order to secure the upper and lower-case components, which include the cathode, anode, separator, electrolyte, spacer, and wave spring, a crimping machine (Figure 3.17) was employed. The operational range of the machine spans from 0 to 250 pounds per square inch (psi).

Figure 3. 17 Battery crimper.

3.2.18 Battery Tester

The electrochemical testing in this study utilized the LAND 2001A battery tester, as shown in Figure 3.18. The data analysis was conducted by synchronizing a personal computer equipped with Land software with the tester.

Figure 3. 18 LAND CT2001A.

3.3 Experimental Procedure

The experiment can be divided into four distinct sections. They are

- Fabrication of Nanostructure Anatase TiO2
- Characterization
- Battery assembly
- Electrochemical Performance Test

3.3.1 Fabrication of Nanostructure Anatase TiO_2

a) Rinsing

In this study, a high purity titanium foil with a purity of 99.6% was subjected to oxidation to produce nanotube anatase titanium dioxide (TiO_2) using the anodization technique. The anodization process involved the use of a platinum plate as the cathode. Prior to the process of anodization, the samples, particularly titanium foils, underwent a preliminary cleaning procedure involving immersion in distilled water and detergent solution for a

duration of 30 minutes. Subsequently, the samples underwent a 10-minute cleaning process in a solution consisting solely of ethanol. Subsequently, the samples underwent a final rinsing process through immersion in acetone for a duration of 20 minutes. Following this, the samples were subjected to a drying procedure at a temperature of 105^{o}C for a period of 24 hours. The specimens were prepared for the process of anodization.

b) Anodization

Nanotube TiO_2 electrodes were manufactured using pure titanium foils (99.7%) with a thickness of 0.10 mm. The Ti samples underwent a series of cleaning steps, including ultrasonic cleaning in distilled water, ethanol, and acetone, followed by air drying at room temperature. The process of electrochemical anodization was conducted under ambient conditions using a custom-made cell featuring a two-electrode setup. The anodization method involved the utilization of a DAZHENG brand, model PS-3050 DC power supply to maintain a consistent voltage. Titanium foils with a surface area of 25.0 cm^2 were utilized as anodes, while a platinum plate with an area of 1.0 cm2 was employed as the cathode. The separation distance between the anode and cathode was consistently maintained at a value of 2.cm. The solution contained electrolytes consisting of 0.5g of NH_4F dissolved in 13.2g of 1M $(NH_4)_2SO_4$, together with varying concentrations of ethylene glycol (EG). These concentrations were 10% (electrolyte type 1), 20% (electrolyte type 2), 30% (electrolyte type 3), and 50% (electrolyte type 4). The potential was incrementally raised from 0 V to 32 V over a period of time, and thereafter maintained at this level for duration of 2 hours while maintaining a negligible current flow. The confirmation of homogenous mixing of the solutes in solution and the appropriate motions of the ions was achieved by utilizing a magnetic stirrer operating at an average speed of 400 revolutions per minute throughout the whole anodization time. Following the process of anodization,

the initial grey appearance of the anodized section of titanium foils underwent a transformation, resulting in a bluish aesthetic. Following the process of anodization, the samples underwent a 10-minute washing procedure using deionized water, and air drying at room temperature. Subsequently, all specimens were subjected to a cleansing process using distilled water, followed by their placement in a furnace for the purpose of calcination at a temperature of 550ºC for a duration of 2 hours. The entire procedure is illustrated in Figure 3.19.

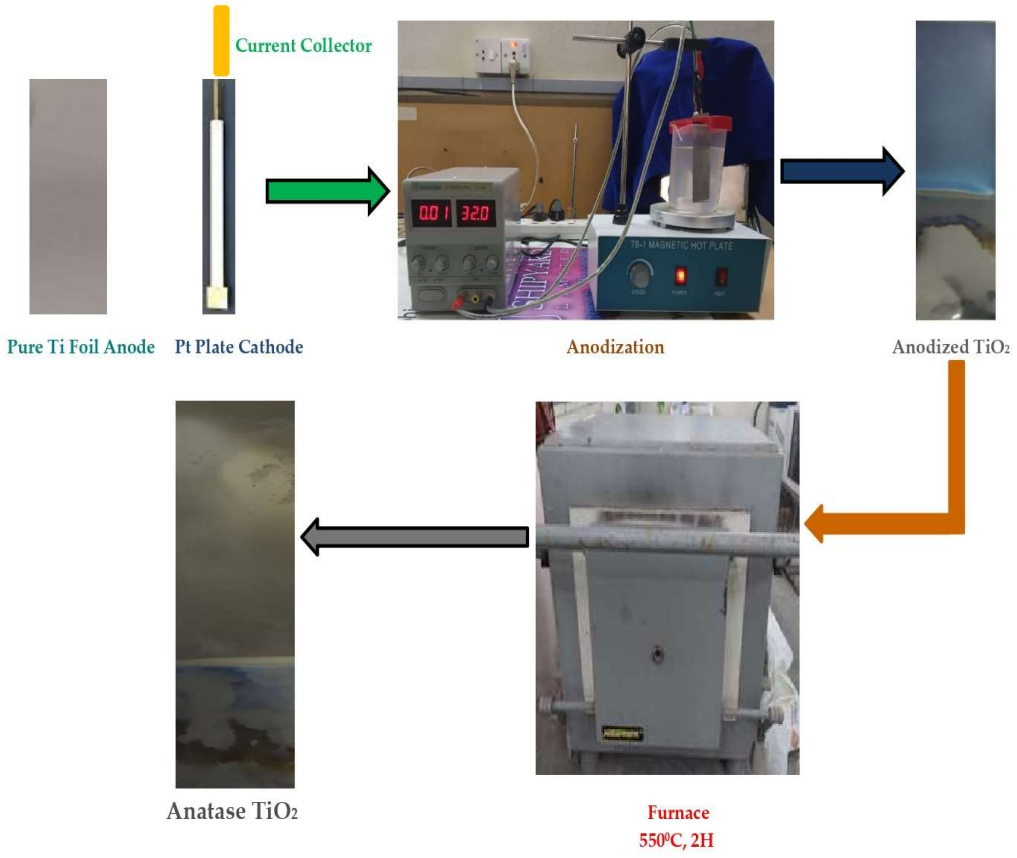

Figure 3. 19 Visual representation of fabrication steps of anatase TiO_2 nanostructure.

The furnace yielded four varieties of anatase TiO2 as the end products. These variants include 10% ethylene glycol (EG) (sample a), 20% ethylene glycol (EG) (sample b), 30% ethylene glycol (EG) (sample c), and 50% ethylene glycol (EG) (sample d). The assortment of products is visually presented in Figure 3.20 (a-e).

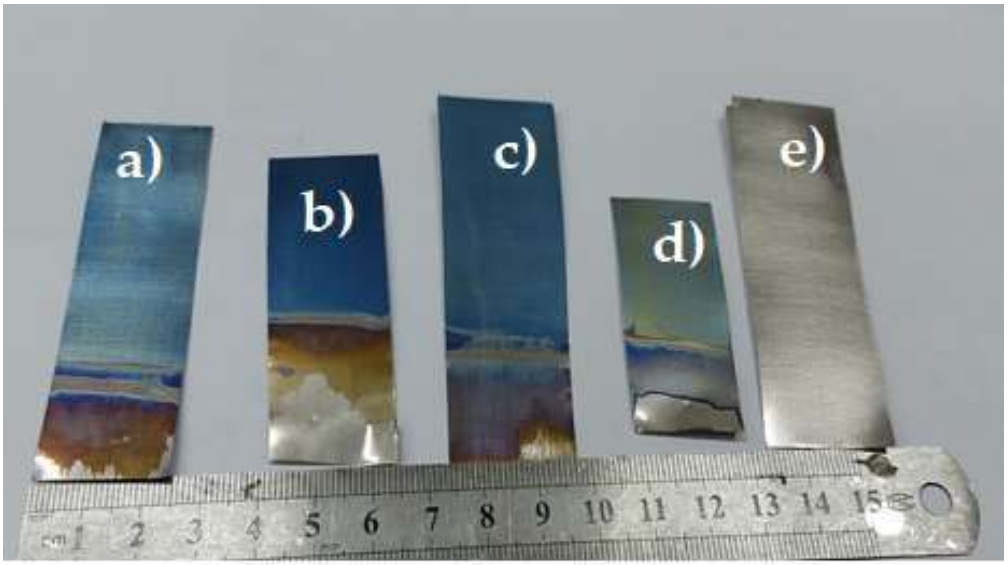

Figure 3. 20 Anodized anatase TiO_2 of (a) 10% (electrolyte type 1), (b) 20% (electrolyte type 2), (c) 30% (electrolyte type 3) and (d) 50% (electrolyte type 4) and (e) Pure Ti substrate.

c) Growth mechanism of nanostructured oxide layer via Anodization

The initiation of the dissolution process of the oxide layer occurs concurrently due to the influence of the field-assisted high polarization effect on this layer. Consequently, a significant polarization effect leads to the induction of Ti4+ cations via the breakage of Ti-O bonds. In contrast, the process of hydrogen assessment is observed at the cathodic terminal, as indicated by equation Eq.(3.1).

$$8H_3O^+ + 8e^- \rightarrow 4H_2 + 4H_2O \qquad \text{Eq.(3.1)}$$

Dissolution commences at the anode upon the application of voltage, resulting in the generation of Ti^{4+} ions as described by Equation (3.2). In addition, when water molecules undergo deprotonation, they dissociate into hydroxide (OH-) or oxide (O^{2-}) ions, both of which are present in the electrolyte. The migration of oxygen anions occurs from the oxide/electrolyte interface to the metal surface, while Ti4+ cations move from the metal/electrolyte contact to the oxide/electrolyte interface. Therefore, the formation of the oxide layer occurs in accordance with Equation (3.3). The presence of an electric field facilitates the phenomenon of ion transfer.

$$Ti \rightarrow Ti^{4+} \qquad \text{Eq.(3.2)}$$

$$Ti(OH)_4 \rightarrow TiO_2 + 2H_2O \qquad \text{Eq.(3.3)}$$

Introducing F- species initiated the chemical attack on the oxide coating, leading to the beginning of pores. Initially, a complex ion is generated through the interaction of Ti4+ ions and F- species, as represented by equations Eq.(3.4) and Eq.(3.5).

$$Ti^{4+} + 6F^{-} \rightarrow [TiF_6]^{2-} \qquad \text{Eq.(3.4)}$$

$$TiO_2 + 6HF^{-} \rightarrow [TiF_6]^{2-} + 2H_2O + 2H^{+} \qquad \text{Eq.(3.5)}$$

Ultimately, the induced chemical attack carried out by the complex ion on the oxide layer leads to the start of pores. The depiction of the entire system may be observed in Figure 3.20 (a-e).

The chemical assault of $[TiF_6]^{2-}$ induces the formation of minuscule depressions on the oxide layer, as depicted in Figure 3.21(c). The formation of these pits can be attributed to the interaction between chemical agents and an electric field. As the anodization time progresses, the pits undergo a widening process and then transform into pores, as depicted in Figure 3.21(c). Eventually, these pores further develop into nanotubes, as illustrated in Figure 3.21(d). The production of nanotubes can be understood as a dynamic

interplay between two competing reactions: oxide synthesis and chemical etching of the oxide layer. A stable nanostructure layer is established when the rates of both processes are equivalent. The cause of a high oxidation rate resulting in a thick layer of oxide is attributed to an increased anodization voltage [145].

3.3.2 Characterization

The samples were subjected to characterization using X-Ray Powder Diffraction (XRD), Scanning Electron Microscopy (SEM), and Energy Dispersive X-ray (EDX) techniques at Bangladesh University of Engineering and Technology (BUET).

a) XRD

The crystallographic information of various anatase TiO2 samples, namely sample 2, sample 4, sample 6, sample 8, and sample 9 (consisting of pure Ti substrate), was obtained through the utilization of the X-Ray Powder Diffraction (XRD) technique. The technique employed in this study is essentially a nondestructive approach, wherein monochromatic x-rays are directed onto the sample as depicted in Figure 3.21. Monochromatic X-rays are generated using a cathode, followed by subsequent filtration and collimated intensification. The sample is subjected to focused X-ray beams. When the interactions between X-rays and a sample result in the formation of a constructive interference pattern with a diffracted ray, this phenomenon can be understood in terms of Bragg's Law.

$$n\lambda = 2d \sin \theta \qquad \text{Eq: 3.6}$$

In the context of this study, it is assumed that the variable "n" represents an integer value. Additionally, the symbol "λ" denotes the wavelength of x-ray radiation that results in the occurrence of constructive interfaces. The variable "θ" represents the incident angle, while "d" represents the lattice spacing,

which is a unique characteristic specific to each individual lattice.

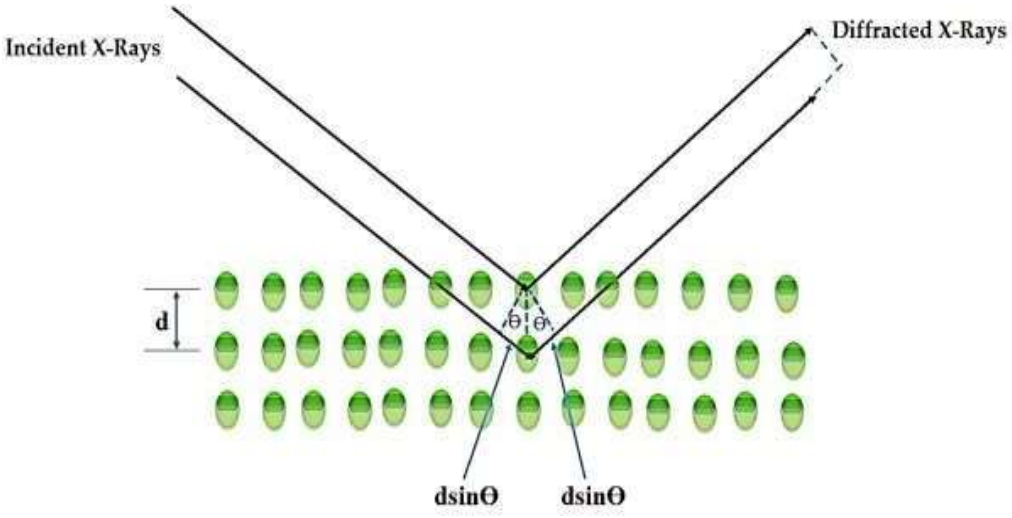

Figure 3. 21 Working principle of XRD.

Subsequently, the aforementioned x-rays are quantified, and the lattice spacing can be readily ascertained through the utilization of the prescribed equation. In order to account for the varied and disorganized arrangement of the samples, scanning is conducted at an angle of 2θ. In our analysis, we also examined the 2θ range from 10^0 to 90^0 with a step size of 0.05^o. We utilized Cu Kα radiation (Empyrean, PANalytical- Netherlands) with a wavelength of λ= 1.5406Å.

b) SEM

The scanning electron microscope (SEM) was utilized to conduct a morphological analysis of both as-prepared anodized TiO_2 and anatase TiO_2. The scanning electron microscopy (SEM) is a microscopic imaging technique that utilizes a series of focused electron beams to generate visual representations of specimens. The analysis involves the activation of high-energy, focused electron beams on the surface of the specimen. The signals obtained as a result of electron-surface interaction provided insights into various aspects of the surface, including its texture (morphology), crystalline structure, orientation, and chemical composition. In practice, when high-

energy electrons collide with the surface of the sample, they undergo deceleration, resulting in the generation of signals that consist of secondary electrons. The generation of scanning electron microscopy (SEM) images is attributed to the presence of secondary electrons, as well as backscattered electrons (BSE) and diffracted backscattered electrons (EBSD). Furthermore, the X-ray diffraction resulting from electron-electron interactions does not have any effect on volume. This technique is classified as a nondestructive testing method. The operational mechanism of the scanning electron microscope (SEM) is visually depicted in Figure 3.22. In this experiment, scanning electron microscopy (SEM) images were acquired using a JSM 7600F instrument manufactured by JEOL (Japan). The images were obtained at an accelerating voltage of 5.0 kilovolts (KV) and at various magnifications, including 5000x, 10000x, 20000x, 30000x, and 50000x.

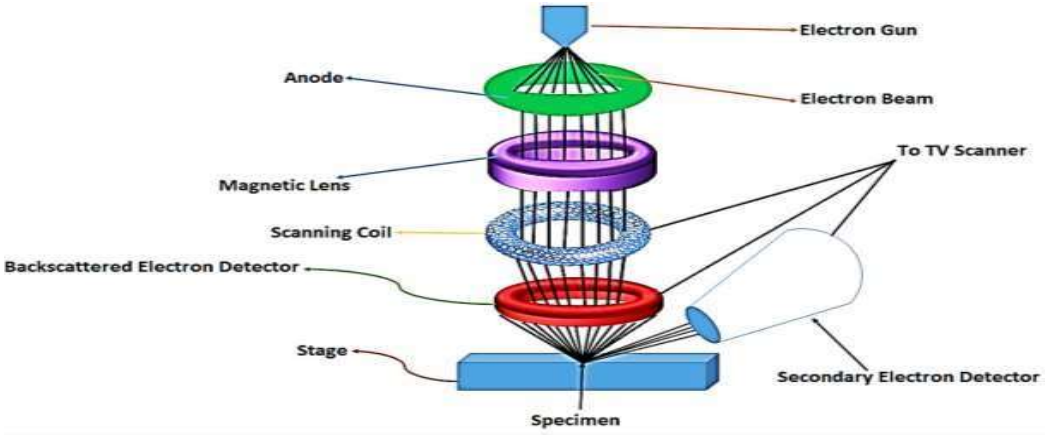

Figure 3. 22 Working Principle of SEM.

c) EDX

In Figure 3.23, the electron beam impinges upon the inner shell of an atom, resulting in the ejection of an electron from the shell. This process creates a positively charged electron hole, which is the fundamental principle underlying the functioning of EDX analysis. When an electron is displaced, it

is attracted by another electron from an outer shell to fill the resulting vacancy. The discharge of this energy difference can manifest as an X-ray emission when the electron transitions from the outer shell, characterized by higher energy levels, to the inner shell, characterized by lower energy levels, within the atom. X-ray emissions are specific to the element and its transition.

The X-rays produced during the procedure are detected by a silicon drift detector, which subsequently analyzes and interprets the signal using specialized software. Various methods can be employed to present chemical information, such as elemental mapping and line scanning. In this manner, X-ray technology can be employed for the purpose of identifying individual elements present within a given sample. EDX spectra were additionally acquired using the JSM 7600F instrument manufactured by JEOL (Japan) in this thesis. Electrons were stimulated within the energy range of 0keV to 10keV.

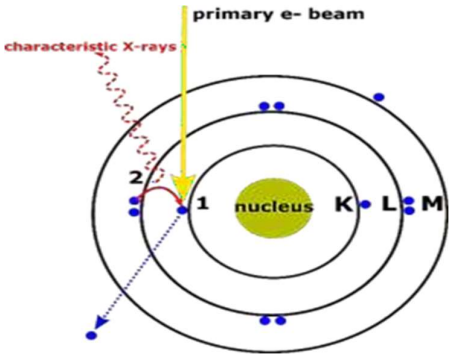

Figure 3. 23 Working Principle of EDX.

3.3.3 Coin Cell Battery Assembly

The assembly process involved the utilization of a CR2032 coin cell battery case set. The battery case comprises various components, including upper and lower cases, a spacer, and a wave spring. The anatase titanium dioxide (TiO_2) samples and the aluminum sheet coated with lithium cobalt oxide ($LiCoO_2$) were subjected to die punching with a diameter of 18 mm in order to achieve

a precise fit within the cases. The PVC separator used in battery manufacturing was also subjected to a cutting process, resulting in a reduction to a length of 20 mm, following the same procedure. Subsequently, each layer was sequentially positioned between the cases in accordance with the diagram depicted in Figure 3.24. Both sides of the separator were observed to contain small droplets of electrolyte. The electrolyte used in the experiment consisted of a 1M concentration of $LiPF_6$ dissolved in a mixture of ethylene carbonate (EC) and diethylene carbonate (DEC) at a volume ratio of 3:7. The crimping process is ultimately executed at a pressure of approximately 100 pounds per square inch (psi) utilizing a battery-powered crimping machine. This process involves the utilization of four distinct types of batteries, namely B-1 and B-2. B-3 and B-4 were constructed using sample b, sample c, sample d, and sample e, respectively.

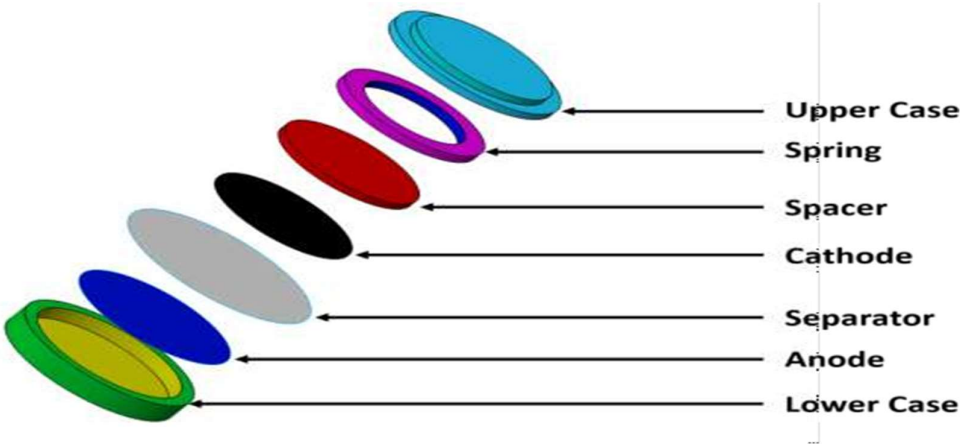

Figure 3. 24 CR2032 Coin Cell Battery Case.

3.3.4 Electrochemical Performance Test

The electrochemical performance tests were conducted using a three-step procedure. In the initial stage, an assessment was conducted on the discharge profiles of the first cycle. The charge and discharge profiles of the second, fifth, eighth, and tenth cycles for all batteries were examined. Based on the findings of these two analyses, battery has undergone deep cycling.

Chapter-04

Results and Discussions

4.1 Introduction

The selection of anode material plays a critical role in achieving optimal performance in lithium-ion batteries (LIBs). The morphological composition of its anode mostly influences the effectiveness of a lithium-ion battery (LIB). Nanomaterials have inherent advantages over bulk materials in terms of their ability to hold more charges. Furthermore, there exists a correlation between crystallinity and storage capacity. The crystal phase exhibits superior rate capability and pseudocapacitive behavior compared to the amorphous phase. As previously stated, transition metal oxides have emerged as highly viable options for serving as negative electrodes in lithium-ion batteries (LIBs). In the context of this thesis, the selection of TiO_2 as the primary emphasis is motivated by its numerous favorable characteristics.

This thesis aims to elucidate the nanotube of anatase TiO_2 via the anodization technique. Anatase has been selected as the preferred crystal phase of TiO_2 owing to its notable electrochemical reactivity when compared to other crystal phases. Four different variants of nano-structured anatase TiO_2 have been successfully produced. The many variants under consideration include the 10% (electrolyte type 1) (sample b), 20% (electrolyte type 2) (sample c), 30% (electrolyte type 2) (sample d), and 50% (electrolyte type 4) (sample e). In order to substantiate the methodology employed in this thesis, an array of analytical techniques including X-ray diffraction (XRD), scanning electron microscopy (SEM), and energy-dispersive X-ray spectroscopy (EDX) were utilized to perform comprehensive characterizations of the synthesized nanomaterials. In addition, electrochemical performance tests were conducted and briefly examined in chapter 3. The primary aims of this chapter are to

compile the results obtained from various physiological and electrochemical tests, to identify the underlying causes of different unique structures and their potential structural assessments, and to establish connections between distinct structures and their electrochemical performances in lithium-ion batteries (LIBs).

4.2 XRD Analysis

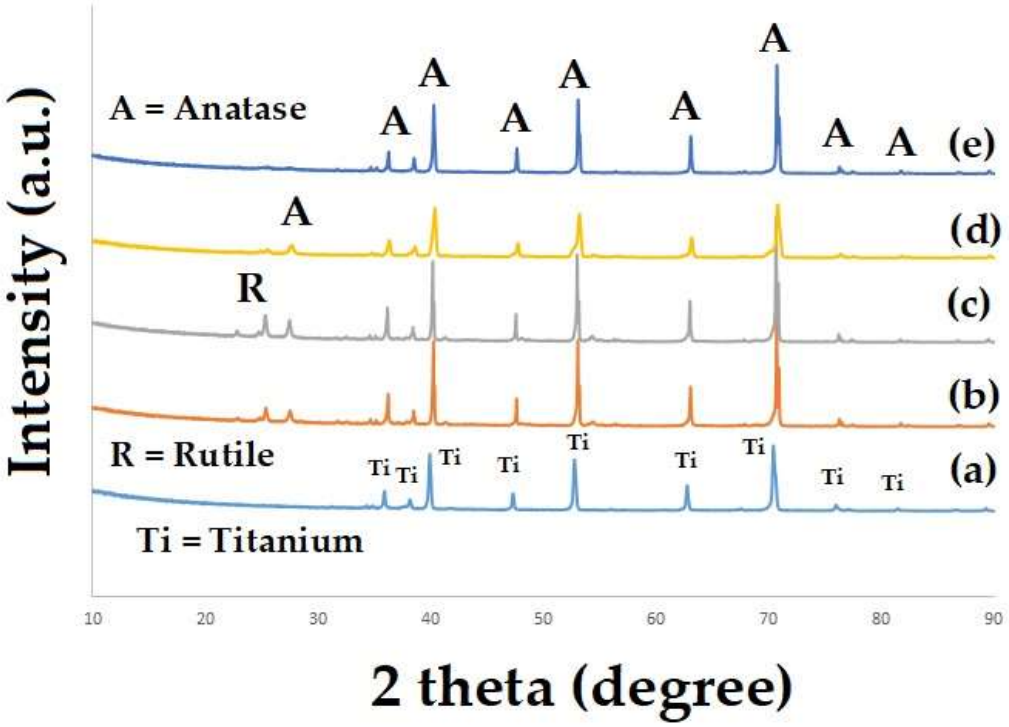

Figure 4. 1 XRD patterns of different NT-TiO_2 along with pure Ti.

The phase purity and crystallinity of Ti and different nanostructured TiO2 were examined by X-ray diffraction (XRD) technique (Fig.4.1). The crystal structure of TiO2 was tetragonal body centered from space group $I4_1/amd$ with lattice parameter a = 3.79 Å, c = 9.51 Å for sample b, sample c, sample d and sample e. These data confirm the anatase phase of TiO2. The values were also precisely matched with standard data (JCPDS Card no. 21-1272). But, more prominent peaks of anatase are observed at diffraction 2θ angles of 39.91^0 (101 plane), 52.77^0 (012 plane) and 70.419^0 (013 plane). The purity of Ti

is demonstrated by the absence of any impurity phases within the diffractometer's detection range. Furthermore, it is evident from the XRD pattern that no other diffraction peaks related to the oxide phase are seen. Ti's XRD pattern possesses strong intensity and distinct peaks.

After calcination process at 550^0C at 2 hours, three additional diffraction peaks are observed at $2\theta = 22.87^0$, 25.36^0 and 27.50^0 respectively. But as in crease the Ethylene Glycol(EG) in the solution the number of peaks are reduced and in 50% EG electrolyte these additional peaks are vanished. It means the increasing percentage of EG in the solution are hampered the anodization process. Plugging these diffraction data in following Scherrer's formula (Eq.(4.1)), we calculated the average crystal sizes for all samples shown in Table 4.1.

$$D = 0.9\times\lambda/B\cos(\theta) \qquad \text{Eq.(4.1)}$$

where,

λ = X-ray wavelength in nanometers;

B = Full width at half maximum (FWHM) of peaks at 2θ;

θ = The angle between the incident and diffracted beams in degree;

Table 4. 1 Crystal Size for all samples

Sample No	Crystallographic Data for Pure Ti										Average Crystal Size (nm)
a	2θ	35.90	38.14	39.92	47.30	52.77	62.78	70.42			38.27
	B	0.22	0.32	0.23	0.20	0.26	0.22	0.33			
	D	40.42	28.01	38.76	46.31	36.18	46.02	32.16			
	Crystallographic Data for 10% EG (Electrolyte Type 1)										
b	2θ	22.87	25.37	27.51	36.21	38.47	40.23	47.61	53.06	63.07	70.71	65.66
	B	2.07	0.36	0.44	0.16	0.16	0.10	0.10	0.09	0.13	0.09	
	D	4.21	24.39	20.09	56.26	58.35	89.19	92.14	111.45	80.33	120.18	
	Crystallographic Data for 20% EG (Electrolyte Type 2)										
c	2θ	25.30	27.48	36.16	40.18	47.57	53.01	63.01	70.67	63.07	70.71	81.06
	B	0.31	0.37	0.16	0.11	0.10	0.08	0.12	0.08	0.13	0.09	
	D	28.40	23.91	56.67	85.59	95.77	113.10	82.88	123.76	80.33	120.18	
	Crystallographic Data for 30% EG (Electrolyte Type 3)										
d	2θ	25.47	27.64	36.35	38.63	40.36	47.76	53.21	63.14	70.79	25.70
	B	1.93	0.64	0.34	0.40	0.33	0.26	0.30	0.27	0.34	
	D	4.55	13.68	26.63	22.43	27.81	36.62	31.50	37.04	31.09	
	Crystallographic Data for 50% EG (Electrolyte Type 4)										
e	2θ	36.24	38.50	40.27	47.65	53.09	63.08	70.73			59.59
	B	0.18	0.21	0.19	0.14	0.16	0.15	0.13			
	D	51.22	42.90	46.98	67.13	61.41	66.44	81.03			

4.3 SEM & EDX Analysis

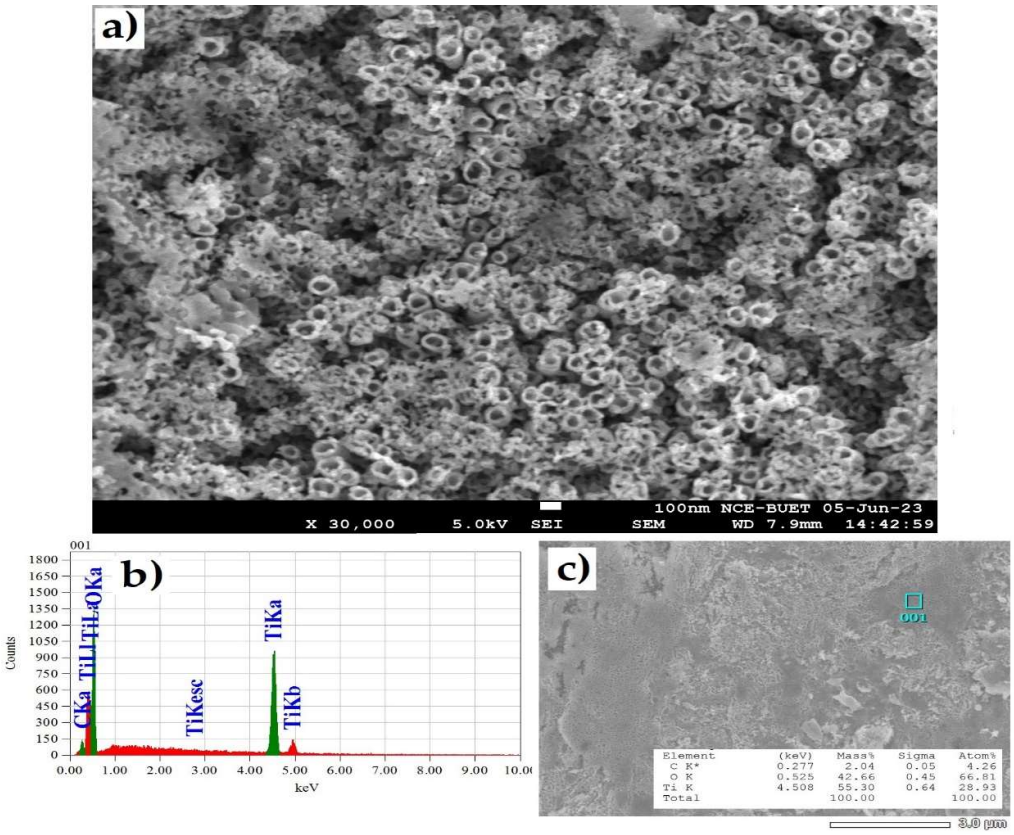

Figure 4. 2 High magnification SEM image and EDX spectra of I (10% EG electrolyte Type 1).

The plan-view SEM images and EDX spectra of NT-TiO2 prepared in different electrolytes for 2h and after calcination at 550^0C for 2h has been shown in different figures. Non-uniform NT-TiO_2 arrays were grown by anodization in all four different electrolyte solutions, and all the NT-TiO_2 arrays were observed clearly underneath the Ti substrates. Different structured were observed on the electrode surfaces that were anodized in electrolytes containing 10 vol%, 20 vol%, 30 vol% & 50% of EG in Fig.4.2, Fig.4.3, Fig.4.4 & Fig.4.5 respectively.

In Fig.4.2 (a), the electrochemical anodization of titanium at 10% EG electrolyte type 1 leads to the formation of an ordered nanotubular array on

the titanium surface. The nanotubes are compact in this area. For the elemental characterization of the obtained nanotube layers, energy dispersive X-ray analysis is conducted using an acceleration voltage of 10 kV. The characteristics of the emitted X-rays from the anodized subtrate produced at different condition are presented in the figure 4.2 (b-c). The EDX spectrum indicates the presence of the TiKa peak at 4.508 keV and O peaks at 0.525 keV as well as C peak at 0.277 keV in the anodized sample. The obtained mass percentages of Ti is 55.30% and O is 42.44% and atom percentage of Ti, O & C is 28.93%, 66.81% & 4.26%. In this analysis, another peak of carbon is found at 0.277 keV with the percentage of C is 2.04%.

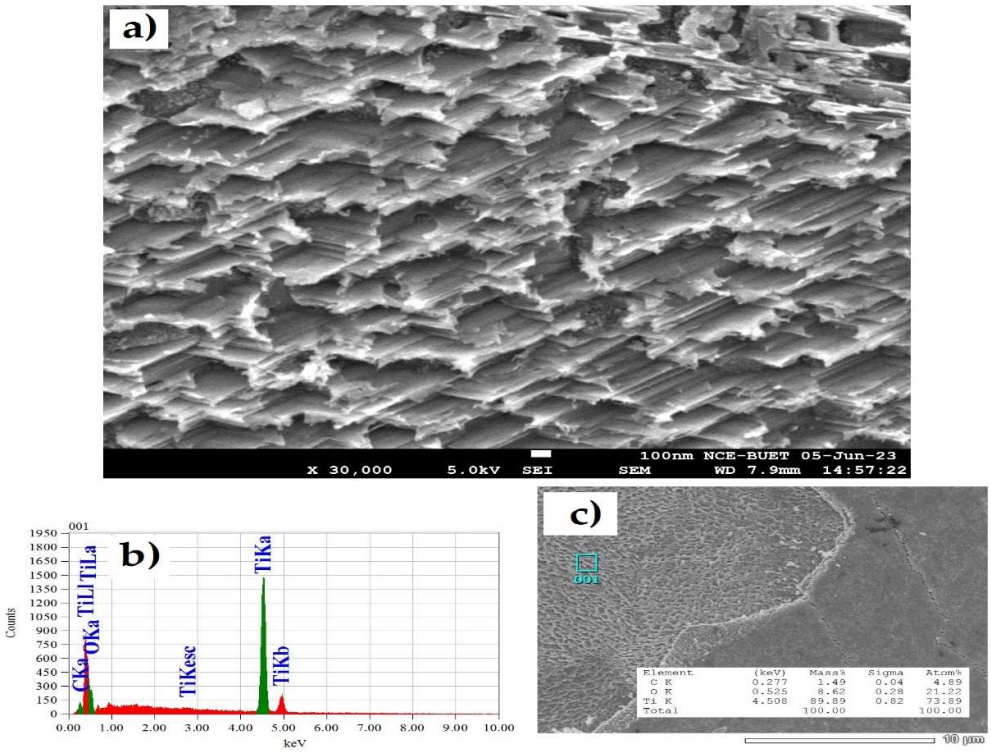

Figure 4. 3 High magnification SEM image and EDX spectra of (20% EG electrolyte Type 2)

On the contrary, earth crust like textures was appeared in the figure 4.3 (a). The EDX spectrum indicates the TiKa peaks at 4.508 keV, O peaks at 0.525

keV and C peak at 0.277 keV with the mass and atom percentages of Ti, O & C are 89.89%, 8.62% & 1.49% and 73.89%, 21.22% & 4.89% respectively shown in figure 4.3 (b-c).

In contrast, the image 4.4 (a) depicted the presence of textures resembling those found in the Mars surface. The energy-dispersive X-ray (EDX) spectrum reveals the presence of peaks corresponding to titanium (TiKa) at 4.508 keV, oxygen (O) at 0.525 keV, and carbon (C) at 0.277 keV. The mass and atom percentages of Ti, O & C are reported as 63.81%, 34.38% & 1.81% and 36.68%, 59.17% & 4.16% respectively. These values are depicted in figure 4.4 (b-c).

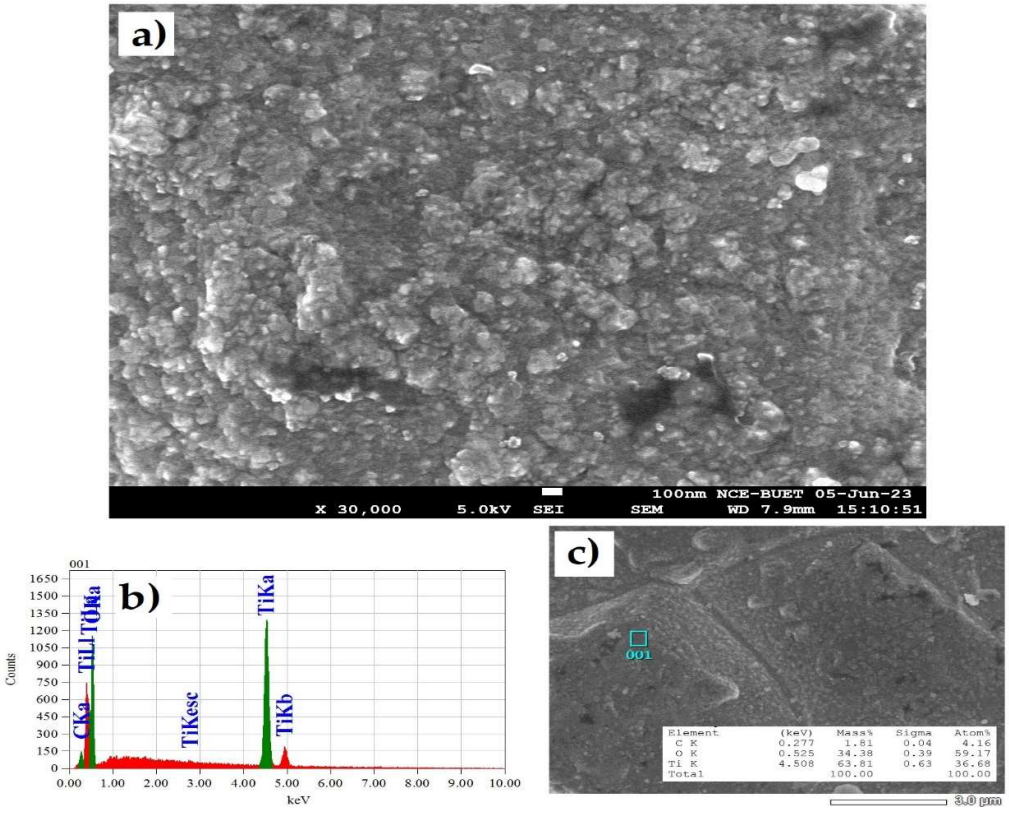

Figure 4. 4 High magnification SEM image and EDX spectra of (30% EG electrolyte Type 3)

On the other hand, image 4.5 (a) exhibited the existence of textures that bear resemblance to those observed on sand surface. The energy-dispersive X-ray (EDX) spectrum exhibits discernible peaks that correspond to titanium (TiKa) at 4.508 keV, oxygen (O) at 0.525 keV, and carbon (C) at 0.277 keV. The indicated values can be observed in Figure 4.5 (b-c).

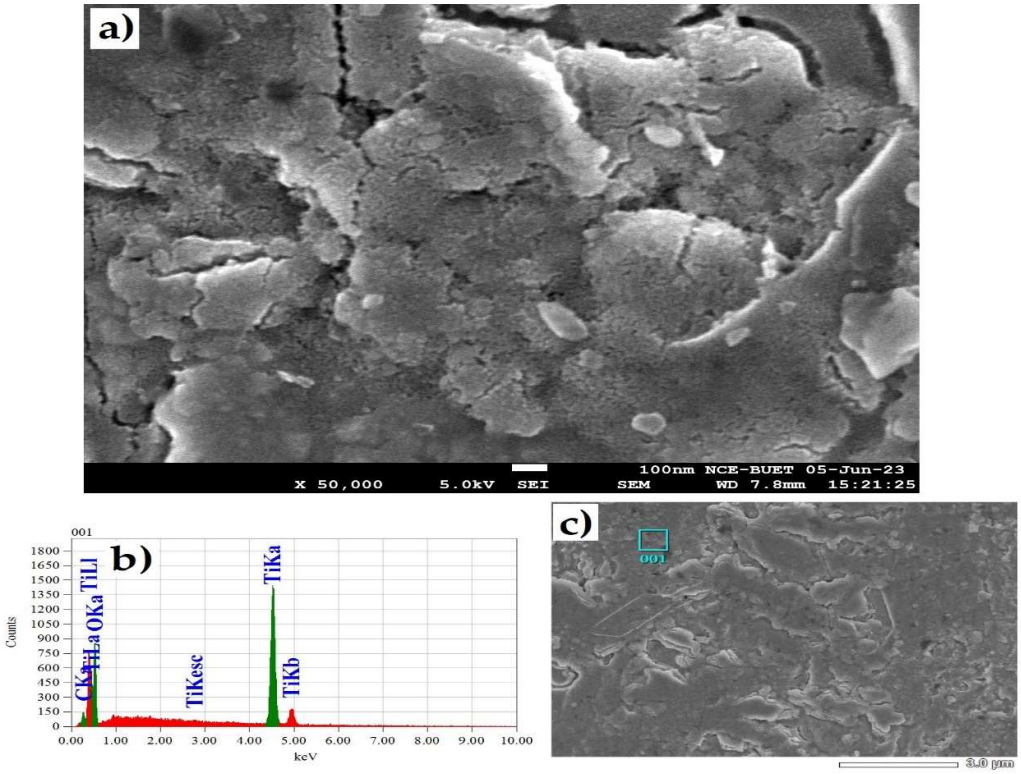

Figure 4. 5 High magnification SEM image and EDX spectra of (50% EG electrolyte Type 4)

From the above, it is clear that the nanotube is formed only in the 10%EG Electrolyte Type 1. So, battery is assembled only from 10% EG Electrolyte Type 1 sample and electrochemical performance is measured further.

4.4 Electrochemical analysis of Anatase TiO2 Nanotubes as anode of LIBs:

The galvanostatic charge-discharge cycle is carried out to measure the electrochemical performance of the as-prepared anatase TiO_2 nanotubes anode.

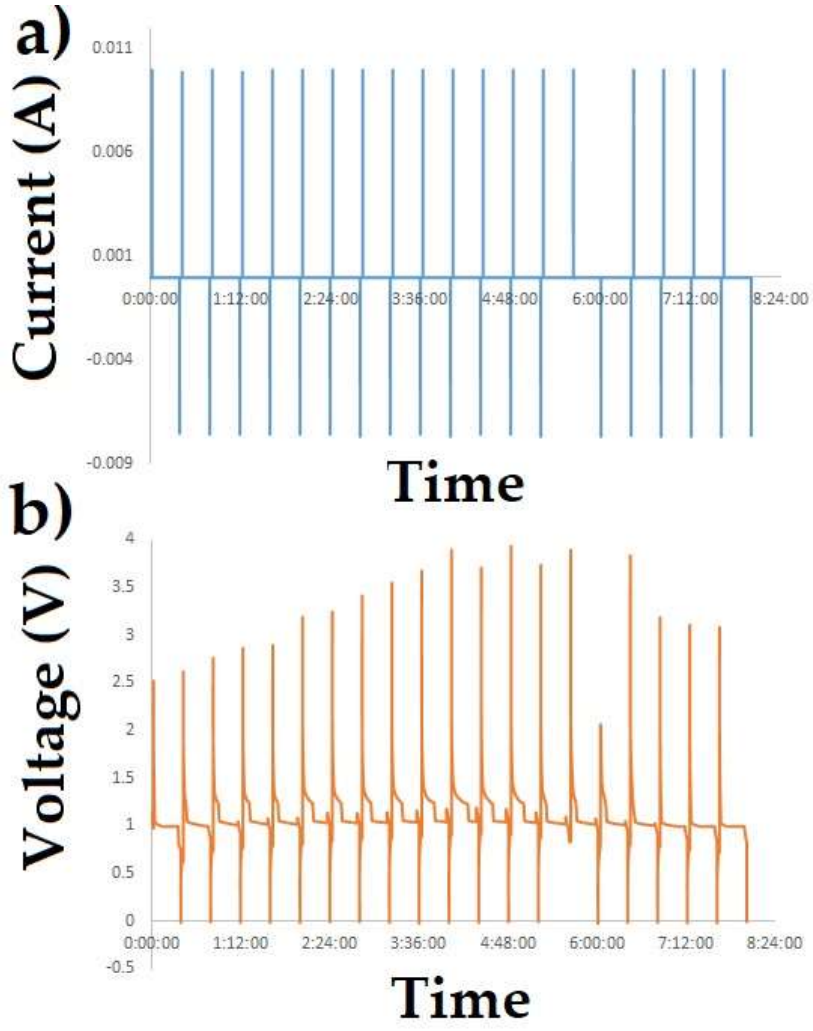

Figure 4. 6 Change of Current and Voltage with respect to time from 1-20 Charge-Discharge cycles.

Figures 4.6 and 4.7 show the changes in current and voltage with respect to time. The cut-off voltage ranges are -4V-3.8V. From figure 4.6, it is shown that at the beginning of the cycling, the voltages remain 2.5V. However, as the

cycling moves forward, the voltage increased, and after 20th cycle the voltage is decreased.

On the other hand, in figure 4.7 from the voltage & current both are increased and at the end of the 40th cycle of the charge-discharge process, the voltage is found to be 4.2V.

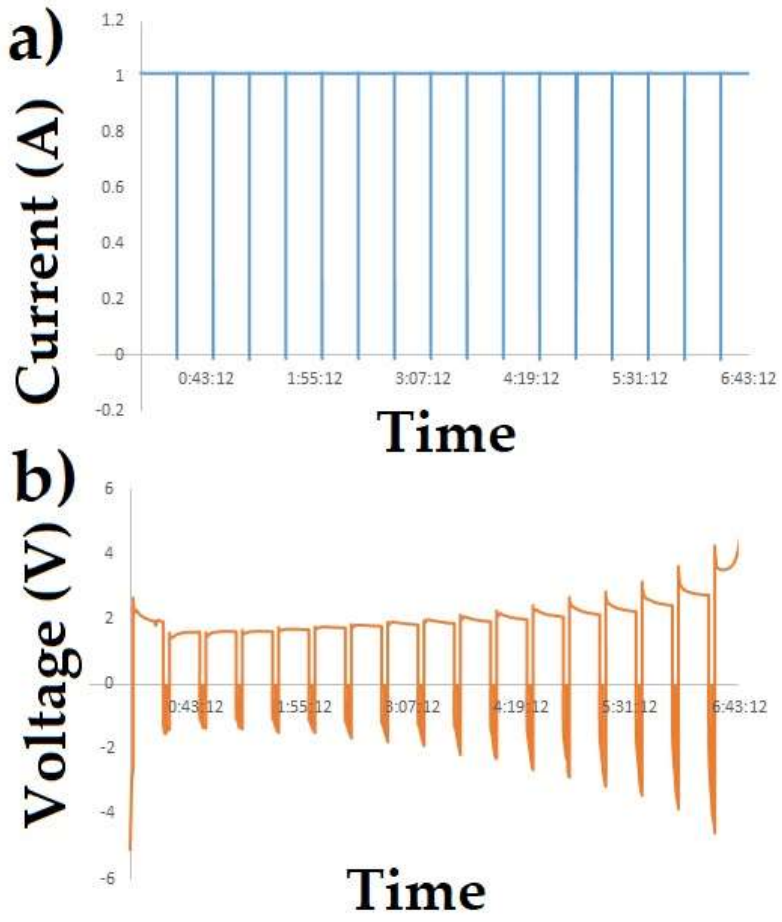

Figure 4. 7 Change of Current and Voltage with respect to Time from 21-40 Charge-Discharge cycles.

One of the most important analyses carried out to forecast cell failure is differential capacity analysis. Figure 4.8 depicts a variation of dQ/dV with V up to 40 charge-discharge cycles. From Figure 4.8 it's evident that from 21 cycles the cell gradually starts to fail.

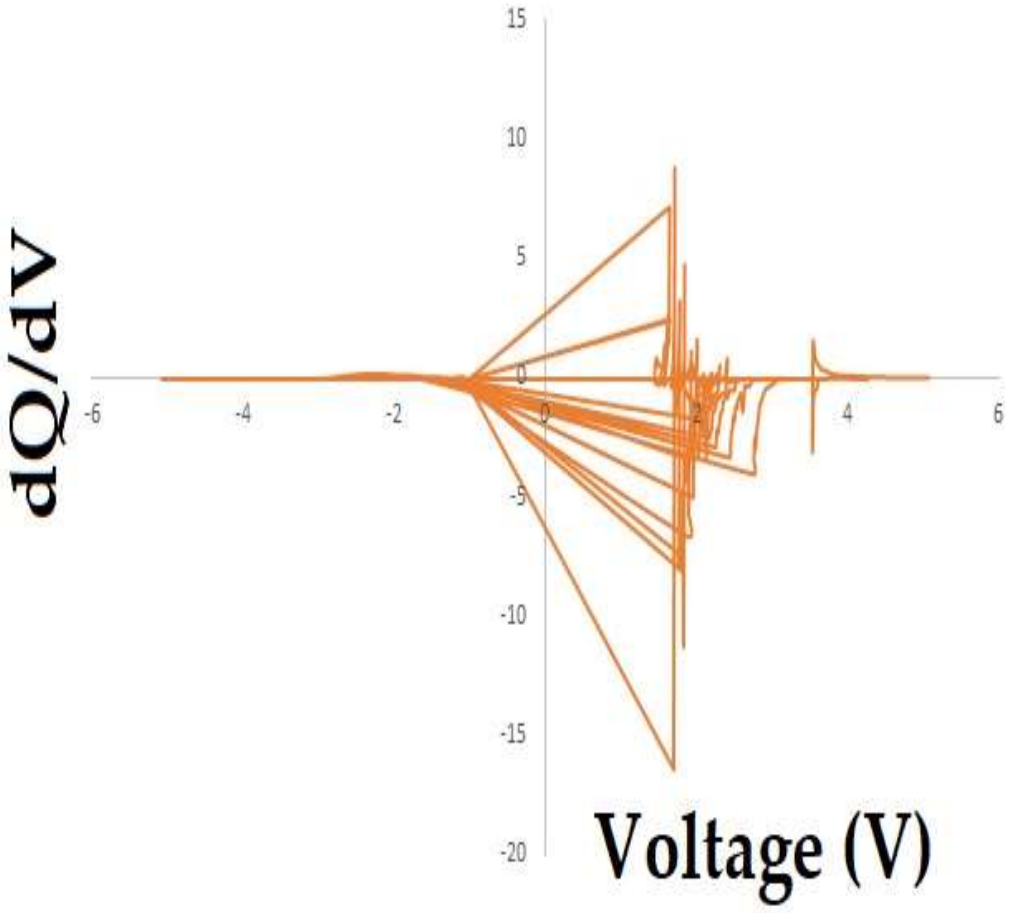

Figure 4. 8 Change of dQ/dV with respect to voltage from 01-40 cycles.

The actual electrochemical performance of the LIB is shown in different figures, whereas the prepared anatase TiO_2 nanotubes disc is used as an anode.

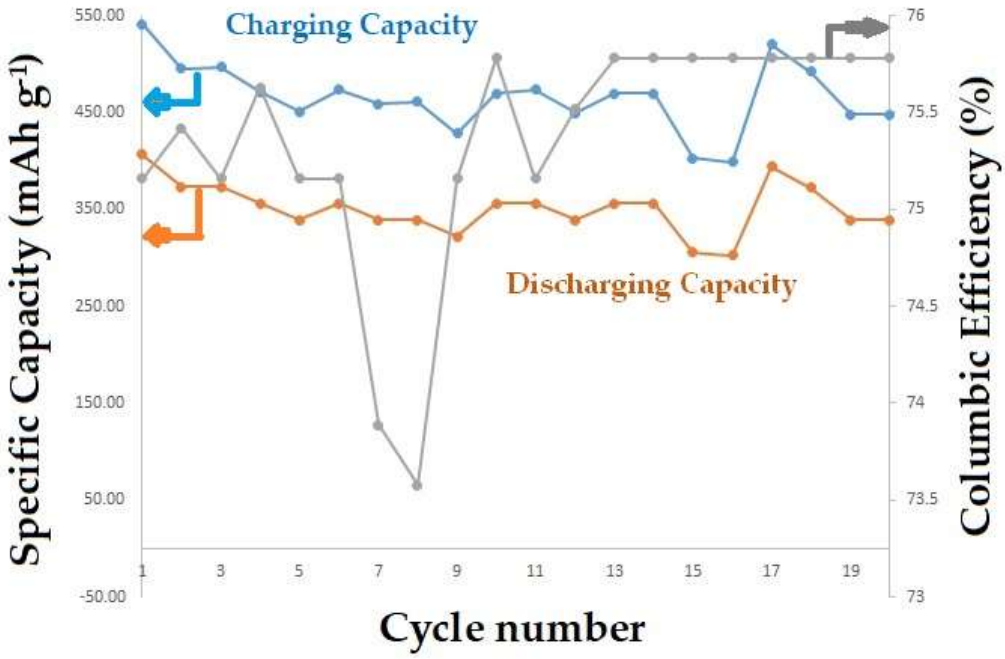

Figure 4. 9 Change of Specific capacity and columbic efficiency during 01-20 charge-discharge cycles with 1C current rating.

Figure 4.9 depicts the variation of specific capacity and columbic efficiency with 1-20 galvanostatic charge-discharge cycles Figure 4.10 shows the variation of specific capacity and columbic efficiency with 21-40 galvanostatic charge-discharge cycles.

First cycle charge-discharge capacities are 550 $mAhg^{-1}$ and 400 $mAhg^{-1}$, respectively, with columbic efficiency 75.75%. Higher initial capacities are ascribed to gel-like SEI layer formation by electrolyte decomposition. The low columbic efficiency is attributed to unstable SEI formation, low reversible capacity, and electrolyte decomposition. However, in the subsequent 2nd cycle, the charge-discharge capacity drastically reduced to 500 mAhg-1 and 360 mAhg-1, respectively, due to the amorphous Li_2O formation, which

required a huge amount of lithium and caused the loss of lithium [241]. The increased columbic efficiency of 75.4% in the 2nd cycle is attributed to stable SEI layer formation. However, the cell shows instability with fluctuating columbic efficiency attributed to the larger volume expansion and pulverization effect of the anode. At 27th cycle the columbic efficiency is as high as 120%. This phenomenon is typical for transition metal oxide, popularly known as pseudo capacitance. At 40th cycle, charge-discharge capacities are found to be 375 $mAhg^{-1}$ and 325 $mAhg^{-1}$, respectively, and at this cycle, the columbic efficiency is 80%

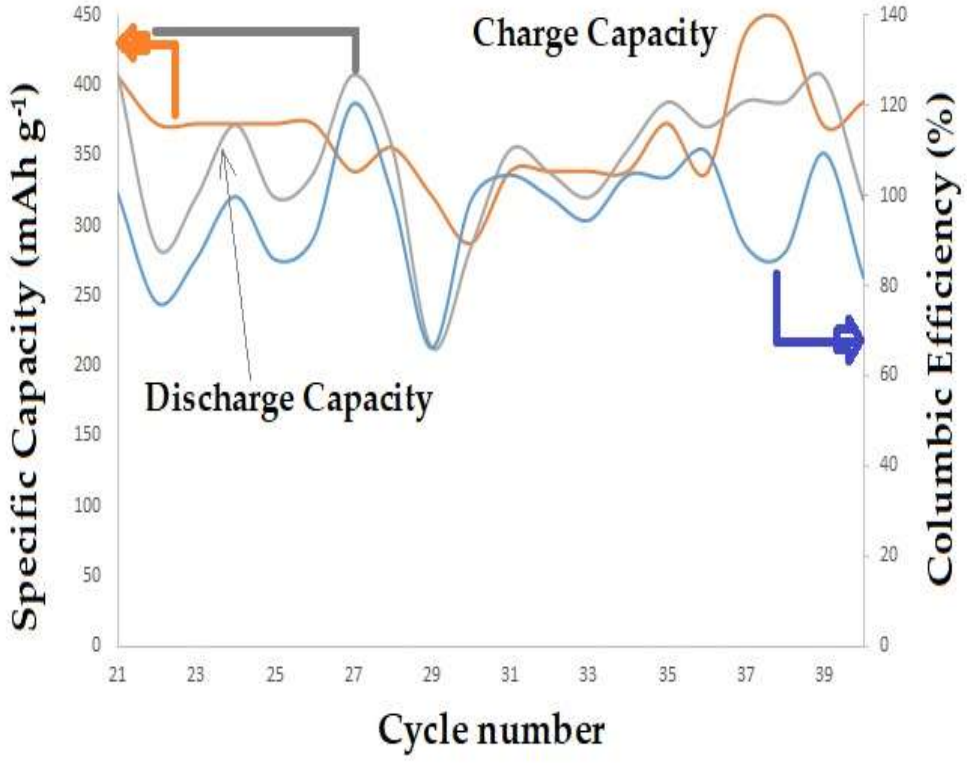

Figure 4. 10 Change of specific capacity and columbic efficiency during 21-40 charge-discharge cycles with 1C current rating.

4.5 Photo Activity Test

The photocatalytic activity of anatase TiO_2 nanostructure anode sheet was measured using methylene blue (MB) dye solutions. The material is shown the photo activity behavior. The findings indicate that higher concentrations of ethylene glycol do not result in a corresponding rise in photocatalytic activity. The blank sample also exhibited photocatalytic activity but showed very low dye degradation (46%) in 4 hours (Figure 5.3.1-5.3.2). This result confirms that the nanostructured anatase TiO2 sheet was successfully fabricated and demonstrated excellent methylene blue degradation.

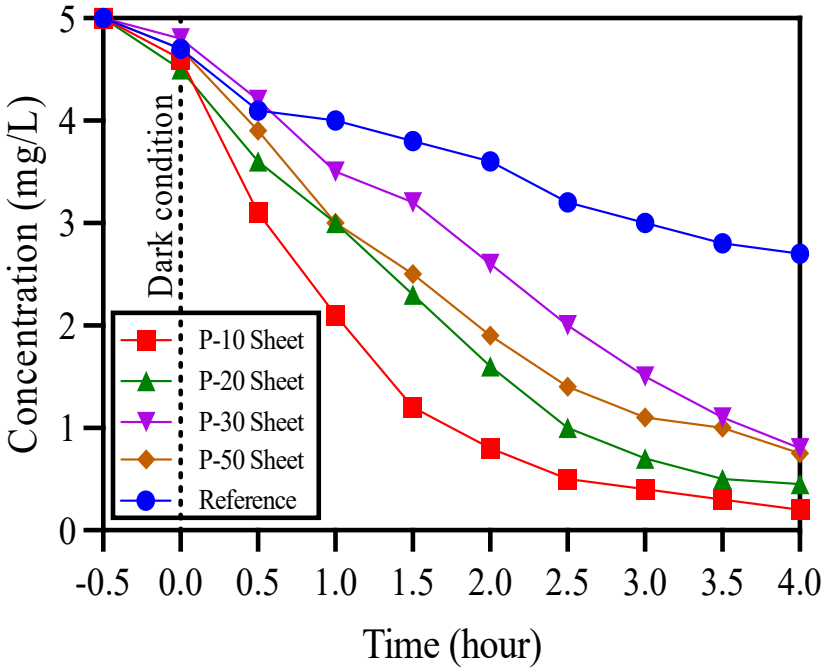

Figure 4. 11 The photocatalytic degradation of MB dye by using different types of anatase TiO2 nanotube anode sheets.

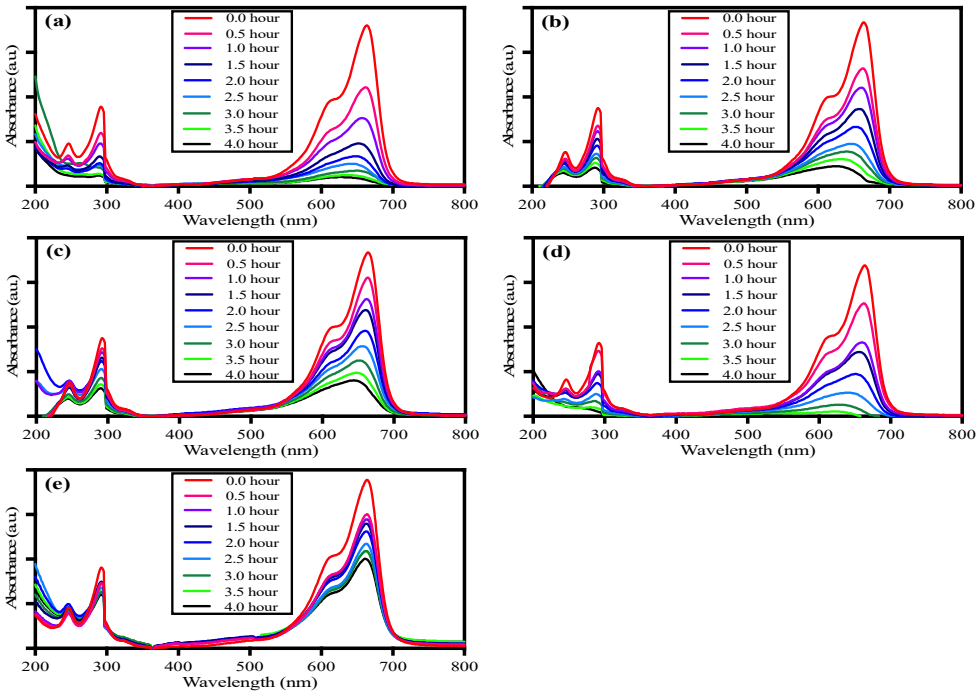

Figure 4. 12 The absorption spectra of MB dye solution on (a) 10% EG electrolyte Type 1, (b) 20% EG electrolyte Type 2, (c) 30% EG electrolyte Type 3, (d) 50% EG electrolyte Type 4 at various times of sunlight irradiation.

So, this material is also used for energy harvesting research purpose. It is a dual functional material.

4.6 Comparison of our works with previous 1D Anatase TiO_2 Study

The comparison between our work with previous work is given below:

Table 4. 2 Comparison of our work with previous work

Compare	Cycle No.	Unit	Our Work	Previous Work	Reference Number
Charge Capacity	1st	$mAhg^{-1}$	550	290	[305]
Discharge Capacity		$mAhg^{-1}$	400	239	
Columbic Efficiency		%	75	82	
Charge Capacity	Last	$mAhg^{-1}$	375	238	[305]
Discharge Capacity		$mAhg^{-1}$	325	198	
Columbic Efficiency		%	80	98	

In the comparison it is noted that, for our work, last cycle is 40th cycle and previous work, last cycle is 20th cycle.

4.7 Summary

In this chapter, after the anodization and calcination process, the nanotube of anatase TiO_2 is found in the 10% EG Electrolyte Type 1. The surface morphology and electrochemical performance of the as-prepared anode are also evaluated. The battery exhibits excellent charge-discharge capacity of, of 550 mAhg-1 and 400 mAhg-1 respectively with 75.25%. At 40th cycle, 375 $mAhg^{-1}$ and 325 $mAhg^{-1}$ with 80% columbic efficiency of charge-discharge capabilities were discovered. This effect, also known as pseudo capacitance, is typical of transition metal oxide.

Chapter-05

Conclusion and Further Study

5.1 Conclusion

This thesis represents a facile fabrication of nanotube anatase TiO_2 (NT-TiO_2) via electrochemical anodization by different percentage of EG in of Ti foils (99% pure) by different percentage of EG in the electrolyte. After that at 550^0C for 2h calcination is performed. Four different types of distinct geometry have been appeared. After surface morphology analysis, the anatase TiO_2 nanotube is found in the 10% EG electrolyte Type 1. The battery is assembled only for 10% EG electrolyte Type 1 (sample b). Assessments of these NT-TiO_2 products as anode showed propitious outcomes. They provide high surface area which allow higher electrode/electrolyte interface. As consequence, lithium storage capacity has greatly enhanced than bulk amorphous TiO_2. The improvement in storage capacities, rate performances and cyclabilities were in different extents for four various batteries. Several outcomes are enumerated below:

- The cut-off voltage ranges are -4V-3.8V. It is shown that at the beginning of the cycling, the voltages remain 2.5V. However, as the cycling moves forward, the voltage increased, and at the end of the 40th cycle of the charge-discharge process, the voltage is found to be 4.2V.
- From 21 cycles the cell gradually starts to fail.
- The battery exhibits excellent charge-discharge capacity of 550 $mAhg^{-1}$ and 400 $mAhg^{-1}$ respectively with 75.75% columbic efficiency.
- At 27th cycle the columbic efficiency is as high as 120%. This phenomenon is typical for transition metal oxide, popularly known as pseudo capacitance.

- At 40th cycle, charge-discharge capacities are found to be 375 $mAhg^{-1}$ and 325 $mAhg^{-1}$, respectively, and at this cycle, the columbic efficiency is 80%

5.2 Limitations

This study focuses on the fabrication and thorough analysis of a high-capacity anode. However, it is essential to note that certain limits were found in this investigation. The limitations of this study are as follows:

- The cathode material utilized in our thesis consisted of $LiCoO_2$ sheets, which were procured from China. The voltage of the produced lithium-ion battery system (LIBS) decreased due to a decrease in the quantity of active components present on the sheet.
- The thermal oxidation furnace employed in the experiment exhibited signs of aging, resulting in a less than optimal temperature control. Furthermore, the occurrence of abrupt power outages further impeded the consistent oxidation process.
- The electrolyte used in the study was $LiPF_6$ which is photosensitive and volatile in nature. In an open environment, the electrolyte decomposes easily. Handling the electrolyte in an open environment was one of the major challenges of this study.

- For assembly and testing, a moisture-free atmosphere is necessary for lithium-ion batteries (LIBs). The highest quality LIB is produced in a highly regulated, moisture-free environment in an inert atmosphere glovebox system. Due to a lack of a glove box facility in our lab, we were unable to construct LIB in a moisture-free environment, which had an adverse influence on the battery's electrochemical performance.

5.3 Further Study

In this work, the fabrication of NT-TiO_2 was conducted through the utilization of an anodization procedure. The interior texture of nanotubes is significantly influenced by several parameters during the process of anodization. These parameters encompass the applied voltage, time, temperature, electrolyte composition, agitation, and the surface state of both the cathode and anode. The dimensions and shape of nanotubes can be adjusted by modifying these factors. Several significant improvements and points should be considered for future pursuit of this thesis work. They are:

- In electrolyte the percentages of Ethylene Glycol can be increased. The other contents ratio like 1M $(NH_4)_2SO_4$, 0.5 wt% NH_4F can be altered.
- Applied voltage can be altered.
- Anodization period can be varied. Long duration is suggested be applied in presence of EG.
- Surface of Ti foils can be annealed before anodization.
- Battery performance analysis can be carried at low and higher current rate like 0.1C, 0.25C, 2C, 3C etc. for gather more deep insight in performance evaluation.

References

1. IEA, *World Energy Outlook 2022*. 2022, IEA, Paris, France.
2. Yang, Z., et al., *Electrochemical energy storage for green grid.* Chemical reviews, 2011. **111**(5): p. 3577-3613.
3. IEA (2019), G.E.C.S.R., IEA, Paris https://www.iea.org/reports/global-energy-co2-status-report-2019, License: CC BY 4.0. *Global Energy & CO2 Status Report 2019*. 2019; Available from: https://www.iea.org/reports/global-energy-co2-status-report-2019/electricity.
4. Roberts, P., *The end of oil: on the edge of a perilous new world*. 2005: Houghton Mifflin Harcourt.
5. Powell, C.A. and B.D. Morreale, *Materials challenges in advanced coal conversion technologies.* Mrs Bulletin, 2008. **33**(4): p. 309-315.
6. Arunachalam, V. and E. Fleischer, *The global energy landscape and materials innovation.* MRS bulletin, 2008. **33**(4): p. 264-288.
7. Meier, P.J., et al., *US electric industry response to carbon constraint: a life-cycle assessment of supply side alternatives.* Energy Policy, 2005. **33**(9): p. 1099-1108.
8. Ersoy, E., M.E. Schaffer, and J. Ditzen, *BP statistical review of world energy 2019.* 2019.
9. Programme, U.N.D., *World energy assessment: Energy and the challenge of sustainability*. 2000: UNDP.
10. Ginley, D., M.A. Green, and R. Collins, *Solar energy conversion toward 1 terawatt.* MRS bulletin, 2008. **33**: p. 355-364.
11. Holdren, J.P., *Energy and sustainability*. 2007, American Association for the Advancement of Science. p. 737-737.
12. Pool, R., *In depth storage-analysis-climate change stirs storage industry.* Power Engineer, 2007. **21**(3): p. 10-11.
13. Lee, B.S. and D.E. Gushee, *Electricity storage: The Achilles' heel of renewable energy.* Chemical Engineering Progress, 2008. **104**(3): p. S29-S32.
14. Energy, U.S.D.o. *Smart Grid System Report*. 2009; Available from: https://www.energy.gov/sites/prod/files/2009%20Smart%20Grid%20System%20Report.pdf.
15. Chang, L., et al., *Review on distributed energy storage systems for utility applications.* CPSS Transactions on Power Electronics and Applications, 2017. **2**(4): p. 267-276.
16. Amrouche, S.O., et al., *Overview of energy storage in renewable energy systems.* International journal of hydrogen energy, 2016. **41**(45): p. 20914-20927.
17. Alva, G., Y. Lin, and G. Fang, *An overview of thermal energy storage systems.* Energy, 2018. **144**: p. 341-378.
18. Rahman, M.M., et al., *Assessment of energy storage technologies: A review.* Energy Conversion and Management, 2020. **223**: p. 113295.
19. Oudalov, A., D. Chartouni, and C. Ohler, *Optimizing a battery energy storage system for primary frequency control.* IEEE Transactions on power systems, 2007. **22**(3): p. 1259-1266.
20. Yang, Y., et al., *Battery energy storage system size determination in renewable energy systems: A review.* Renewable and Sustainable Energy Reviews, 2018. **91**: p. 109-125.
21. Lawder, M.T., et al., *Battery energy storage system (BESS) and battery management system (BMS) for grid-scale applications.* Proceedings of the IEEE, 2014. **102**(6): p. 1014-1030.

22. Duan, X., et al., *Analysis of winding vibration characteristics of power transformers based on the finite-element method.* Energies, 2018. **11**(9): p. 2404.
23. Divya, K. and J. Østergaard, *Battery energy storage technology for power systems—An overview.* Electric power systems research, 2009. **79**(4): p. 511-520.
24. Alharbi, H. and K. Bhattacharya. *Optimal sizing of battery energy storage systems for microgrids*. in *2014 IEEE Electrical Power and Energy Conference*. 2014. IEEE.
25. Murty, V. and A. Kumar, *RETRACTED ARTICLE: Multi-objective energy management in microgrids with hybrid energy sources and battery energy storage systems.* Protection and Control of Modern Power Systems, 2020. **5**(1): p. 1-20.
26. Hill, C.A., et al., *Battery energy storage for enabling integration of distributed solar power generation.* IEEE Transactions on smart grid, 2012. **3**(2): p. 850-857.
27. Abbott, M. and B. Cohen, *Issues associated with the possible contribution of battery energy storage in ensuring a stable electricity system.* The Electricity Journal, 2020. **33**(6): p. 106771.
28. Reddy, T.B., *Linden's handbook of batteries*. 2011: McGraw-Hill Education.
29. Sobianowska-Turek, A., et al., *Non-reductive acidic leaching as a method for recovery of zinc and manganese from Zn-C and Zn-MnO2 battery waste.* Environment Protection Engineering, 2021. **47**(2).
30. Farrell, T.W., et al., *Primary Alkaline Battery Cathodes A Three-Scale Model.* Journal of the Electrochemical Society, 2000. **147**(11): p. 4034.
31. Lisbona, D. and T. Snee, *A review of hazards associated with primary lithium and lithium-ion batteries.* Process safety and environmental protection, 2011. **89**(6): p. 434-442.
32. Fleischer, A. and J.J. Lander, *Zinc-silver oxide batteries*. 1971, Air Force Aero Propulsion Lab Wright-patterson Afb Ohio.
33. Caramia, V. and B. Bozzini, *Materials science aspects of zinc–air batteries: a review.* Materials for Renewable and Sustainable Energy, 2014. **3**: p. 1-12.
34. Watanabe, K., T. Kikuoka, and N. Kumagai, *Physical and electrochemical characteristics of nickel hydroxide as a positive material for rechargeable alkaline batteries.* Journal of applied electrochemistry, 1995. **25**: p. 219-226.
35. Lacerda, V.G., et al., *Separation of Cd and Ni from Ni–Cd batteries by an environmentally safe methodology employing aqueous two-phase systems.* Journal of Power Sources, 2009. **193**(2): p. 908-913.
36. Serrao, L., et al. *An aging model of Ni-MH batteries for hybrid electric vehicles*. in *2005 IEEE Vehicle Power and Propulsion Conference*. 2005. IEEE.
37. Liu, Y., et al., *Advanced hydrogen storage alloys for Ni/MH rechargeable batteries.* Journal of Materials Chemistry, 2011. **21**(13): p. 4743-4755.
38. Bode, H., *Lead-acid batteries.* 1977.
39. Manwell, J.F. and J.G. McGowan, *Lead acid battery storage model for hybrid energy systems.* Solar energy, 1993. **50**(5): p. 399-405.
40. Jiao, H., et al., *A rechargeable Al–Te battery.* ACS Applied Energy Materials, 2018. **1**(9): p. 4924-4930.
41. Gao, T., et al., *A rechargeable Al/S battery with an ionic-liquid electrolyte.* Angewandte Chemie International Edition, 2016. **55**(34): p. 9898-9901.
42. Song, Y., et al., *A long-life rechargeable Al ion battery based on molten salts.* Journal of Materials Chemistry A, 2017. **5**(3): p. 1282-1291.
43. Wang, M., et al., *Reversible calcium alloying enables a practical room-temperature rechargeable calcium-ion battery with a high discharge voltage.* Nature chemistry, 2018. **10**(6): p. 667-672.

44. Shimizu, Y., et al., *Bi-Functional Oxygen Electrode Using Large Surface Area La1− x Ca x CoO3 for Rechargeable Metal-Air Battery.* Journal of The Electrochemical Society, 1990. **137**(11): p. 3430.
45. Choi, J.W. and D. Aurbach, *Promise and reality of post-lithium-ion batteries with high energy densities.* Nature Reviews Materials, 2016. **1**(4): p. 1-16.
46. Zhang, J., et al., *Carbon science in 2016: Status, challenges and perspectives.* Carbon, 2016. **98**(70): p. 708-732.
47. Rodrigues, M.-T.F., et al., *A materials perspective on Li-ion batteries at extreme temperatures.* nature energy, 2017. **2**(8): p. 1-14.
48. Yang, Z., et al., *Nanostructures and lithium electrochemical reactivity of lithium titanites and titanium oxides: A review.* Journal of Power Sources, 2009. **192**(2): p. 588-598.
49. Jabbour, L., et al., *Cellulose-based Li-ion batteries: a review.* Cellulose, 2013. **20**: p. 1523-1545.
50. Arfwedson, A., *Untersuchung einiger bei der Eisen-Grube von Utö vorkommenden Fossilien und von einem darin gefundenen neuen feuerfesten Alkali.* J. Chem. Phys, 1818. **22**: p. 93-117.
51. Berzelius, J.J., *Ein neues mineralisches Alkali und ein neues Metall.* J. Chem. Phys, 1817. **21**: p. 44-48.
52. Reddy, M.V., et al., *Brief history of early lithium-battery development.* Materials, 2020. **13**(8): p. 1884.
53. Lewis, G.N. and F.G. Keyes, *THE POTENTIAL OF THE LITHIUM ELECTRODE.* Journal of the American Chemical Society, 1913. **35**(4): p. 340-344.
54. Whittingham, M.S., *Electrical energy storage and intercalation chemistry.* Science, 1976. **192**(4244): p. 1126-1127.
55. Tarascon, J.-M. and M. Armand, *Issues and challenges facing rechargeable lithium batteries.* nature, 2001. **414**(6861): p. 359-367.
56. Touzain, P., R. Yazami, and J. Maire, *Insertion compounds of graphite with improved performances and electrochemical applications of those compounds*. 1986, Google Patents.
57. Bredas, J.-L., et al., *An electrifying choice for the 2019 chemistry Nobel Prize: Goodenough, Whittingham, and Yoshino*. 2019, ACS Publications. p. 8577-8581.
58. Liu, Y., et al., *Solder-free electrical Joule welding of macroscopic graphene assemblies.* Materials Today Nano, 2018. **3**: p. 1-8.
59. Thackeray, M.M., C. Wolverton, and E.D. Isaacs, *Electrical energy storage for transportation—approaching the limits of, and going beyond, lithium-ion batteries.* Energy & Environmental Science, 2012. **5**(7): p. 7854-7863.
60. Yao, F. and C.S. Cojocaru, *Carbon-based nanomaterials as an anode for lithium ion battery*. 2013, Ecole Polytechnique X.
61. Shimadzu, *Rechargeable Lithium-Ion Battery.*
62. Ehrlich, G.M., *Lithium-ion batteries.* Handbook of batteries, 2002. **3**: p. 35.2-35.94.
63. Ozawa, K., *Lithium-ion rechargeable batteries with LiCoO2 and carbon electrodes: the LiCoO2/C system.* Solid State Ionics, 1994. **69**(3-4): p. 212-221.
64. Amanor-Boadu, J.M., A. Guiseppi-Elie, and E. Sánchez-Sinencio, *Search for optimal pulse charging parameters for Li-ion polymer batteries using Taguchi orthogonal arrays.* IEEE Transactions on Industrial Electronics, 2018. **65**(11): p. 8982-8992.
65. Jeon, H., et al. *Aqueous Ceramic Coating upon Hydrophobic Polyethylene Lithium-Ion Battery Separators through Use of an Anionic Surfactant*. in *Electrochemical Society Meeting Abstracts 229*. 2016. The Electrochemical Society, Inc.
66. Nitta, N., et al., *Li-ion battery materials: present and future.* Materials today, 2015. **18**(5): p. 252-264.

67. Pistoia, G., *Lithium-ion batteries: advances and applications.* 2013.
68. Scrosati, B., J. Hassoun, and Y.-K. Sun, *Lithium-ion batteries. A look into the future.* Energy & Environmental Science, 2011. **4**(9): p. 3287-3295.
69. Yi, T.-F., S.-Y. Yang, and Y. Xie, *Recent advances of Li 4 Ti 5 O 12 as a promising next generation anode material for high power lithium-ion batteries.* Journal of Materials Chemistry A, 2015. **3**(11): p. 5750-5777.
70. Wang, X., et al., *A novel composite containing nanosized silicon and tin as anode material for lithium ion batteries.* Electrochimica Acta, 2009. **54**(20): p. 4662-4667.
71. Lee, Y.J., et al., *Fabricating genetically engineered high-power lithium-ion batteries using multiple virus genes.* Science, 2009. **324**(5930): p. 1051-1055.
72. Chen, H., et al., *From biomass to a renewable LixC6O6 organic electrode for sustainable Li-ion batteries.* ChemSusChem: Chemistry & Sustainability Energy & Materials, 2008. **1**(4): p. 348-355.
73. Zackrisson, M., L. Avellán, and J. Orlenius, *Life cycle assessment of lithium-ion batteries for plug-in hybrid electric vehicles–Critical issues.* Journal of cleaner production, 2010. **18**(15): p. 1519-1529.
74. Deng, D., *Li-ion batteries: basics, progress, and challenges.* Energy Science & Engineering, 2015. **3**(5): p. 385-418.
75. Antolini, E., *LiCoO2: formation, structure, lithium and oxygen nonstoichiometry, electrochemical behaviour and transport properties.* Solid state ionics, 2004. **170**(3-4): p. 159-171.
76. Akimoto, J., Y. Gotoh, and Y. Oosawa, *Synthesis and structure refinement of LiCoO2Single crystals*. 1998, Elsevier. p. 298-302.
77. Belov, D. and M.-H. Yang, *Investigation of the kinetic mechanism in overcharge process for Li-ion battery.* Solid State Ionics, 2008. **179**(27-32): p. 1816-1821.
78. Belov, D. and M.-H. Yang, *Failure mechanism of Li-ion battery at overcharge conditions.* Journal of Solid State Electrochemistry, 2008. **12**: p. 885-894.
79. Doh, C.-H., et al., *Thermal and electrochemical behaviour of C/LixCoO2 cell during safety test.* Journal of Power Sources, 2008. **175**(2): p. 881-885.
80. Takahashi, Y., et al., *Development of lithium-ion batteries with a LiCoO2 cathode toward high capacity by elevating charging potential.* Journal of the electrochemical society, 2008. **155**(7): p. A537.
81. Amatucci, G., J. Tarascon, and L. Klein, *Cobalt dissolution in LiCoO2-based non-aqueous rechargeable batteries.* Solid state ionics, 1996. **83**(1-2): p. 167-173.
82. Amatucci, G., J. Tarascon, and L. Klein, *CoO2, the end member of the Li x CoO2 solid solution.* Journal of The Electrochemical Society, 1996. **143**(3): p. 1114.
83. Ohzuku, T. and A. Ueda, *Solid-state redox reactions of LiCoO2 (R3m) for 4 volt secondary lithium cells.* Journal of The Electrochemical Society, 1994. **141**(11): p. 2972.
84. Zhou, J. and P. Notten, *Studies on the degradation of Li-ion batteries by the use of microreference electrodes.* Journal of power Sources, 2008. **177**(2): p. 553-560.
85. Ménétrier, M., et al., *On "really" stoichiometric LiCoO2.* Electrochemical and Solid-State Letters, 2008. **11**(11): p. A179.
86. Pereira, N., et al., *Thermodynamically induced surface modification for the stabilization of high-capacity LiCoO2.* Journal of The Electrochemical Society, 2008. **155**(11): p. A831.
87. Yamada, A., S.-C. Chung, and K. Hinokuma, *Optimized LiFePO4 for lithium battery cathodes.* Journal of the electrochemical society, 2001. **148**(3): p. A224.
88. Amriou, T., et al., *Ab initio investigation of the Jahn–Teller distortion effect on the stabilizing lithium intercalated compounds.* Materials chemistry and physics, 2005. **92**(2-3): p. 499-504.

89. Liu, H., Y. Yang, and J. Zhang, *Reaction mechanism and kinetics of lithium ion battery cathode material LiNiO2 with CO2.* Journal of Power Sources, 2007. **173**(1): p. 556-561.
90. Rougier, A., P. Gravereau, and C. Delmas, *Optimization of the composition of the Li1− z Ni1+ z O 2 electrode materials: structural, magnetic, and electrochemical studies.* Journal of The Electrochemical Society, 1996. **143**(4): p. 1168.
91. Thongtem, T. and S. Thongtem, *Characterization of Li 1− x Ni 1+ x O 2 prepared using succinic acid as a complexing agent.* Inorganic materials, 2006. **42**: p. 202-209.
92. Whittingham, M.S., *Lithium batteries and cathode materials.* Chemical reviews, 2004. **104**(10): p. 4271-4302.
93. Shi, X., et al., *Synthesis and electrochemical properties of LiNi0. 9Co0. 1O2 cathode material for lithium secondary battery.* Materials Chemistry and Physics, 2009. **113**(2-3): p. 780-783.
94. Lee, D.G., et al., *Improved electrochemical properties of Li (Ni 0.7 Co 0.3) O 2 cathode for lithium ion batteries with controlled sintering conditions.* Journal of applied electrochemistry, 2009. **39**: p. 671-679.
95. Li, D., et al., *Synthesis and characterization of LiNi1− xCoxO2 for lithium batteries by a novel method.* Materials Chemistry and Physics, 2008. **107**(1): p. 171-176.
96. Baskaran, R., et al., *Structural and electrochemical studies on thin film LiNi0. 8Co0. 2O2 by PLD for micro battery.* Solid State Ionics, 2009. **180**(6-8): p. 636-643.
97. Sakamoto, K., et al., *Surface structure of LiNi0. 8Co0. 2O2: A new experimental technique using in situ x-ray diffraction and two-dimensional epitaxial film electrodes.* Chemistry of materials, 2009. **21**(13): p. 2632-2640.
98. Armstrong, A., A. Robertson, and P. Bruce, *Structural transformation on cycling layered Li (Mn1− yCoy) O2 cathode materials.* Electrochimica Acta, 1999. **45**(1-2): p. 285-294.
99. Ammundsen, B., et al., *Formation and structural properties of layered LiMnO2 cathode materials.* Journal of the Electrochemical Society, 2000. **147**(11): p. 4078.
100. Xu, H., Q. Wang, and C. Chen, *Synthesis of Li [Li 0.2 Ni 0.2 Mn 0.6] O 2 by radiated polymer gel method and impact of deficient Li on its structure and electrochemical properties.* Journal of Solid State Electrochemistry, 2008. **12**: p. 1173-1178.
101. Jiang, M., et al., *Electrochemical and structural study of the layered,"Li-excess" lithium-ion battery electrode material Li [Li1/9Ni1/3Mn5/9] O2.* Chemistry of Materials, 2009. **21**(13): p. 2733-2745.
102. Wang, L., et al., *Recent advances in layered LiNi x Co y Mn 1− x− y O 2 cathode materials for lithium ion batteries.* Journal of Solid State Electrochemistry, 2009. **13**: p. 1157-1164.
103. Wu, Y. and A. Manthiram, *Structural stability of chemically delithiated layered (1− z) Li [Li1/3Mn2/3] O2–zLi [Mn0. 5− yNi0. 5− yCo2y] O2 solid solution cathodes.* Journal of power sources, 2008. **183**(2): p. 749-754.
104. Stewart, S.G., V. Srinivasan, and J. Newman, *Modeling the performance of lithium-ion batteries and capacitors during hybrid-electric-vehicle operation.* Journal of The Electrochemical Society, 2008. **155**(9): p. A664.
105. Martha, S., et al., *A short review on surface chemical aspects of Li batteries: A key for a good performance.* Journal of Power Sources, 2009. **189**(1): p. 288-296.
106. Martha, S.K., et al., *A comparative study of electrodes comprising nanometric and submicron particles of LiNi0. 50Mn0. 50O2, LiNi0. 33Mn0. 33Co0. 33O2, and LiNi0. 40Mn0. 40Co0. 20O2 layered compounds.* Journal of Power Sources, 2009. **189**(1): p. 248-255.

107. Dahbi, M., et al., *A delithiated LiNi0. 65Co0. 25Mn0. 10O2 electrode material: A structural, magnetic and electrochemical study.* Electrochimica Acta, 2009. **54**(11): p. 3211-3217.
108. Lu, C.-H. and Y.-K. Lin, *Microemulsion preparation and electrochemical characteristics of LiNi1/3Co1/3Mn1/3O2 powders.* Journal of Power Sources, 2009. **189**(1): p. 40-44.
109. Li, D., et al., *Synthesis and electrochemical properties of LiNi 0.85− x Co x Mn 0.15 O 2 as cathode materials for lithium-ion batteries.* Journal of solid state electrochemistry, 2008. **12**: p. 323-327.
110. Wu, Y. and A. Manthiram, *Effect of surface modifications on the layered solid solution cathodes (1− z) Li [Li1/3Mn2/3] O2−(z) Li [Mn0. 5− yNi0. 5− yCo2y] O2.* Solid State Ionics, 2009. **180**(1): p. 50-56.
111. Kosova, N., et al., *Effect of electronic state of ions on the electrochemical properties of layered cathode materials LiNi 1− 2 x Co x Mn x O 2.* Russian Journal of Electrochemistry, 2008. **44**: p. 543-549.
112. Churikov, A., et al., *Electrochemical properties of LiMn 2− y Me y O 4 (Me= Cr, Co, Ni) spinels as cathodic materials for lithium-ion batteries.* Russian Journal of Electrochemistry, 2009. **45**: p. 175-182.
113. Myung, S.-T., et al., *Structural, Electrochemical, and Thermal Aspects of Li [(Ni0. 5Mn0. 5) 1− x Co x] O2 (0≤ x≤ 0.2) for High-Voltage Application of Lithium-Ion Secondary Batteries.* Journal of the Electrochemical Society, 2008. **155**(5): p. A374.
114. Li, J., et al., *Synthesis and characterization of LiNi0. 6Mn0. 4− xCoxO2 as cathode materials for Li-ion batteries.* Journal of Power Sources, 2009. **189**(1): p. 28-33.
115. Bang, H., et al., *Effects of Metal Ions on the Structural and Thermal Stabilities of Li [Ni1− x− y Co x Mn y] O2 (x+ y⩽ 0.5) Studied by In Situ High Temperature XRD.* Journal of The Electrochemical Society, 2008. **155**(12): p. A952.
116. Xiao, J., N.A. Chernova, and M.S. Whittingham, *Layered mixed transition metal oxide cathodes with reduced cobalt content for lithium ion batteries.* Chemistry of Materials, 2008. **20**(24): p. 7454-7464.
117. Oh, S.W., et al., *Effects of Co doping on Li [Ni0. 5CoxMn1. 5− x] O4 spinel materials for 5 V lithium secondary batteries via Co-precipitation.* Journal of Power Sources, 2009. **189**(1): p. 752-756.
118. Wu, H., et al., *Effects of abundant Co doping on the structure and electrochemical characteristics of LiMn1. 5Ni0. 5− xCoxO4.* Journal of Electroanalytical Chemistry, 2007. **608**(1): p. 8-14.
119. Rosciano, F., et al., *Electrochemical stress at high potential to investigate phase transitions in Li1. 1 (Ni1/3Mn1/3Co1/3) 0.9 O2.* Electrochemical and Solid-State Letters, 2009. **12**(7): p. A140.
120. Tran, N., et al., *Mechanisms associated with the "plateau" observed at high voltage for the overlithiated Li1. 12 (Ni0. 425Mn0. 425Co0. 15) 0.88 O2 system.* Chemistry of Materials, 2008. **20**(15): p. 4815-4825.
121. Park, S.-H., et al., *Physical and electrochemical properties of spherical Li1+ x (Ni1/3Co1/3Mn1/3) 1− xO2 cathode materials.* Journal of Power Sources, 2008. **177**(1): p. 177-183.
122. Kim, J.-M., N. Kumagai, and T.-H. Cho, *Synthesis, Structure, and Electrochemical Characteristics of Overlithiated Li1+ x (Ni z Co1− 2z Mn z) 1− x O2 (z= 0.1–0.4 and x= 0.0–0.1) Positive Electrodes Prepared by Spray-Drying Method.* Journal of the Electrochemical Society, 2007. **155**(1): p. A82.
123. La Mantia, F., et al., *Direct evidence of oxygen evolution from Li 1+ x (Ni 1/3 Mn 1/3 Co 1/3) 1− x O 2 at high potentials.* Journal of Applied Electrochemistry, 2008. **38**: p. 893-896.

124. Kang, S.-H., et al., *First-cycle irreversibility of layered Li–Ni–Co–Mn oxide cathode in Li-ion batteries.* Electrochimica Acta, 2008. **54**(2): p. 684-689.
125. Thackeray, M., A. De Kock, and W. David, *Synthesis and structural characterization of defect spinels in the lithium-manganese-oxide system.* Materials Research Bulletin, 1993. **28**(10): p. 1041-1049.
126. Du Pasquier, A., C. Huang, and T. Spitler, *Nano Li4Ti5O12–LiMn2O4 batteries with high power capability and improved cycle-life.* Journal of Power Sources, 2009. **186**(2): p. 508-514.
127. Belharouak, I., et al., *On the safety of the Li4Ti5O12/ LiMn2O4 lithium-ion battery system.* Journal of the Electrochemical Society, 2007. **154**(12): p. A1083.
128. Takami, N., et al., *Electrochemical kinetics and safety of 2-volt class Li-ion battery system using lithium titanium oxide anode.* Journal of the electrochemical society, 2008. **156**(2): p. A128.
129. Liu, Q., et al., *Phase conversion and morphology evolution during hydrothermal preparation of orthorhombic LiMnO2 nanorods for lithium ion battery application.* Journal of power sources, 2007. **173**(1): p. 538-544.
130. Molenda, J., et al., *Electrochemical and high temperature physicochemical properties of orthorhombic LiMnO2.* Journal of power sources, 2007. **173**(2): p. 707-711.
131. Thackeray, M.M., *Spinel electrodes for lithium batteries.* Journal of the American Ceramic Society, 1999. **82**(12): p. 3347-3354.
132. Matsushima, T., *Deterioration estimation of lithium-ion cells in direct current power supply systems and characteristics of 400-Ah lithium-ion cells.* Journal of Power Sources, 2009. **189**(1): p. 847-854.
133. Deng, B., H. Nakamura, and M. Yoshio, *Capacity fading with oxygen loss for manganese spinels upon cycling at elevated temperatures.* Journal of power sources, 2008. **180**(2): p. 864-868.
134. Yunjian, L., et al., *Electrochemical performance and capacity fading reason of LiMn2O4/graphite batteries stored at room temperature.* Journal of Power Sources, 2009. **189**(1): p. 721-725.
135. Doi, T., et al., *Electrochemical AFM study of LiMn2O4 thin film electrodes exposed to elevated temperatures.* Journal of Power Sources, 2008. **180**(1): p. 539-545.
136. Mateyshina, Y.G., et al., *Physical and electrochemical properties of LiFe 0.5 Mn 1.5 O 4 spinel synthesized by different methods.* Russian Journal of Electrochemistry, 2009. **45**: p. 602-605.
137. Shigemura, H., et al., *Structure and Electrochemical Properties of LiFe x Mn2− x O 4 (0⩽ x⩽ 0.5) Spinel as 5 V Electrode Material for Lithium Batteries.* Journal of the Electrochemical Society, 2001. **148**(7): p. A730.
138. Arora, P., B. Popov, and R.E. White, *Electrochemical Investigations of Cobalt-Doped LiMn2 O 4 as Cathode Material for Lithium-Ion Batteries.* Journal of the electrochemical society, 1998. **145**(3): p. 807.
139. Wang, C., et al., *Enhanced capacity retention of Co and Li doubly doped LiMn2O4.* Journal of Power Sources, 2009. **189**(1): p. 607-610.
140. Amdouni, N., et al., *Structural, Magnetic and Electrochemical Properties of the Spinel LiMn2-yCoyO4 Nanosized Powders.* MRS Online Proceedings Library (OPL), 2006. **973**: p. 0973-BB04-04.
141. Amarilla, J., et al., *Sucrose-aided combustion synthesis of nanosized LiMn1. 99− yLiyM0. 01O4 (M= Al3+, Ni2+, Cr3+, Co3+, y= 0.01 and 0.06) spinels: Characterization and electrochemical behavior at 25 and at 55 C in rechargeable lithium cells.* Journal of power sources, 2009. **191**(2): p. 591-600.
142. Zhao, S., et al., *Electrochemical properties of spinel LiCoxMn2− xO4 prepared by sol–gel process.* Journal of alloys and compounds, 2009. **474**(1-2): p. 473-476.

143. Huang, H., et al., *Electrochemical study on LiCo1/6Mn11/6O4 as cathode material for lithium ion batteries at elevated temperature.* Journal of Power Sources, 2008. **184**(2): p. 583-588.
144. Ohzuku, T., S. Takeda, and M. Iwanaga, *Solid-state redox potentials for Li [Me1/2Mn3/2] O4 (Me: 3d-transition metal) having spinel-framework structures: a series of 5 volt materials for advanced lithium-ion batteries.* Journal of Power Sources, 1999. **81**: p. 90-94.
145. Fang, T.T. and H.Y. Chung, *Reassessment of the Electronic-Conduction Behavior above the Verwey-Like Transition of Ni2+-and Al3+-Doped LiMn2O4.* Journal of the American ceramic society, 2008. **91**(1): p. 342-345.
146. Patoux, S., et al., *High voltage spinel oxides for Li-ion batteries: From the material research to the application.* Journal of Power Sources, 2009. **189**(1): p. 344-352.
147. Sung, N.-E., et al., *In Situ XAFS Study of the Effect of Dopants in Li1+ x Ni (1− 3x)⁄ 2Mn (3+ x)⁄ 2O4 (0⩽ x⩽ 1⁄ 3), a Li-Ion Battery Cathode Material.* Journal of The Electrochemical Society, 2008. **155**(11): p. A845.
148. Shaju, K.M. and P.G. Bruce, *Nano-LiNi 0.5 Mn 1.5 O 4 spinel: a high power electrode for Li-ion batteries.* Dalton Transactions, 2008(40): p. 5471-5475.
149. Liu, J. and A. Manthiram, *Understanding the improvement in the electrochemical properties of surface modified 5 V LiMn1. 42Ni0. 42Co0. 16O4 spinel cathodes in lithium-ion cells.* Chemistry of Materials, 2009. **21**(8): p. 1695-1707.
150. Yuan, Y., et al., *Preparation, characteristics and electrochemical properties of surface-modified LiMn2O4 by doped LiNi0. 05Mn1. 95O4.* Applied Surface Science, 2008. **255**(5): p. 2225-2229.
151. Lee, J.-W., S.-M. Park, and H.-J. Kim, *Effect of LiNi1/2Mn1/2O2 coating on the electrochemical performance of Li–Mn spinel.* Electrochemistry communications, 2009. **11**(6): p. 1101-1104.
152. Li, X. and Y. Xu, *Spinel LiMn2O4 active material with high capacity retention.* Applied surface science, 2007. **253**(21): p. 8592-8596.
153. Sahana, M., et al., *The effect of titanium on the lithium intercalation capacity of V2O5 thin films.* Thin Solid Films, 2009. **517**(24): p. 6642-6651.
154. Li, G., et al., *Environmentally friendly chemical route to vanadium oxide single-crystalline nanobelts as a cathode material for lithium-ion batteries.* The Journal of Physical Chemistry B, 2006. **110**(19): p. 9383-9386.
155. Feng, C., et al., *Synthesis of spherical porous vanadium pentoxide and its electrochemical properties.* Journal of Power Sources, 2008. **184**(2): p. 485-488.
156. Mohan, V., et al., *Synthesis, structural, and electrochemical performance of V 2 O 5 nanotubes as cathode material for lithium battery.* Journal of Applied Electrochemistry, 2009. **39**: p. 2001-2006.
157. Wang, Y., et al., *Nanostructured vanadium oxide electrodes for enhanced lithium-ion intercalation.* Advanced Functional Materials, 2006. **16**(9): p. 1133-1144.
158. Benedek, R., M. Thackeray, and L. Yang, *Lithium site preference and electronic structure of Li 4 V 3 O 8.* Physical Review B, 1997. **56**(17): p. 10707.
159. Liu, Y., X. Zhou, and Y. Guo, *Structure and electrochemical performance of LiV3O8 synthesized by solid-state routine with quenching in freezing atmosphere.* Materials Chemistry and Physics, 2009. **114**(2-3): p. 915-919.
160. Wu, F., et al., *Study on Li1+ xV3O8 synthesized by microwave sol–gel route.* Materials Chemistry and Physics, 2009. **115**(2-3): p. 707-711.
161. Sun, J., et al., *Effect of PEG molecular weight on the crystal structure and electrochemical performance of LiV 3 O 8.* Journal of Solid State Electrochemistry, 2010. **14**: p. 615-619.

162. Liu, H., et al., *Synthesis and electrochemical properties of single-crystalline LiV3O8 nanorods as cathode materials for rechargeable lithium batteries.* Journal of Power Sources, 2009. **192**(2): p. 668-673.
163. Padhi, A.K., K.S. Nanjundaswamy, and J.B. Goodenough, *Phospho-olivines as positive-electrode materials for rechargeable lithium batteries.* Journal of the electrochemical society, 1997. **144**(4): p. 1188.
164. Padhi, A., et al., *Effect of structure on the Fe3+/Fe2+ redox couple in iron phosphates.* Journal of the Electrochemical Society, 1997. **144**(5): p. 1609.
165. Axmann, P., et al., *Nonstoichiometric LiFePO4: defects and related properties.* Chemistry of Materials, 2009. **21**(8): p. 1636-1644.
166. Chen, J., et al., *The hydrothermal synthesis and characterization of olivines and related compounds for electrochemical applications.* Solid State Ionics, 2008. **178**(31-32): p. 1676-1693.
167. Maier, J. and R. Amin, *Defect chemistry of LiFePO4.* Journal of The Electrochemical Society, 2008. **155**(4): p. A339.
168. Kobayashi, G., et al., *Isolation of Solid Solution Phases in Size-Controlled LixFePO4 at Room Temperature.* Advanced Functional Materials, 2009. **19**(3): p. 395-403.
169. Maccario, M., et al., *Raman and FTIR Spectroscopy Investigations of Carbon-Coated Li x FePO4 Materials.* Journal of the Electrochemical Society, 2008. **155**(12): p. A879.
170. Kasavajjula, U.S., C. Wang, and P.E. Arce, *Discharge model for LiFePO4 accounting for the solid solution range.* Journal of The Electrochemical Society, 2008. **155**(11): p. A866.
171. Dedryvère, R., et al., *X-ray photoelectron spectroscopy investigations of carbon-coated Li x FePO4 materials.* Chemistry of Materials, 2008. **20**(22): p. 7164-7170.
172. Allen, J., T. Jow, and J. Wolfenstine, *Analysis of the FePO 4 to LiFePO 4 phase transition.* Journal of Solid State Electrochemistry, 2008. **12**: p. 1031-1033.
173. Meethong, N., et al., *Electrochemically induced phase transformation in nanoscale olivines Li1− x MPO4 (M= Fe, Mn).* Chemistry of Materials, 2008. **20**(19): p. 6189-6198.
174. Sigle, W., et al., *Delithiation study of LiFePO4 crystals using electron energy-loss spectroscopy.* Electrochemical and Solid-State Letters, 2009. **12**(8): p. A151.
175. Ellis, B., et al., *Small polaron hopping in Li x FePO4 solid solutions: coupled lithium-ion and electron mobility.* Journal of the American Chemical Society, 2006. **128**(35): p. 11416-11422.
176. Amin, R. and J. Maier, *Effect of annealing on transport properties of LiFePO4: Towards a defect chemical model.* Solid State Ionics, 2008. **178**(35-36): p. 1831-1836.
177. Whittingham, M.S., *Inorganic nanomaterials for batteries.* Dalton Transactions, 2008(40): p. 5424-5431.
178. Zaghib, K., et al., *Magnetic studies of phospho-olivine electrodes in relation with their electrochemical performance in Li-ion batteries.* Solid State Ionics, 2008. **179**(1-6): p. 16-23.
179. Kang, H.-C., et al., *Optimized solid-state synthesis of LiFePO4 cathode materials using ball-milling.* Journal of Power Sources, 2008. **179**(1): p. 340-346.
180. Ojczyk, W., et al., *Studies of selected synthesis procedures of the conducting LiFePO4-based composite cathode materials for Li-ion batteries.* Journal of Power Sources, 2007. **173**(2): p. 700-706.
181. Liu, H., J. Xie, and K. Wang, *Synthesis and characterization of LiFePO4/(C+ Fe2P) composite cathodes.* Solid State Ionics, 2008. **179**(27-32): p. 1768-1771.
182. Lin, Y., et al., *Effects of carbon coating and iron phosphides on the electrochemical properties of LiFePO4/C.* Journal of Power Sources, 2008. **184**(2): p. 444-448.

183. Liu, H. and D. Tang, *The low cost synthesis of nanoparticles LiFePO4/C composite for lithium rechargeable batteries.* Solid State Ionics, 2008. **179**(33-34): p. 1897-1901.
184. Song, M.-S., et al., *Amphoteric effects of Fe2P on electrochemical performance of lithium iron phosphate–carbon composite synthesized by ball-milling and microwave heating.* Journal of Power Sources, 2008. **180**(1): p. 546-552.
185. Shiratsuchi, T., et al., *Cathodic performance of LiMn1− xMxPO4 (M= Ti, Mg and Zr) annealed in an inert atmosphere.* Electrochimica Acta, 2009. **54**(11): p. 3145-3151.
186. Kim, S.-W., et al., *Phase stability study of Li1− x MnPO4 (0⩽ x⩽ 1) cathode for Li rechargeable battery.* Journal of The Electrochemical Society, 2009. **156**(8): p. A635.
187. Murugan, A.V., T. Muraliganth, and A. Manthiram, *One-pot microwave-hydrothermal synthesis and characterization of carbon-coated LiMPO4 (M= Mn, Fe, and Co) cathodes.* Journal of the Electrochemical Society, 2008. **156**(2): p. A79.
188. Bramnik, N.N., et al., *Thermal stability of LiCoPO4 cathodes.* Electrochemical and Solid-State Letters, 2008. **11**(6): p. A89.
189. Lee, K.T. and K.S. Lee, *Electrochemical properties of LiFe0. 9Mn0. 1PO4/Fe2P cathode material by mechanical alloying.* Journal of Power Sources, 2009. **189**(1): p. 435-439.
190. Chen, Y.-C., et al., *Structure studies on LiMn0. 25Fe0. 75PO4 by in-situ synchrotron X-ray diffraction analysis.* Journal of Power Sources, 2009. **189**(1): p. 790-793.
191. Kim, J.-K., et al., *Effect of synthetic conditions on the electrochemical properties of LiMn0. 4Fe0. 6PO4/C synthesized by sol–gel technique.* Journal of Power Sources, 2009. **189**(1): p. 391-396.
192. Han, D.-W., et al., *Effects of Fe doping on the electrochemical performance of LiCoPO4/C composites for high power-density cathode materials.* Electrochemistry Communications, 2009. **11**(1): p. 137-140.
193. Shanmukaraj, D., et al., *Electrochemical studies on LiFe1− xCoxPO4/carbon composite cathode materials synthesized by citrate gel technique for lithium-ion batteries.* Materials Science and Engineering: B, 2008. **149**(1): p. 93-98.
194. Baek, D.-H., et al., *Effect of firing temperature on the electrochemical performance of LiMn0. 4Fe0. 6PO4/C materials prepared by mechanical activation.* Journal of Power Sources, 2009. **189**(1): p. 59-65.
195. Kobayashi, G., et al., *Shift of redox potential and kinetics in Lix (MnyFe1− y) PO4.* Journal of Power Sources, 2009. **189**(1): p. 397-401.
196. Kope, M., et al., *Structural and magnetic properties of Lix (MnyFe1− y) PO4 electrode materials for Li-ion batteries.* Journal of Power Sources, 2009. **189**(2): p. 1154-1163.
197. Yang, M.-R. and W.-H. Ke, *The doping effect on the electrochemical properties of LiFe0. 95M0. 05PO4 (M= Mg2+, Ni2+, Al3+, or V3+) as cathode materials for lithium-ion cells.* Journal of the Electrochemical Society, 2008. **155**(10): p. A729.
198. Lu, Y., et al., *Synthesis of LiFe1− xNixPO4/C composites and their electrochemical performance.* Journal of Power Sources, 2009. **194**(2): p. 786-793.
199. Chen, G., J.D. Wilcox, and T.J. Richardson, *Improving the performance of lithium manganese phosphate through divalent cation substitution.* Electrochemical and solid-state letters, 2008. **11**(11): p. A190.
200. Liu, X.-H., et al., *Electrochemical properties of rechargeable aqueous lithium ion batteries with an olivine-type cathode and a Nasicon-type anode.* Journal of Power Sources, 2009. **189**(1): p. 706-710.
201. Zhang, Y., C. Sun, and Z. Zhou, *Sol–gel preparation and electrochemical performances of LiFe1/3Mn1/3Co1/3PO4/C composites with core–shell nanostructure.* Electrochemistry communications, 2009. **11**(6): p. 1183-1186.
202. Wang, X., et al., *Li-storage in LiFe1/4Mn1/4Co1/4Ni1/4PO4 solid solution.* Electrochemistry Communications, 2008. **10**(9): p. 1347-1350.

203. Nam, K.-W., et al., *In situ X-ray absorption and diffraction studies of carbon coated LiFe1/4Mn1/4Co1/4Ni1/4PO4 cathode during first charge.* Electrochemistry communications, 2009. **11**(4): p. 913-916.
204. Zhu, X., et al., *Synthesis and characteristics of Li3V2 (PO4) 3 as cathode materials for lithium-ion batteries.* Solid State Ionics, 2008. **179**(27-32): p. 1679-1682.
205. Chen, Q., et al., *Electrochemical performance of the carbon coated Li3V2 (PO4) 3 cathode material synthesized by a sol–gel method.* Electrochimica Acta, 2007. **52**(16): p. 5251-5257.
206. Huang, H., et al., *Lithium metal phosphates, power and automotive applications.* Journal of Power Sources, 2009. **189**(1): p. 748-751.
207. Yu, F., et al., *Preparation and electrochemical performance of Li 3 V 2 (PO 4) 3/C cathode material by spray-drying and carbothermal method.* Journal of Solid State Electrochemistry, 2010. **14**: p. 883-888.
208. Hong, J., et al., *Vanadium modified LiFePO4 cathode for Li-ion batteries.* Electrochemical and Solid-State Letters, 2008. **12**(2): p. A33.
209. Sun, C., et al., *Improved high-rate charge/discharge performances of LiFePO4/C via V-doping.* Journal of Power Sources, 2009. **193**(2): p. 841-845.
210. Nishi, Y., *Performance of the first lithium ion battery and its process technology.* Lithium Ion Batteries: Fundamentals and Performance, 1998: p. 181-198.
211. Shu, Z., R. McMillan, and J. Murray, *Electrochemical intercalation of lithium into graphite.* Journal of The Electrochemical Society, 1993. **140**(4): p. 922.
212. Ohzuku, T., Y. Iwakoshi, and K. Sawai, *Formation of lithium-graphite intercalation compounds in nonaqueous electrolytes and their application as a negative electrode for a lithium ion (shuttlecock) cell.* Journal of The Electrochemical Society, 1993. **140**(9): p. 2490.
213. Dahn, J., et al., *Dependence of the electrochemical intercalation of lithium in carbons on the crystal structure of the carbon.* Electrochimica Acta, 1993. **38**(9): p. 1179-1191.
214. Sonobe, N., M. Ishikawa, and T. Iwasaki, *Abstract of the 35th Battery Symposium in Japan*. 1994, Japan.
215. Wakihara, M., *Recent developments in lithium ion batteries.* Materials Science and Engineering: R: Reports, 2001. **33**(4): p. 109-134.
216. Mabuchi, A., et al., *Charge-discharge characteristics of the mesocarbon miocrobeads heat-treated at different temperatures.* Journal of the Electrochemical Society, 1995. **142**(4): p. 1041.
217. Sato, K., et al., *A mechanism of lithium storage in disordered carbons.* Science, 1994. **264**(5158): p. 556-558.
218. Zheng, T., J. Xue, and J. Dahn, *Lithium insertion in hydrogen-containing carbonaceous materials.* Chemistry of materials, 1996. **8**(2): p. 389-393.
219. Takamura, T., et al., *Enhancement of Li doping/undoping reaction rate of carbonaceous materials by coating with an evaporated metal film.* Journal of power sources, 1999. **81**: p. 368-372.
220. Besenhard, J., J. Yang, and M. Winter, *Will advanced lithium-alloy anodes have a chance in lithium-ion batteries?* Journal of Power Sources, 1997. **68**(1): p. 87-90.
221. Nagayama, M., et al., *A new anode material SnSO4 for lithium secondary battery.* Solid State Ionics, 1998. **106**(1-2): p. 33-38.
222. Idota, Y., et al., *Tin-based amorphous oxide: a high-capacity lithium-ion-storage material.* Science, 1997. **276**(5317): p. 1395-1397.
223. Denis, S., et al., *Synthesis and electrochemical properties of numerous classes of vanadates.* Journal of power sources, 1999. **81**: p. 79-84.

224. Kim, S.-S., H. Ikuta, and M. Wakihara, *Synthesis and characterization of MnV2O6 as a high capacity anode material for a lithium secondary battery.* Solid State Ionics, 2001. **139**(1-2): p. 57-65.
225. Goriparti, S., et al., *Review on recent progress of nanostructured anode materials for Li-ion batteries.* Journal of power sources, 2014. **257**: p. 421-443.
226. Ryu, J.H., et al., *Failure modes of silicon powder negative electrode in lithium secondary batteries.* Electrochemical and solid-state letters, 2004. **7**(10): p. A306.
227. Tamura, N., et al., *Study on the anode behavior of Sn and Sn–Cu alloy thin-film electrodes.* Journal of Power Sources, 2002. **107**(1): p. 48-55.
228. Courtney, I.A. and J. Dahn, *Electrochemical and in situ X-ray diffraction studies of the reaction of lithium with tin oxide composites.* Journal of the Electrochemical Society, 1997. **144**(6): p. 2045.
229. Zhang, W.-J., *Lithium insertion/extraction mechanism in alloy anodes for lithium-ion batteries.* Journal of Power Sources, 2011. **196**(3): p. 877-885.
230. Wen, C.J. and R.A. Huggins, *Chemical diffusion in intermediate phases in the lithium-silicon system.* Journal of solid state chemistry, 1981. **37**(3): p. 271-278.
231. Limthongkul, P., et al., *Electrochemically-driven solid-state amorphization in lithium-silicon alloys and implications for lithium storage.* Acta Materialia, 2003. **51**(4): p. 1103-1113.
232. Obrovac, M. and L. Christensen, *Structural changes in silicon anodes during lithium insertion/extraction.* Electrochemical and solid-state letters, 2004. **7**(5): p. A93.
233. Li, J. and J. Dahn, *An in situ X-ray diffraction study of the reaction of Li with crystalline Si.* Journal of The Electrochemical Society, 2007. **154**(3): p. A156.
234. Hatchard, T. and J. Dahn, *In situ XRD and electrochemical study of the reaction of lithium with amorphous silicon.* Journal of The Electrochemical Society, 2004. **151**(6): p. A838.
235. Dey, A., *Electrochemical alloying of lithium in organic electrolytes.* Journal of The Electrochemical Society, 1971. **118**(10): p. 1547.
236. Kwon, Y., et al., *Sn0. 9Si0. 1/Carbon Core− Shell Nanoparticles for High-Density Lithium Storage Materials.* Chemistry of materials, 2007. **19**(5): p. 982-986.
237. Beaulieu, L., et al., *Reaction of Li with alloy thin films studied by in situ AFM.* Journal of the Electrochemical Society, 2003. **150**(11): p. A1457.
238. Mukaibo, H., et al., *In situ stress transition observations of electrodeposited Sn-based anode materials for lithium-ion secondary batteries.* Electrochemical and solid-state letters, 2007. **10**(3): p. A70.
239. Zhu, J., et al., *Facile synthesis of metal oxide/reduced graphene oxide hybrids with high lithium storage capacity and stable cyclability.* Nanoscale, 2011. **3**(3): p. 1084-1089.
240. Wang, Z., L. Zhou, and X.W. Lou, *Metal oxide hollow nanostructures for lithium-ion batteries*. 2012, Wiley Online Library.
241. Hang, B.T., et al., *Electrochemical properties of nano-sized Fe2O3-loaded carbon as a lithium battery anode.* Journal of power sources, 2006. **161**(2): p. 1281-1287.
242. Poizot, P., et al., *Nano-sized transition-metal oxides as negative-electrode materials for lithium-ion batteries.* Nature, 2000. **407**(6803): p. 496-499.
243. Larcher, D., et al., *The electrochemical reduction of Co3 O 4 in a lithium cell.* Journal of the Electrochemical Society, 2002. **149**(3): p. A234.
244. Lu, X., et al., *New insight into the atomic-scale bulk and surface structure evolution of Li4Ti5O12 anode.* Journal of the American Chemical Society, 2015. **137**(4): p. 1581-1586.
245. Zhu, G.N., et al., *Binary Li4Ti5O12-Li2Ti3O7 nanocomposite as an anode material for Li-Ion batteries.* Advanced Functional Materials, 2013. **23**(5): p. 640-647.

246. Li, H., et al., *Li3VO4: a promising insertion anode material for lithium-ion batteries.* Advanced Energy Materials, 2013. **3**(4): p. 428-432.
247. Guo, Z., et al., *Hard carbon derived from coal tar pitch for use as the anode material in lithium ion batteries.* International Journal of Electrochemical Science, 2013. **8**(2): p. 2702-2709.
248. Noerochim, L., et al., *Free-standing single-walled carbon nanotube/SnO2 anode paper for flexible lithium-ion batteries.* Carbon, 2012. **50**(3): p. 1289-1297.
249. Fang, S., et al., *Ge–graphene–carbon nanotube composite anode for high performance lithium-ion batteries.* Journal of Materials Chemistry A, 2015. **3**(4): p. 1498-1503.
250. Jiao, X., et al., *Amorphous phosphorus-carbon nanotube hybrid anode with ultralong cycle life and high-rate capability for lithium-ion batteries.* Carbon, 2019. **148**: p. 518-524.
251. Takamura, T., et al., *Identification of nano-sized holes by TEM in the graphene layer of graphite and the high rate discharge capability of Li-ion battery anodes.* Electrochimica Acta, 2007. **53**(3): p. 1055-1061.
252. Huang, X., et al., *Graphene-based composites.* Chemical Society Reviews, 2012. **41**(2): p. 666-686.
253. Wen, J., Y. Yu, and C. Chen, *A review on lithium-ion batteries safety issues: existing problems and possible solutions.* Materials express, 2012. **2**(3): p. 197-212.
254. Li, X., et al., *Graphene nanoscrolls encapsulated TiO2 (B) nanowires for lithium storage.* Journal of Power Sources, 2014. **268**: p. 372-378.
255. Jin, J., et al., *Design of new anode materials based on hierarchical, three dimensional ordered macro-mesoporous TiO 2 for high performance lithium ion batteries.* Journal of Materials Chemistry A, 2014. **2**(25): p. 9699-9708.
256. Dambournet, D., I. Belharouak, and K. Amine, *Tailored preparation methods of TiO2 anatase, rutile, brookite: mechanism of formation and electrochemical properties.* Chemistry of materials, 2010. **22**(3): p. 1173-1179.
257. Madej, E., et al., *Effect of the specific surface area on thermodynamic and kinetic properties of nanoparticle anatase TiO2 in lithium-ion batteries.* Journal of Power Sources, 2015. **297**: p. 140-148.
258. Chen, Z., et al., *Titanium-based anode materials for safe lithium-ion batteries.* Advanced Functional Materials, 2013. **23**(8): p. 959-969.
259. Rui, X., et al., *Ambient dissolution–recrystallization towards large-scale preparation of V2O5 nanobelts for high-energy battery applications.* Nano Energy, 2016. **22**: p. 583-593.
260. Ren, Y., et al., *Nanoparticulate TiO2 (B): an anode for lithium-ion batteries.* Angewandte Chemie, 2012. **124**(9): p. 2206-2209.
261. Antony, R.P., et al., *Rapid breakdown anodization technique for the synthesis of high aspect ratio and high surface area anatase TiO2 nanotube powders.* Journal of Solid State Chemistry, 2011. **184**(3): p. 624-632.
262. Motola, M., et al., *Intrinsic properties of high-aspect ratio single-and double-wall anodic TiO2 nanotube layers annealed at different temperatures.* Electrochimica Acta, 2020. **352**: p. 136479.
263. Colbow, K., J. Dahn, and R. Haering, *Structure and electrochemistry of the spinel oxides LiTi2O4 and Li43Ti53O4.* Journal of Power Sources, 1989. **26**(3-4): p. 397-402.
264. Ferg, E., et al., *Spinel anodes for lithium-ion batteries.* Journal of the Electrochemical Society, 1994. **141**(11): p. L147.
265. Ohzuku, T., A. Ueda, and N. Yamamoto, *Zero-strain insertion material of Li [Li1/3Ti5/3] O 4 for rechargeable lithium cells.* Journal of the Electrochemical Society, 1995. **142**(5): p. 1431.

266. Takai, S., et al., *Diffusion coefficient measurement of lithium ion in sintered Li1. 33Ti1. 67O4 by means of neutron radiography.* Solid State Ionics, 1999. **123**(1-4): p. 165-172.
267. Zaghib, K., et al., *Electrochemical study of Li4Ti5O12 as negative electrode for Li-ion polymer rechargeable batteries.* Journal of Power Sources, 1999. **81**: p. 300-305.
268. Peramunage, D. and K. Abraham, *Preparation of Micron-Sized Li4Ti5 O 12 and Its Electrochemistry in Polyacrylonitrile Electrolyte-Based Lithium Cells.* Journal of the Electrochemical Society, 1998. **145**(8): p. 2609.
269. Scharner, S., W. Weppner, and P. Schmid-Beurmann, *Evidence of two-phase formation upon lithium insertion into the Li1. 33Ti1. 67 O 4 spinel.* Journal of the Electrochemical Society, 1999. **146**(3): p. 857.
270. Kavan, L. and M. Grätzel, *Facile synthesis of nanocrystalline Li4Ti5 O 12 (Spinel) exhibiting fast Li insertion.* Electrochemical and Solid-State Letters, 2001. **5**(2): p. A39.
271. Kim, J. and J. Cho, *Spinel Li4Ti5O12 nanowires for high-rate Li-ion intercalation electrode.* Electrochemical and solid-state letters, 2007. **10**(3): p. A81.
272. Ohzuku, T., Z. Takehara, and S. Yoshizawa, *Nonaqueous lithium/titanium dioxide cell.* Electrochimica Acta, 1979. **24**(2): p. 219-222.
273. Kavan, L., D. Fattakhova, and P. Krtil, *Lithium Insertion into Mesoscopic and Single-Crystal TiO2 (Rutile) Electrodes.* Journal of the Electrochemical Society, 1999. **146**(4): p. 1375.
274. Zachau-Christiansen, B., et al., *Lithium insertion in different TiO2 modifications.* Solid State Ionics, 1988. **28**: p. 1176-1182.
275. Macklin, W. and R. Neat, *Performance of titanium dioxide-based cathodes in a lithium polymer electrolyte cell.* Solid State Ionics, 1992. **53**: p. 694-700.
276. Koudriachova, M.V., N.M. Harrison, and S.W. de Leeuw, *Effect of diffusion on lithium intercalation in titanium dioxide.* Physical Review Letters, 2001. **86**(7): p. 1275.
277. Koudriachova, M.V., N.M. Harrison, and S.W. de Leeuw, *Diffusion of Li-ions in rutile. An ab initio study.* Solid State Ionics, 2003. **157**(1-4): p. 35-38.
278. Johnson, O., *One-dimensional diffusion of Li in rutile.* Physical Review, 1964. **136**(1A): p. A284.
279. Gligor, F. and S. De Leeuw, *Lithium diffusion in rutile structured titania.* Solid State Ionics, 2006. **177**(26-32): p. 2741-2746.
280. Stashans, A., et al., *Theoretical study of lithium intercalation in rutile and anatase.* Physical Review B, 1996. **53**(1): p. 159.
281. Baudrin, E., et al., *Structural evolution during the reaction of Li with nano-sized rutile type TiO2 at room temperature.* Electrochemistry communications, 2007. **9**(2): p. 337-342.
282. Hu, Y.S., et al., *High lithium electroactivity of nanometer-sized rutile TiO2.* Advanced Materials, 2006. **18**(11): p. 1421-1426.
283. Delmas, C., et al., *The LixV2O5 system: An overview of the structure modifications induced by the lithium intercalation.* Solid State Ionics, 1994. **69**(3-4): p. 257-264.
284. Reddy, M.A., et al., *Room temperature synthesis and Li insertion into nanocrystalline rutile TiO2.* Electrochemistry communications, 2006. **8**(8): p. 1299-1303.
285. Jiang, C., et al., *Nanocrystalline rutile TiO2 electrode for high-capacity and high-rate lithium storage.* Electrochemical and solid-state letters, 2007. **10**(5): p. A127.
286. Wang, D., et al., *Synthesis and Li-ion insertion properties of highly crystalline mesoporous rutile TiO2.* Chemistry of Materials, 2008. **20**(10): p. 3435-3442.
287. Wagemaker, M., et al., *The life and times of lithium in anatase TiO2.* Solid State Ionics, 2004. **175**(1-4): p. 191-193.

288. Lunell, S., et al., *Li and Na diffusion in TiO2 from quantum chemical theory versus electrochemical experiment.* Journal of the American Chemical Society, 1997. **119**(31): p. 7374-7380.
289. Tielens, F., et al., *Lithium insertion and mobility in the TiO2-anatase/titanate structure: A periodic DFT study.* Journal of Electroanalytical Chemistry, 2005. **581**(2): p. 216-223.
290. Cava, R.J., et al., *The crystal structures of the lithium-inserted metal oxides Li0. 5TiO2 anatase, LiTi2O4 spinel, and Li2Ti2O4.* Journal of Solid State Chemistry, 1984. **53**(1): p. 64-75.
291. Li, J., Z. Tang, and Z. Zhang, *Preparation and novel lithium intercalation properties of titanium oxide nanotubes.* Electrochemical and Solid-State Letters, 2005. **8**(6): p. A316.
292. Sudant, G., et al., *Electrochemical lithium reactivity with nanotextured anatase-type TiO 2.* Journal of Materials Chemistry, 2005. **15**(12): p. 1263-1269.
293. Lindström, H., et al., *Li+ ion insertion in TiO2 (anatase). 2. Voltammetry on nanoporous films.* The Journal of Physical Chemistry B, 1997. **101**(39): p. 7717-7722.
294. van de Krol, R., A. Goossens, and E.A. Meulenkamp, *In situ X-ray diffraction of lithium intercalation in nanostructured and thin film anatase TiO2.* Journal of the Electrochemical Society, 1999. **146**(9): p. 3150.
295. Murphy, D., et al., *Ternary LixTiO2 phases from insertion reactions.* Solid State Ionics, 1983. **9**: p. 413-417.
296. Wagemaker, M., A. Kentgens, and F. Mulder, *Equilibrium lithium transport between nanocrystalline phases in intercalated TiO2 anatase.* Nature, 2002. **418**(6896): p. 397-399.
297. Wagemaker, M., et al., *Multiple Li positions inside oxygen octahedra in lithiated TiO2 anatase.* Journal of the American Chemical Society, 2003. **125**(3): p. 840-848.
298. Wagemaker, M., et al., *Two phase morphology limits lithium diffusion in TiO2 (anatase): A 7Li MAS NMR study.* Journal of the American Chemical Society, 2001. **123**(46): p. 11454-11461.
299. Koudriachova, M.V., N.M. Harrison, and S.W. de Leeuw, *First principles predictions for intercalation behaviour.* Solid State Ionics, 2004. **175**(1-4): p. 829-834.
300. Wagemaker, M., W.J. Borghols, and F.M. Mulder, *Large impact of particle size on insertion reactions. a case for anatase Li x TiO2.* Journal of the American Chemical Society, 2007. **129**(14): p. 4323-4327.
301. Kim, J. and J. Cho, *Rate characteristics of anatase TiO2 nanotubes and nanorods for lithium battery anode materials at room temperature.* Journal of the Electrochemical Society, 2007. **154**(6): p. A542.
302. Kavan, L., et al., *Lithium storage in nanostructured TiO2 made by hydrothermal growth.* Chemistry of Materials, 2004. **16**(3): p. 477-485.
303. Zukalová, M., et al., *Pseudocapacitive lithium storage in TiO2 (B).* Chemistry of Materials, 2005. **17**(5): p. 1248-1255.
304. Gao, X., et al., *Electrochemical performance of anatase nanotubes converted from protonated titanate hydrate nanotubes.* Electrochemical and solid-state letters, 2004. **8**(1): p. A26.
305. Xu, J., et al., *Electrochemical properties of anatase TiO2 nanotubes as an anode material for lithium-ion batteries.* Electrochimica acta, 2007. **52**(28): p. 8044-8047.
306. Bao, S.-J., et al., *Novel porous anatase TiO2 nanorods and their high lithium electroactivity.* Electrochemistry Communications, 2007. **9**(5): p. 1233-1238.
307. Marchand, R., L. Brohan, and M. Tournoux, *TiO2 (B) a new form of titanium dioxide and the potassium octatitanate K2Ti8O17.* Materials Research Bulletin, 1980. **15**(8): p. 1129-1133.

308. Feist, T.P. and P.K. Davies, *The soft chemical synthesis of TiO2 (B) from layered titanates.* Journal of solid state chemistry, 1992. **101**(2): p. 275-295.
309. Armstrong, A.R., et al., *Lithium-ion intercalation into TiO2-B nanowires.* Advanced Materials, 2005. **17**(7): p. 862-865.
310. Armstrong, A.R., et al., *TiO2–B nanowires as negative electrodes for rechargeable lithium batteries.* Journal of Power Sources, 2005. **146**(1-2): p. 501-506.
311. Armstrong, A.R., et al., *TiO2-B nanowires.* Angewandte Chemie International Edition, 2004. **43**(17): p. 2286-2288.
312. Armstrong, G., et al., *TiO2 (B) nanowires as an improved anode material for lithium-ion batteries containing LiFePO4 or LiNi0. 5Mn1. 5O4 cathodes and a polymer electrolyte.* Advanced Materials, 2006. **18**(19): p. 2597-2600.
313. Arico, A.S., et al., *Nanostructured materials for advanced energy conversion and storage devices.* Nature materials, 2005. **4**(5): p. 366-377.
314. Reddy, M.A., et al., *Crystallite size constraints on lithium insertion into brookite TiO2.* Electrochemical and Solid-State Letters, 2008. **11**(8): p. A132.
315. Reddy, M.A., et al., *Lithium intercalation into nanocrystalline brookite TiO2.* Electrochemical and solid-state letters, 2006. **10**(2): p. A29.
316. Lee, D.H., et al., *Preparation of Brookite-Type TiO2/Carbon Nanocomposite Electrodes for Application to Li Ion Batteries*. 2008, Wiley Online Library.
317. Aida, I.S. and S. Sreekantan, *Effect of pH on TiO2 nanoparticles via sol-gel method.* Advanced Materials Research, 2011. **173**: p. 184-189.
318. Chen, Z., et al., *Effects of water amount and pH on the crystal behavior of a TiO2 nanocrystalline derived from a sol–gel process at a low temperature.* Journal of the American Ceramic Society, 2009. **92**(5): p. 1024-1029.
319. Molea, A., et al., *Influence of pH on the formulation of TiO2 nano-crystalline powders with high photocatalytic activity.* Powder technology, 2014. **253**: p. 22-28.
320. Bakri, A., et al. *Effect of annealing temperature of titanium dioxide thin films on structural and electrical properties*. in *AIP conference proceedings*. 2017. AIP Publishing.
321. Alsawat, M., et al., *Influence of dimensions, inter-distance and crystallinity of titania nanotubes (TNTs) on their photocatalytic activity.* Catalysis Science & Technology, 2014. **4**(7): p. 2091-2098.
322. Daghrir, R., P. Drogui, and D. Robert, *Modified TiO2 for environmental photocatalytic applications: a review.* Industrial & Engineering Chemistry Research, 2013. **52**(10): p. 3581-3599.
323. Zhou, W., et al., *One-dimensional single-crystalline Ti–O based nanostructures: properties, synthesis, modifications and applications.* Journal of Materials Chemistry, 2010. **20**(29): p. 5993-6008.
324. Tian, J., et al., *Recent progress in design, synthesis, and applications of one-dimensional TiO 2 nanostructured surface heterostructures: a review.* Chemical Society Reviews, 2014. **43**(20): p. 6920-6937.
325. Sakamoto, M. and T. Majima, *Photochemistry for the synthesis of noble metal nanoparticles.* Bulletin of the Chemical Society of Japan, 2010. **83**(10): p. 1133-1154.
326. Lu, Q., et al., *Photocatalytic synthesis and photovoltaic application of Ag-TiO2 nanorod composites.* Nano letters, 2013. **13**(11): p. 5698-5702.
327. Wang, G., et al., *Detection of T4 polynucleotide kinase activity with immobilization of TiO2 nanotubes and amplification of Au nanoparticles.* Biosensors and Bioelectronics, 2013. **43**: p. 125-130.
328. Pu, Y.-C., et al., *Au nanostructure-decorated TiO2 nanowires exhibiting photoactivity across entire UV-visible region for photoelectrochemical water splitting.* Nano letters, 2013. **13**(8): p. 3817-3823.

329. Wei, J., et al., *A review of nanostructured TiO2 application in Li-ion batteries.* Advanced Materials Research, 2013. **750**: p. 301-306.
330. Bhatnagar, A., et al., *Nanotechnology for Batteries*, in *Nanotechnology for Electronic Applications*. 2022, Springer. p. 29-48.
331. Tian, Q., et al., *Facile fabrication of one-dimensional mesoporous titanium dioxide composed of nanocrystals for lithium storage.* Electrochimica Acta, 2014. **138**: p. 155-162.
332. Tang, Y., et al., *TiO 2 nanotubes grown on graphene sheets as advanced anode materials for high rate lithium ion batteries.* RSC advances, 2014. **4**(68): p. 36372-36376.
333. Tammawat, P. and N. Meethong, *Synthesis and characterization of stable and binder-free electrodes of TiO2 nanofibers for li-ion batteries.* Journal of Nanomaterials, 2013. **2013**: p. 1-1.
334. Xia, H.-R., et al., *Floating Growth of Large-Scale Freestanding TiO2 Nanorod Films at the Gas–Liquid Interface for Additive-Free Li-Ion Battery Applications.* ACS Applied Materials & Interfaces, 2014. **6**(20): p. 17376-17383.
335. Chen, J.S. and X.W. Lou, *Anatase TiO2 nanosheet: an ideal host structure for fast and efficient lithium insertion/extraction.* Electrochemistry communications, 2009. **11**(12): p. 2332-2335.
336. Ding, S., et al., *TiO 2 hollow spheres with large amount of exposed (001) facets for fast reversible lithium storage.* Journal of Materials Chemistry, 2011. **21**(6): p. 1677-1680.
337. Wu, F., et al., *Simple preparation of petal-like TiO2 nanosheets as anode materials for lithium-ion batteries.* Ceramics International, 2014. **40**(10): p. 16805-16810.
338. Liu, J., et al., *Sandwich-like, stacked ultrathin titanate nanosheets for ultrafast lithium storage.* Advanced Materials, 2011. **23**(8): p. 998-1002.
339. Cai, Y., et al., *Porous TiO2 urchins for high performance Li-ion battery electrode: facile synthesis, characterization and structural evolution.* Electrochimica Acta, 2016. **210**: p. 206-214.
340. Shin, J.Y., D. Samuelis, and J. Maier, *Sustained lithium-storage performance of hierarchical, nanoporous anatase TiO2 at high rates: Emphasis on interfacial storage phenomena.* Advanced Functional Materials, 2011. **21**(18): p. 3464-3472.
341. Lui, G., et al., *Flexible, three-dimensional ordered macroporous TiO2 electrode with enhanced electrode–electrolyte interaction in high-power Li-ion batteries.* Nano Energy, 2016. **24**: p. 72-77.
342. Wang, X., et al., *Template-free synthesis of homogeneous yolk–shell TiO2 hierarchical microspheres for high performance lithium ion batteries.* Journal of Power Sources, 2014. **262**: p. 72-78.
343. Chang, Y.-C., et al., *Bio-ingredient assisted formation of porous TiO 2 for Li-ion battery electrodes.* RSC Advances, 2015. **5**(44): p. 34949-34955.
344. Hasegawa, G., et al., *Synthesis and electrochemical performance of hierarchically porous N-doped TiO 2 for Li-ion batteries.* New Journal of Chemistry, 2014. **38**(4): p. 1380-1384.
345. Di Lupo, F., et al., *Mesoporous TiO2 nanocrystals produced by a fast hydrolytic process as high-rate long-lasting Li-ion battery anodes.* Acta materialia, 2014. **69**: p. 60-67.
346. Madian, M., A. Eychmüller, and L. Giebeler, *Current advances in TiO2-based nanostructure electrodes for high performance lithium ion batteries.* Batteries, 2018. **4**(1): p. 7.
347. Ruan, C., et al., *Fabrication of highly ordered TiO2 nanotube arrays using an organic electrolyte.* The Journal of Physical Chemistry B, 2005. **109**(33): p. 15754-15759.

348. Mor, G., et al., *Fabrication of tapered, conical-shaped titania nanotubes.* Journal of Materials Research, 2003. **18**: p. 2588-2593.
349. Gong, D., et al., *Titanium oxide nanotube arrays prepared by anodic oxidation.* Journal of Materials Research, 2001. **16**: p. 3331-3334.
350. Zwilling, V., M. Aucouturier, and E. Darque-Ceretti, *Anodic oxidation of titanium and TA6V alloy in chromic media. An electrochemical approach.* Electrochimica Acta, 1999. **45**(6): p. 921-929.
351. Kelly, J., *The influence of fluoride ions on the passive dissolution of titanium.* Electrochimica Acta, 1979. **24**(12): p. 1273-1282.
352. Liu, G., N. Hoivik, and K. Wang, *Small diameter TiO2 nanotubes with enhanced photoresponsivity.* Electrochemistry Communications, 2013. **28**: p. 107-110.
353. Macak, J.M., et al., *Smooth anodic TiO2 nanotubes.* Angewandte Chemie International Edition, 2005. **44**(45): p. 7463-7465.
354. Balaur, E., et al., *Wetting behaviour of layers of TiO 2 nanotubes with different diameters.* Journal of Materials Chemistry, 2005. **15**(42): p. 4488-4491.
355. Liu, Y., et al., *Preparation of short, robust and highly ordered TiO2 nanotube arrays and their applications as electrode.* Applied Catalysis B: Environmental, 2009. **92**(3-4): p. 326-332.
356. Varghese, O.K., et al., *Hydrogen sensing using titania nanotubes.* Sensors and Actuators B: Chemical, 2003. **93**(1-3): p. 338-344.
357. Richter, C., et al., *Titania nanotubes prepared by anodization in fluorine-free acids.* Journal of materials research, 2007. **22**(6): p. 1624-1631.
358. Hahn, R., J. Macak, and P. Schmuki, *Rapid anodic growth of TiO2 and WO3 nanotubes in fluoride free electrolytes.* Electrochemistry communications, 2007. **9**(5): p. 947-952.
359. Nguyen, Q.A., Y. Bhargava, and T. Devine, *Titania nanotube formation in chloride and bromide containing electrolytes.* Electrochemistry communications, 2008. **10**(3): p. 471-475.
360. Raja, K., T. Gandhi, and M. Misra, *Effect of water content of ethylene glycol as electrolyte for synthesis of ordered titania nanotubes.* Electrochemistry communications, 2007. **9**(5): p. 1069-1076.
361. Yoriya, S., W. Kittimeteeworakul, and N. Punprasert, *Effect of anodization parameters on morphologies of TiO2 nanotube arrays and their surface properties.* Journal of Chemistry and Chemical Engineering, 2012. **6**(8): p. 686.
362. Tsuchiya, H., et al., *Characterization of electronic properties of TiO2 nanotube films.* Corrosion science, 2007. **49**(1): p. 203-210.
363. Joo, S., I. Muto, and N. Hara, *In situ ellipsometric analysis of growth processes of anodic TiO2 nanotube films.* Journal of the electrochemical society, 2008. **155**(4): p. C154.
364. Indira, K., et al., *A review on TiO 2 nanotubes: influence of anodization parameters, formation mechanism, properties, corrosion behavior, and biomedical applications.* Journal of bio-and tribo-corrosion, 2015. **1**: p. 1-22.
365. Indira, K., et al., *Effect of anodization temperature on the surface morphology of anodized titanium.* Thin Films and Nanomaterials. Noida: Macmillan India, 2011: p. 63-66.
366. Chen, J., J. Lin, and X. Chen, *Self-assembled TiO2 nanotube arrays with U-shaped profile by controlling anodization temperature.* Journal of Nanomaterials, 2010. **2010**: p. 1-4.
367. Tsuchiya, H., et al., *Self-organized TiO2 nanotubes prepared in ammonium fluoride containing acetic acid electrolytes.* Electrochemistry communications, 2005. **7**(6): p. 576-580.

368. Roman, I., et al., *Titanium dioxide nanotube films: Preparation, characterization and electrochemical biosensitivity towards alkaline phosphatase.* Materials Science and Engineering: C, 2014. **37**: p. 374-382.
369. Ivanov, S., et al., *Electrochemical behavior of anodically obtained titania nanotubes in organic carbonate and ionic liquid based Li ion containing electrolytes.* Electrochimica Acta, 2013. **104**: p. 228-235.
370. Li, H., et al., *High cyclability of ionic liquid-produced TiO2 nanotube arrays as an anode material for lithium-ion batteries.* Journal of Power Sources, 2012. **218**: p. 88-92.
371. Kirchgeorg, R., et al., *Key factors for an improved lithium ion storage capacity of anodic TiO2 nanotubes.* Electrochimica Acta, 2016. **198**: p. 56-65.
372. Ryu, W.-H., et al., *Electrochemical performance of a smooth and highly ordered TiO2 nanotube electrode for Li-ion batteries.* Electrochimica Acta, 2012. **61**: p. 19-24.
373. Guan, D., C. Cai, and Y. Wang, *Amorphous and crystalline TiO2 nanotube arrays for enhanced Li-ion intercalation properties.* Journal of nanoscience and nanotechnology, 2011. **11**(4): p. 3641-3650.
374. Wei, Z., et al., *TiO 2 nanotube array film prepared by anodization as anode material for lithium ion batteries.* Journal of Solid State Electrochemistry, 2010. **14**: p. 1045-1050.
375. Wei, W., et al., *High energy and power density TiO 2 nanotube electrodes for 3D Li-ion microbatteries.* Journal of Materials Chemistry A, 2013. **1**(28): p. 8160-8169.
376. Tighineanu, A., et al., *Conductivity of TiO2 nanotubes: Influence of annealing time and temperature.* Chemical Physics Letters, 2010. **494**(4-6): p. 260-263.
377. Lu, Z., et al., *Hydrogenated TiO2 nanotube arrays as high-rate anodes for lithium-ion microbatteries.* ChemPlusChem, 2012. **77**(11): p. 991-1000.
378. Mole, F., et al., *Highly conductive nanostructured C-TiO2 electrodes with enhanced electrochemical stability and double layer charge storage capacitance.* Langmuir, 2012. **28**(28): p. 10610-10619.
379. Wang, Y., et al., *Electrochemical properties of freestanding TiO 2 nanotube membranes annealed in Ar for lithium anode material.* Journal of Solid State Electrochemistry, 2012. **16**: p. 723-729.

Appendix

Turnitin Plagiarism Report:

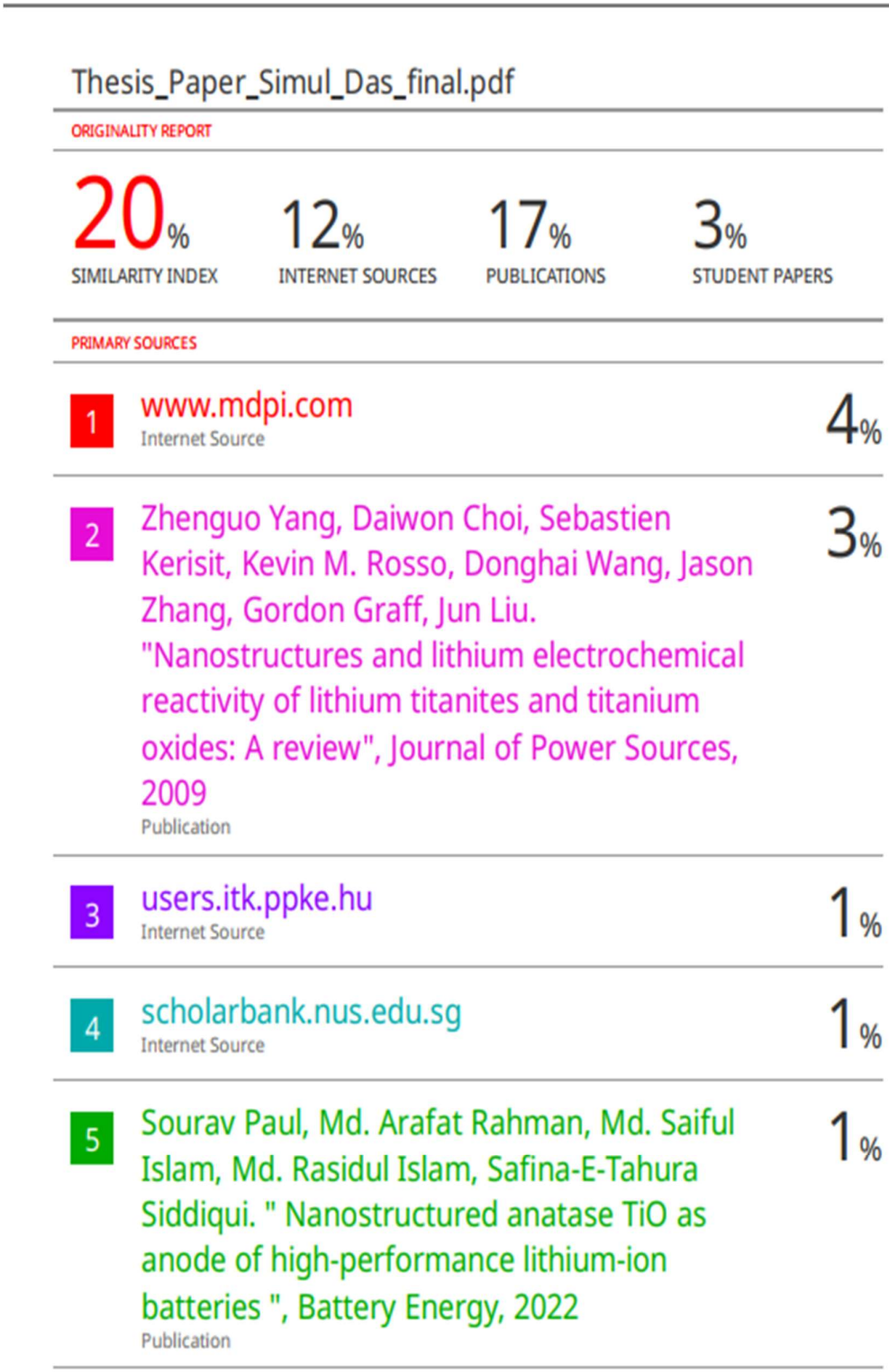

Thesis_Paper_Simul_Das_final.pdf

ORIGINALITY REPORT

20%	12%	17%	3%
SIMILARITY INDEX	INTERNET SOURCES	PUBLICATIONS	STUDENT PAPERS

PRIMARY SOURCES

1	www.mdpi.com Internet Source	4%
2	Zhenguo Yang, Daiwon Choi, Sebastien Kerisit, Kevin M. Rosso, Donghai Wang, Jason Zhang, Gordon Graff, Jun Liu. "Nanostructures and lithium electrochemical reactivity of lithium titanites and titanium oxides: A review", Journal of Power Sources, 2009 Publication	3%
3	users.itk.ppke.hu Internet Source	1%
4	scholarbank.nus.edu.sg Internet Source	1%
5	Sourav Paul, Md. Arafat Rahman, Md. Saiful Islam, Md. Rasidul Islam, Safina-E-Tahura Siddiqui. " Nanostructured anatase TiO as anode of high-performance lithium-ion batteries ", Battery Energy, 2022 Publication	1%